IntechOpen

# Charged Particles

*Edited by Malek Maaza and Mahmoud Izerrouken*

# Charged Particles

*Edited by Malek Maaza*
*and Mahmoud Izerrouken*

Published in London, United Kingdom







IntechOpen






*Supporting open minds since 2005*

Charged Particles
http://dx.doi.org/10.5772/intechopen.73999
Edited by Malek Maaza and Mahmoud Izerrouken

Contributors
Ian Lazarus, Takemi Otsuki, Suni Lee, Kei Yoshitome, Nagisa Sada, Megumi Maeda, Hidenori Matsuzaki, Naoko Kumagai-Takei, Yasumitsu Nishimura, Thomas Taylor, Jaydip Singh, Srishti Nagu, Jyotsna Singh, Takaaki Nomura, Ishaq Ahmad



First published in London, United Kingdom, 2019 by IntechOpen
eBook (PDF) Published by IntechOpen, 2019
IntechOpen is the global imprint of INTECHOPEN LIMITED, registered in England and Wales, registration number: 11086078, The Shard, 25th floor, 32 London Bridge Street
London, SE19SG – United Kingdom
Printed in Croatia

British Library Cataloguing-in-Publication Data
A catalogue record for this book is available from the British Library

Additional hard and PDF copies can be obtained from orders@intechopen.com

Charged Particles
Edited by Malek Maaza and Mahmoud Izerrouken
p. cm.
Print ISBN 978-1-78985-395-7
Online ISBN 978-1-78985-396-4
eBook (PDF) ISBN 978-1-83962-035-5

# Meet the editors

Prof. M. Maaza holds a PhD in Quantum Neutron Optics from the University of Pierre-Marie Curie and the Commissariat a lEnergie Atomique, respectively. He is currently a permanent joint staff member of the National Research Foundation of South Africa, in charge of the Africa-International relations desk at iThemba LABS and the University of South Africa. Prof. Maaza is the chair of reputable international organizations and commissions. His expertise is in the multidisciplinary field of nanosciences, photonics, and solar energy. Within the STI and RDI landscapes, with a Hirsch index of 33, Prof. Maaza has published more than 300 ISI international publications and supervised several postgraduates from all over Africa and the south.

Mahmoud Izerrouken joined the Nuclear Research Centre of Draria in 1996 and currently holds the position of Head of the Nuclear Techniques Department, Nuclear Research Center of Draria, Algiers, Algeria. He has coauthored over 30 publications in SCI journals and supervised several Master's and PhD students. His research interests are focused on ion- and neutron-induced damage in materials. He obtained his PhD at Ferhat Abbas University, Faculty of Sciences, Setif, Algeria.

# Contents

# Preface

Particle physicists believe that the creation of the universe and matter was started as a result of a very big explosion known as the big bang. At this time, matter and antimatter were created in equal amounts. Just after the big bang at $t \sim 10^{-35}$ s came the era of grand-unification transition, i.e. inflation, baryogenesis, monopoles, cosmic strings, etc. Sometime later, electro-weak phase transition occurred, i.e. electromagnetic and weak nuclear forces became differentiated. At $t \sim 10^{-6}$ protons and neutrons formed. Then nucleo-synthesis occurred, i.e. light elements were created, e.g. D, He, Li, etc. With the creation of light elements the amount of positive and negative charges was balanced inside an atom. There are electrons carrying a negative charge and protons carrying a positive charge inside atoms. This book briefly looks at high-energy charged particle physics and gives a flavor of the application of charged particles.

The first part of the book covers the cutting-edge and important research topic of flavor physics to search for new areas of physics via charged particles that appear in different extensions of the standard model. The latest research on the analysis of ultra-high energy muons using the pair-meter technique is also presented in a Geant4 simulation study for iron plates. In this study, the feasibility of detecting high-energy muons (1–1000 TeV) in the underground iron calorimeter detector is demonstrated. The idea of the Eloisatron to Pevatron is also included in this book.

The second part of this book covers the important research field of electrostatic waves in magnetized electron/positron plasmas where the behavior of the arbitrary amplitude of electrostatic waves propagation in an electron/positron plasma is discussed in detail. Well-known fluid and kinetic approaches have been used to describe linear waves, whereas nonlinear analysis of electrostatic waves is done via fluid modeling.

The final part of the book addresses the most important applications of charged bodies. Apart from high-energy particle physics, the application of charged bodies is also included in this book, such as immune effects of negatively charged particles dominating indoor air conditions and many others.

The authors gratefully acknowledge all those who contributed to this book : Prof. Dr. Ishaq Ahmad, Prof. Dr. Jaydip Singh, Prof. Dr. Srishti Nagu, Prof. Dr. Jyotsna Singh, Prof. Dr. Thomas Taylor, Prof. Dr. Takaaki Nomura, Prof. Dr. Ian Joseph Lazarus, Prof. Dr. Suni Lee, Prof. Dr. Yasumitsu Nishimura, Prof. Dr. Naoko Kumagai-Takei,

Prof. Dr. Hidenori Matsuzaki, Prof. Dr. Megumi Maeda, Prof. Dr. Nagisa Sada, Prof. Dr. Kei Yoshitome, Prof. Dr. Takemi Otsuki, and Ms. Marijana Francetic, Author Service Manager.

**Prof. Dr. Maaza Malek**
iThemba LABS-National Research Foundation, Somerset West, South Africa,
UNESCO-UNISA Africa Chair in Nanosciences/Nanotechnology,
University of South Africa

**Prof. Dr. Mahmoud Izerrouken**
Nuclear Research Center Draria, Algiers, Algeria

Section 1

# Introductory Chapter

Chapter 1

# Introductory Chapter: Charged Particles

*Mahmoud Izerrouken and Ishaq Ahmad*

## 1. Overview

Bringing history back in August 1912, Austrian physicist Victor Hess discovered cosmic rays coming from outer space. These cosmic rays consist of high-energy particles, entering from outer space, such as mainly protons, helium, and heavier nuclei up to uranium. When these cosmic rays come to earth to interact with upper atmosphere, they collide with the nuclei of atoms, creating more high-energy particles such as pions. The charged pions can quickly decay into two particles, a muon and a muon neutrino or antineutrino. Several high-energy particles were also discovered, which is long list. Studies of cosmic rays opened the door to a world class of particles.

It is concluded that charged particle is a particle that carries an electric charge. In atomic levels, the atom consists of nucleus around which the electrons turn. The nucleus is formed by proton and neutron and thus carries a positive charge (the proton charge is $1.602 \times 10^{-19}$ Coulombs). The electron carries a negative charge ($-1.602 \times 10^{-19}$ Coulombs). An atom is called neutral if the number of protons equals the number of electrons. Thus, an atom can be positive, negative, or neutral. The charged particle is negative when it gains electron from another atom. It is positively charged if it loses electron from it. Applications of charged particles are subjected to control their motion and energy through electric field and magnetic field. Therefore, motion of charged particle in electric and magnetic fields is discussed in order to understand the beam of charged particles and their applications.

## 2. Charged particles motion in an electromagnetic field ($\vec{E}$ , $\vec{B}$)

The motion of charged particle of mass $m$ and charge $q$ with a velocity $\vec{v}$ in uniform magnetic field $\vec{B} \neq \vec{0}$ and uniform electric field $\vec{E}$ is subjected to an electromagnetic force called the Lorentz force given by:

$$\vec{F} = q\vec{E} + q\vec{v} \times \vec{B} \tag{1}$$

From Newton second law, the particle's equation of motion is written as:

$$m\frac{d\vec{v}}{dt} = q\left(\vec{E} + \vec{v} \times \vec{B}\right) \tag{2}$$

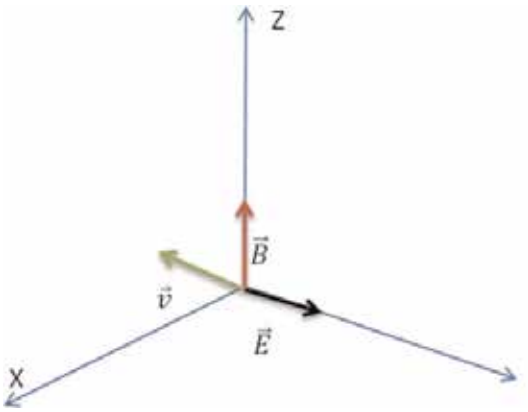


Let us assume that the magnetic field is applied in the direction Oz and electric field $\vec{E}$ is applied in the direction Oy.

1. In the case of motion of charged particle through a stationary electric field $\vec{E} = \vec{E_0}$ and $\vec{B} = \vec{0}$, the equation of motion is:

$$m\frac{d\vec{v}}{dt} = q\vec{E} \;\Leftrightarrow\; \vec{v} = \frac{q\vec{E}}{m}t + \vec{v_0} \tag{3}$$

The projection of (3) on the axes gives

$$\begin{aligned} m\frac{dv_x}{dt} &= 0 \\ m\frac{dv_y}{dt} &= qE \\ m\frac{dv_z}{dt} &= 0 \end{aligned} \tag{4}$$

The integration of (4) with the initial conditions $x(0) = 0, y(0) = 0$, and $z(0) = 0; vx(0) = v_{x0}$, $vy(0) = v_{yo}$, and $vz(0) = v_{z0}$ gives:

$$\begin{aligned} x &= v_{x0}t \\ y &= \frac{qE}{2m}t^2 + v_{y0}t \\ z &= v_{0z}t \end{aligned} \tag{5}$$

If $\vec{E}$ and $\vec{v}$ are collinear, the motion is rectilinear and uniformly accelerated.

2. In the case of motion of charged particle in uniform magnetic field $\vec{B} \neq \vec{0}$, the projection of (2) on the axes gives:

$$\begin{aligned} m\frac{dV_x}{dt} &= qBV_y \Leftrightarrow \frac{dV_x}{dt} = \frac{qB}{m}\,V_y \\ m\frac{dV_y}{dt} &= -qBV_x + qE \Leftrightarrow \frac{dV_y}{dt} = -\frac{qB}{m}V_x + \frac{q}{m}E \\ m\frac{dV_z}{dt} &= 0 \end{aligned} \tag{6}$$

We note $\Omega = \frac{qB}{m}$ the so-called cyclotron frequency.
The solution of (6) is:

$$\begin{aligned} x &= \frac{E}{B}t + \frac{1}{\Omega}\left(v_{x0} - \frac{t}{B}\right)\sin(\Omega t) + \frac{v_{y0}}{\Omega}(1 - \cos(\Omega t)) \\ y &= \frac{1}{\Omega}\left(v_{x0} - \frac{t}{B}\right).(\cos(\Omega t) - 1) + \frac{v_{y0}}{\Omega}\sin(\Omega t) \\ z &= v_{z0}\, t \end{aligned} \tag{7}$$

According to the above equations, we can see that the charged particle can have different trajectories. Depending on the initial conditions, the trajectory could be straight, parabolas, circles, cycloids, spirals, etc. Lorentz force is then a base of charged particle acceleration and beam guidance.

## 3. Charged particle accelerators

After understanding the concept of controlling and generating the charged particles, different machines were developed to deflect or accelerate the charged particles through electromagnetic fields. The machines that generate and push charged particles to very high speed and energies and contain them in well-defined beams are called charged particle accelerators. A large variety of accelerators were developed since that fabricated by Cockcroft and Walton in 1932. Using such accelerator, the authors achieved the first nuclear reaction using artificially accelerated particle:

$$p + Li \rightarrow 2He$$

Since then, more and more successful accelerators appeared according to the progress in particle acceleration techniques. Depending on the accelerated particle trajectory, we can distinguish linear accelerators and circular accelerators. The accelerator during the last century can be found chronologically in [1]. Currently available electrostatic accelerators and cyclotrons over the world can produce and accelerate intense and stable charged particle beams with energy varying between few keV and few TeV. Charged particle accelerators are classified as per their applications:

## 4. Classification of charged particles

Charged particle accelerators are classified mainly into electrostatic and electromagnetic.

### 4.1 Electrostatic charged particle accelerators

In electrostatic accelerators, the static high voltage was generated and then applied across the ion source. The charged particles are accelerated through static electric field generated from static high voltage due to the electrostatic force. These types of accelerators are suitable to accelerate light and heavy ions from keV to few MeV energies. These ion beams, charged particle beams of various energies, are standard research tools in many areas of sciences and engineering having many applications in nuclear physics, atomic physics, medicine, materials science,

agriculture, industry, and so on [2–6]. It is an advanced and versatile tool frequently applied across a broad range of discipline and fields.

### 4.2 Electromagnetic charged particle accelerators

Electrostatic charged particle accelerators have limitations on its beam energy due to high electrical voltage discharge. To avoid electrical discharge and increase charged particle energies, techniques involved electromagnetic fields instead of electrostatic fields. Electromagnetic acceleration is possible from two mechanisms either nonresonant magnetic induction or resonant circuits or cavities excited by oscillating radio frequency. High-energy charged particle colliders are installed around the world for forefront of scientific discoveries. These colliders are based on electrostatic charged particle accelerators. Through high-energy colliders, standard models are verified experimentally. Moreover, the cutting-edge and important research topic of flavor (particle physics) to search for new physics via charged particles that appears in the different extension of standard model is presented in this book. The latest research on analysis of ultrahigh-energy muon using pair-meter technique is also presented in Geant4 simulation study for iron plates. In this study, the feasibility for detection of high-energy muons at the underground iron calorimeter detector is demonstrated. The basic aim of this study is to detect high-energy muons (1–1000 TeV). The idea of the Eloisatron to Pevatron is also included in this book.

## 5. Charged particles applications

Charged particles interact with electrons and atom nuclei via Coulomb force, also called electrostatic force. When two charges are placed near to each other, they will be repulsed if they have the same charge or attract each other if they are of opposite charges. Each particle exerts a force on each other given by Coulomb's law expressed as:

$$F = k\frac{Q1Q2}{r^2}$$

where Q1, Q2, and r are the charge of the two particles (1 and 2) in Coulomb and the distance between the charges and k is the proportionality constant:

$$k = \frac{1}{4\pi\varepsilon}$$

Thus, when accelerated charged particle moves in materials, it interacts with orbital electron and nuclei via Coulomb interaction depending on its energy. At low energy ($<0.01$ MeV/u), the interaction is with nuclei, known as elastic interaction. This interaction leads to atomic displacement. At high energy ($>0.01$ MeV/u), the interaction is mainly with orbital electron known as inelastic interaction and leads to ionization and excitation. At very high energy, nuclear reactions can be produced and give rise to new particles (neutron, proton alpha, gamma rays). The basic interaction process of charged particle with matter is well known, and much performed detectors are now available. So ion beam is actually used in several applications. Electrostatic waves in magnetized electron-positron plasmas are covered in this book where the behavior of arbitrary amplitude of electrostatic wave propagation in electron-positron plasma is discussed. The well-known fluid and kinetic approaches have been used to describe linear waves, whereas the nonlinear

analysis of ESW is done via fluid modeling. Apart from the high-energy particle physics, charged bodies are also included in this book such as immune effects of negative charged particles dominated by indoor air conditions and many others.

## 6. Charged particle beams for materials analysis

Several techniques of ion beam analysis (IBA) are being used for the study of the chemical composition and structure of surfaces, interface, and thin layers and are explained as below.

### 6.1 Rutherford backscattering spectroscopy

The accelerated charged particle with energy $E_0$ and mass $M_1$ scatters from the analyzed surface containing the particle $M_2$ with energy $E_1$ and scattering angle $\theta$. From the conservation laws of energy and momentum and the known Rutherford cross section, it is possible to deduce the mass $M_2$ and estimate its abundance [7, 8].

### 6.2 Nuclear reaction analysis (NRA)

The NRA technique is very useful as a tool for the detection and profiling of light elements. The fast charged particle (few MeV) initiates a nuclear reaction with target atom. The reaction products are characteristic for this reaction and can be used to identify the target atom and its concentration. For example, determination of hydrogen content in material: for this purpose, $H(^{15}N, \alpha\gamma)^{16}O$ nuclear reaction is used. This reaction produces alpha particle and excited $^{12}C$ isotope. The disintegration of the excited $^{12}C$ to ground state emits a gamma photon with a well-defined energy of $E\gamma = 4.43$ MeV, which identifies hydrogen content in material.

### 6.3 Elastic recoil detection analysis (ERDA)

ERDA technique is a unique method to measure the H and D content in thin films. When He ion (alpha particle) interacts with material containing hydrogen (H) and deuterium (D), the H and D will be scattered in the forward direction. From the detection of the forwarded H and D, one can measure the quantitative depth profiling of these elements in the material. Similar experiments can be performed using heavy ion beam to study light element profiling.

### 6.4 Particle-induced X-ray emission (PIXE)

Ion beam of energy typically 1–2 MeV induces ionization of the target atom. If the ejected electron belongs to K-shell, an X-ray characteristic of the irradiated element is emitted. Using this technique, qualitative and quantitative analysis can be used where the trace element of about 1 ppm can be achieved [9].

## Author details

Mahmoud Izerrouken[1*] and Ishaq Ahmad[2]

1 Nuclear Research Center Draria, Algiers, Algeria

2 National Centre for Physics, Islamabad, Pakistan

*Address all correspondence to: m-izerrouken@crnd.dz

## References

[1] Brissaud I, Baron E. The Race of Particle Accelerators to High Energy and Log Periodicity, Cybergeo: European Journal of Geography [Online], Debates, Theory of Relativity Scale and Log Periodicity. Online: December 11, 2007. [Accessed Dec 14, 2018]. http://journals.openedition.org/cybergeo/14173

[2] Awais A, Hussain J, Usman M, Akram W, Shahzad K, Ali T, et al. The charge state distribution of B, C, Si, Ni, Cu and Au ions on 5 MV Pelletron accelerator. Nuclear Science and Techniques. 2017;**28**(5):64

[3] Ahmad I, Madhuku M, Sadaf A, Khan S, Hussain J, Ali A, et al. Tailoring the structural and optical characteristics of InGaN/GaN multilayer thin films by 12 MeV Si ion irradiation. Materials Science in Semiconductor Processing. 2017;**64**:95-100

[4] Ni Z, Ishaq A, Yan L, Gong J, Zhu D. Enhanced electron field emission of carbon nanotubes by Si ion beam irradiation. Journal of Physics D: Applied Physics. 2009;**42**:075408

[5] Ahmad I, Long Y, Suixia H, Dezhang Z, Xingtai Z. Optical absorption of ion irradiated multi-walled carbon nanotube sheets in the visible to terahertz ranges. Nuclear Science and Techniques. 2009;**20**:197-201

[6] Ishaq A, Yan L, Gong J, Zhu D. Graphite-to-amorphous structural transformation of multiwalled carbon nanotubes under proton beam irradiation. Materials Letters. 2009;**63**: 1505-1507

[7] Husnain G, Shu-De Y, Ahmad I, Lin L. Role of substrate temperature on structure and magnetization of Cr-implanted GaN thin film. Applied Physics A: Materials Science & Processing. 2014;**117**:2275-2279

[8] Husnain G, Ahmad I, Rafique HM, Akrajas AU, Dee CF. Depth-dependent tetragonal distortion study of AlGaN epilayer thin film using RBS and channeling technique. Modern Physics Letters B. 2012;**26**(14):1250086

[9] Akram W, Madhuku M, Shehzad K, Awais A, Ahmad I, Ahmad I, et al. Roadside dust contamination with toxic metals along Islamabad industrial area. Nuclear Science and Techniques. 2014; **25**(3):030201

Section 2

# High Energy Particle Physics

Chapter 2

# Analysis of Ultra-High Energy Muons at INO-ICAL Using Pair Meter Technique

*Jaydip Singh, Srishti Nagu and Jyotsna Singh*

## Abstract

The proposed magnetized Iron CALorimeter (ICAL) detector at India-based Neutrino Observatory (INO) is a large-sized underground detector. ICAL is designed to reconstruct muon momentum using magnetic spectrometers as detectors. Muon energy measurements using magnets fail for high energy muons (TeV range), since the angular deflection of the muon in the magnetic field is negligible and the muon tracks become nearly straight. A new technique for measuring the energy of muons in the TeV range, used by the CCFR neutrino detector is known as the pair meter technique. This technique estimates muon energy by measuring the energy deposited by the muon in several layers of an iron calorimeter through $e^+$ and $e^-$ pair production. In this work we have performed Geant4-based preliminary analysis for iron plates and have demonstrated the feasibility to detect very high energy muons (1–1000 TeV) at the underground ICAL detector operating as a pair meter. This wide range of energy spectrum will not only be helpful for studying the cosmic rays in the Knee region which is around 5 PeV in the cosmic ray spectra but also useful for understanding the atmospheric neutrino flux for the running and upcoming ultra-high energy atmospheric neutrino experiments.

**Keywords:** pair meter techniques, cosmic rays, iron calorimeter

## 1. Introduction

ICAL at INO is a 52 ktons detector [1] proposed to be built at Theni district of Tamil Nadu in Southern India. It is designed to study the flavor oscillations of atmospheric neutrinos. The main goal of the ICAL detector is to precisely measure the neutrino oscillation parameters and to determine the neutrino mass hierarchy [1]. At a depth of around 1.2 km underground, the INO-ICAL detector will be the world's biggest magnetized detector to measure cosmic ray muon flux with the capability to distinguish $\mu+$ from $\mu-$. The existing direct and indirect methods of muon spectrometry at accelerator-based and in cosmic rays (magnetic spectrometers and transition radiation detectors) experiments involve certain technical problems and limitations in the energy region $\geq 10^{13}$ eV. These disadvantages vanquish in this alternate method where the muon energy is estimated by measuring the energy of secondary cascades formed by muons losing their energy in thick layers of matter, mainly due to the process of direct pair production of $e^+$ and $e^-$. By using this technique, muon energy can be estimated from INO-ICAL detector operating

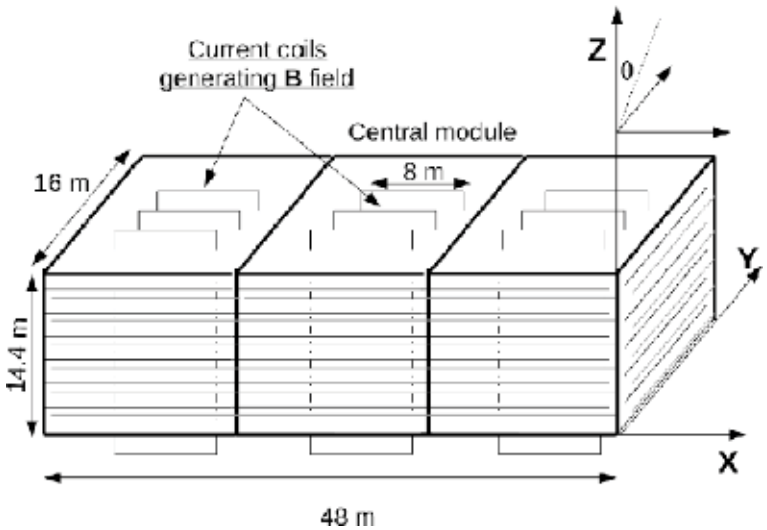


**Figure 1.**
*Schematic view of three modules for the proposed INO-ICAL detector.*

as a pair meter. The primary cosmic rays which are approximately in 50 TeV–50 PeV energy range correspond to this energy range [5].

This work presents a simulation based on the latest version of Geant4 [3] INO-ICAL code, developed by the INO collaboration for momentum reconstruction of muons in GeV energy range using INO-ICAL magnet. We have developed a separate Geant4 code for counting the muon bursts in iron plates for ultra-high energy muon analysis using the pair meter technique. The proposed detector will have a modular structure of total lateral size 48 m × 16 m, subdivided into three modules of size 16 m × 16 m. The height of the detector will be 14.5 m. It will consist of a stack of 151 horizontal layers of ~5.6 cm thick magnetized iron plates interleaved with 4 cm gaps to house the active detector layers. Detector geometry of ICAL magnet is presented in **Figure 1** and details of the components and dimensions are discussed in Ref. [1].

## 2. Momentum reconstruction analysis with ICAL magnet

In this section we have discussed the simulation for momentum reconstruction of muons in magnetic field. Details of the detector simulation for muons with energy of few 10's of GeV with older version of INO-ICAL code are already published in Ref. [4]. For simulating the response of high energy (100's of GeV) muons in the ICAL detector, 10,000 muons were propagated uniformly from a vertex randomly located inside 8 m × 8 m × 10 m volume. This is the central region of the central module where the magnetic field is uniform of 1.5 T. In our analysis we have considered only those events whose z coordinate of the input vertex lie within $z_{in} \leq 400$ cm which comprises the vertex to the central region. The input momentum and zenith angle are kept fixed in each case while the azimuthal angle is uniformly averaged over the entire range $-\pi \leq \phi \leq \pi$. In each case, we have studied the number of reconstructed tracks, the position resolution, including up/down discrimination and the zenith angle resolution. In this chapter, we have followed the same approach as in Ref. [4] for muon response analysis upto energy 500 GeV inside the detector [8]. Momentum reconstruction efficiency in the energy range of 1–400 GeV is shown in **Figure 2** and this energy range at the detector corresponds to the surface muon lying in the energy range 1600–2000 GeV from the top of the

surface. Muon will lose around 1600 GeV in the rock overburden [8] to reach at the detector from the top surface. Energetic muons from other directions will also hit the detector since the rock cover in other directions of detector is very huge, so we have not incorporated it in our discussion.

The momentum reconstruction efficiency ($\varepsilon_{recon}$) is defined as the ratio of the number of reconstructed events, n rec, to the total number of generated events, $N_{total}$. We have

$$\varepsilon_{recon} = \frac{n_{rec}}{N_{total}} \tag{1}$$

with error, $\delta\varepsilon_{recon} = \sqrt{(\varepsilon_{recon}(1 - \varepsilon_{recon})/N_{total})}$.

**Figure 2** shows the muon momentum reconstruction efficiency as a function of input momentum for different cos$\theta$ bins, here left and right panels demonstrate detector response for low and high energy muon momentum respectively. One can see that the momentum reconstruction efficiency depends on the incident particle momentum, the angle of propagation and the strength of the magnetic field. As the input momentum increases, the reconstruction efficiency increases for all angles because with increase in energy the particle crosses more number of layers producing more hits in the detector. But at sufficiently high energies, the reconstruction efficiency starts decreasing, since the muons travel nearly straight without being deflected in the magnetic field of the detector. Track reconstruction is done using Kalman Filter techniques [4], tracks for few typical energies are plotted in **Figure 3**, which shows the deflected and undeflected muon tracks depending on the energy of muons in a fixed magnetic field (1.5 T).

Pair meter techniques:

1. High energy muons produce secondary cascades mainly due to electron pair production process.

2. It is one of the most important processes for muon interaction at TeV energies, pair creation cross section exceeds those of other muon interaction processes in a wide range of energy transfer:

100 MeV $\leq E_0 \leq 0.1E_\mu$, $E_0$ is threshold energy.

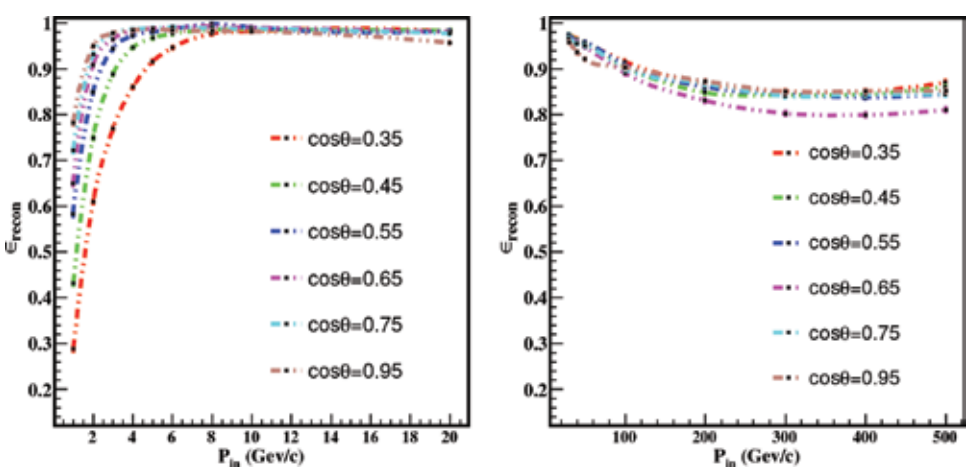


**Figure 2.**
*Reconstructed momentum efficiency as a function of the input momentum for different cos θ values at low (1–20 GeV) and high energy (20–500 GeV).*

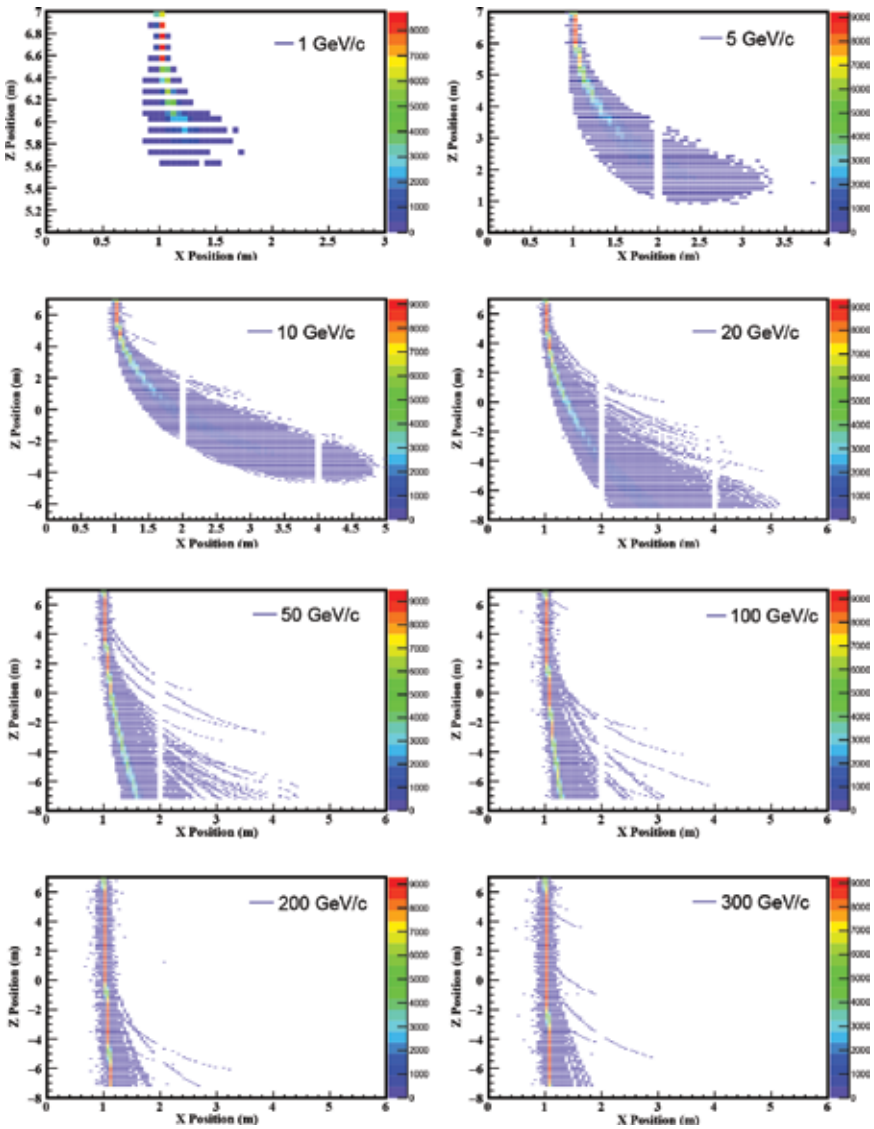


**Figure 3.**
*Fixed energy muons track stored in X-Z plane of the detector going in the downward direction.*

3. Average energy loss for pair production increases linearly with the increase in the muon energy and in the TeV region this process contributes more than 50% of the total energy loss rate.

4. Pair meter method for energy reconstruction of high energy muons has been used by the NuTeV/CCFR collaboration [6].

## 2.1 Average number of burst calculation

The $e^+$ and $e^-$ pair production cross section by a muon of energy $E_\mu$ with energy transfer above a threshold $E_0$ increases as $\ln^2 (2m_e E_\mu/m_\mu E_0)$ where $m_\mu$ and $m_e$ are the masses of the muon and the electron respectively [1]. Defining $v = E_0/E_\mu$, above $v^{-1} = 10$, this cross section dominates over other processes by which the muon loses its energy when it passes through dense matter, generating observable cascades.

- The pair production cross section depends upon $E_\mu/E_0$ which allows one to estimate the energy of muon by counting the number of interaction cascades M in the detector with energies above a threshold $E_0$.

- Differential cross section for pair production is estimated in Ref. [1] and that expression is given by:

$$v\frac{d\sigma}{dv} \simeq \frac{14\alpha}{9\pi t_0} ln\left(\frac{km_e E_\mu}{E_0 m_\mu}\right) \tag{2}$$

where $\alpha$ = 1/137, k ≃ 1.8 and $t_0$ is the radiation length(r.l.) of the material, for iron $t_0$ = 13.75 g/cm$^2$.

- The average number of interaction cascades M above a threshold $E_0$ is given by:

$$M(E_0, E_\mu) = Tt_0\,\sigma(E_0, E_\mu) \tag{3}$$

$$E_\mu = (E_0 m_\mu/km_e)\, exp\left(\sqrt{9\pi M/7\alpha T - A}\right) \tag{4}$$

where T is target thickness and σ ($E_0$,$E_\mu$) is the integrated cross section(in unit of cm$^2$/g) and A ≃ 1.4.,

$$\sigma(E_0, E_\mu) \simeq \frac{7\alpha}{9\pi t_0}\left(ln^2\left(\frac{km_e E_\mu}{E_0 m_\mu}\right) + A\right) \tag{5}$$

## 3. Counting the burst using pair meter

A muon traversing vertically from the top will cover 151 × 5.6 ≃ 845 cm in iron plates, this is equivalent to a path-length of ≃480 r.l.(g/cm$^2$). The number of cascades produced by high energy muon for a path length of 450 r.l.(g/cm$^2$) can be calculated using Eq. (3). The number of cascades produced as a function of muon energy is shown in **Figure 4**, which increase with energy in the energy range $10^3$–$10^6$ GeV (1–1000 TeV). One can interpret from **Figure 4** that the approximate number of interactions for a 1 TeV muon at threshold energy $E_0$ of 1 GeV is 4. Similarly for a 10 TeV muon, the number of interactions for $E_0$ = 10 GeV is 4 and for 1 GeV is 20. For a 100 TeV muon, the number of interactions for $E_0$ = 100 GeV is around 4, for $E_0$ = 10 GeV is close to 20 and for $E_0$ = 1 GeV is approximately 50.

### 3.1 Penetration depth of electron in the iron plates

The estimation of muon burst energy in iron plates is done by evaluating the energy of electron and positron pair, for that $e^+$ and $e^-$ must hit the active elements of the detector, that is, the RPC which is a type of spark chamber with resistive electrodes placed parallel to each other. Measurement of penetration depth of the electron in iron gives us a handle to determine the energy loss of the electrons in the iron plates. The energy loss of electron in iron is given by: $E = E_0\, e^{-x/x_0}$, where $x$ is distance traveled in the iron plate and $x_0$ is the radiation length. It is thus important to determine the range of electron in iron plates which is shown in **Figure 5**.

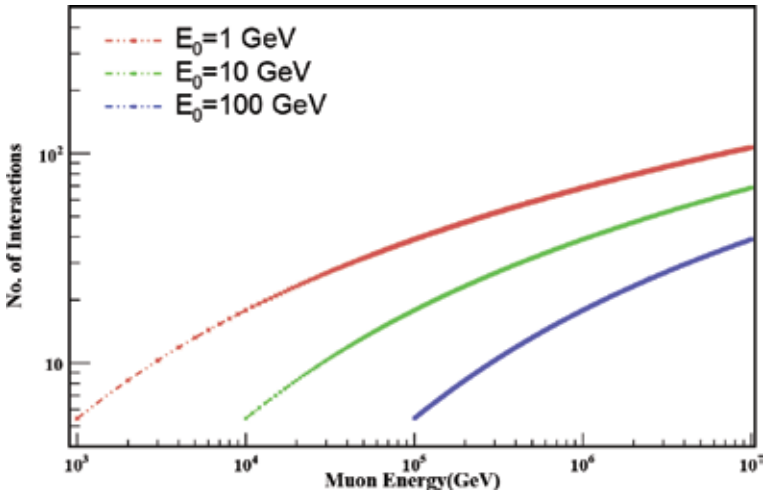


**Figure 4.**
*Average number of bursts above a threshold $E_0$ versus muon energy for $E_0$ = 1, 10 and 100 GeV, with T fixed to 450 r.l.*

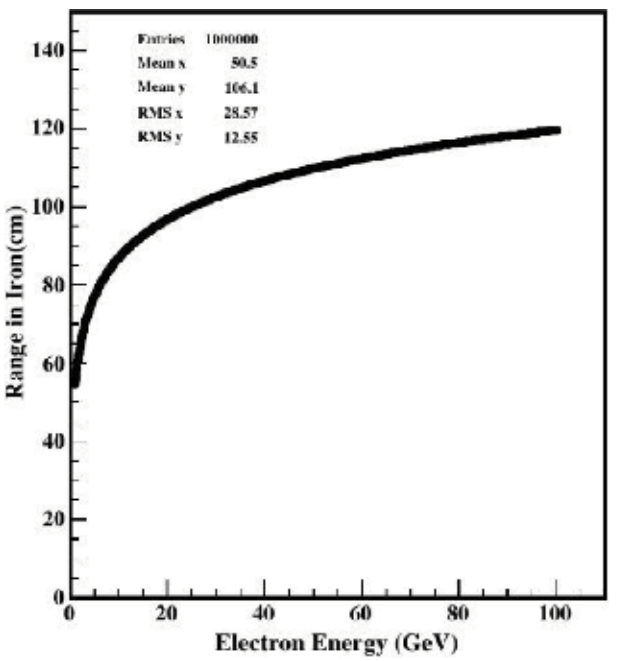


**Figure 5.**
*Energy of the electron and its corresponding penetrating range in the iron plates.*

### *3.1.1 Muon burst of a few typical energies in the iron plates*

A Geant4-based code is developed for simulating the muons burst in iron plates, here horizontal axis is the z-axis of INO-ICAL detector, in which 152 layers of iron plates of width 5.6 cm are placed vertically, interleaved with 2.5 cm gaps for placing the RPC. Muons are propagated using Geant4 particle generator class and generated bursts in the iron plates are counted, muon bursts for a 10, 100, 500 and 1000 GeV are shown in **Figure 6(a)–(d)** respectively [7].

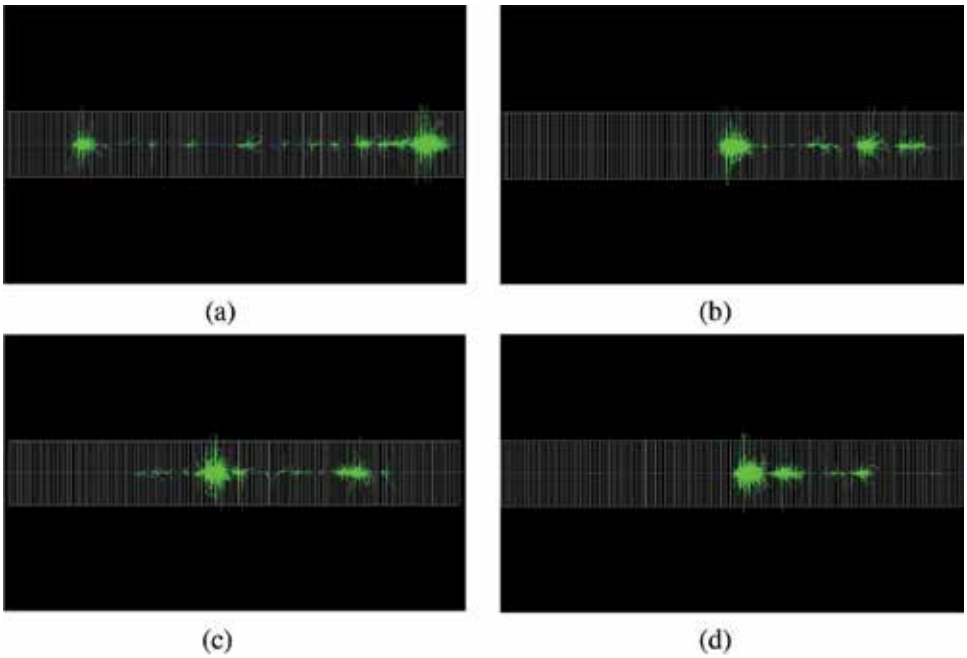


**Figure 6.**
*Cascade generation for a few typical energies. Blue line (muon) represents z-axis of the detector and green line represents the electron-positron cascade in the x-y plane.*

### 3.2 Operating ICAL using pair meter technique

Cosmic rays are composed of highly energetic particles mostly protons, alpha particles and a small fraction of heavier nuclei that reach the Earth from the outer space. Supernova bursts, quasars and other astronomical events are believed to be the sources of cosmic rays ranging over $10^{20}$ eV of energy [9]. The cosmic ray (CR) spectrum depicts a power law behavior over the entire spectral range but displaying two transition regions where the slope of the spectrum changes abruptly. The

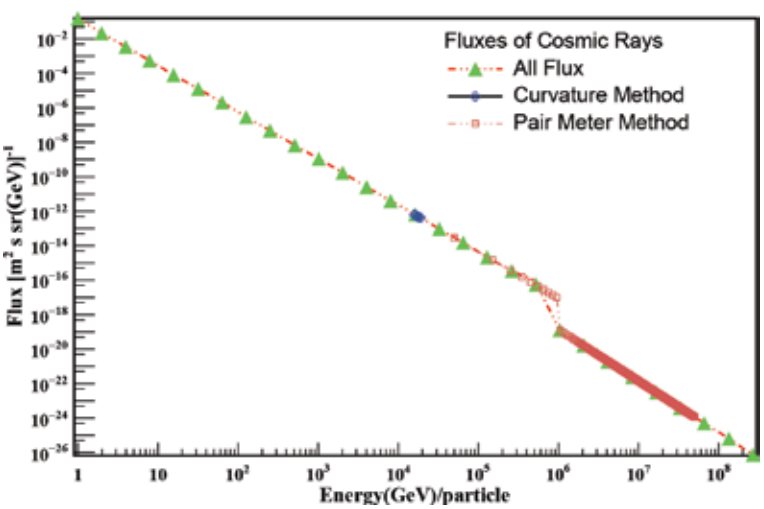


**Figure 7.**
*Primary cosmic ray flux ($\phi \simeq KE^{-\alpha}$, where $\alpha \simeq 2.7$ and for KNEE (3PeV) $\alpha$: $2.7 \rightarrow 3$) versus energy of primary particle, and limited range for ICAL to cover the spectrum using magnetic field and pair meter technique.*

region around E ~ 5 PeV is where the CR spectrum becomes steeper, is known as the 'knee' region. At higher energy around E ~ 5000 PeV, the CR spectrum flattens at the 'ankle' where the sources of such high energies are believed to be of extra-galactic origin. The reason for these two appreciable 'breaks' in the CR spectrum is still unknown. Once accelerated at supernova shocks, cosmic rays have to propagate through the interstellar medium before they can be detected. CR muons are created when cosmic rays enter the Earth's atmosphere where they eventually collide with air molecules and decay into pions. The charged pions ($\pi^+$ and $\pi^-$) decay in flight. All these particles together create into muons ($\mu^+$ and $\mu^-$) and neutrinos ($\nu$ and $\nu^-$). A cascade called an air shower. Measurement of air shower particles can be interpreted in terms of the energy spectrum and primary cosmic ray composition. To determine these measurements we require calculation of fluxes generated via CR nuclei of mass A, charge Z and energy E.

**Figure 7** represents primary cosmic ray flux versus energy of the primary cosmic ray particle. From **Figure 7**, we can see the limit of the energy range upto which magnetic spectrometers work i.e. around E ~ $10^4$ while the pair meter technique works well in a wide energy range from $5 \times 10^4$–$5 \times 10^7$ GeV.

## 4. Results and discussion

In Section 2, we have discussed the limitation of magnetized ICAL detector to be used as a magnetic spectrometer, which limits the efficiency of the detector to discriminate between $\mu+$ and $\mu-$ at higher energies and reconstruct momentum. Variation in efficiency of muon momentum reconstruction as a function of input momentum is shown in **Figure 2**, which shows a clear fall in efficiency for energetic muons. In **Figure 3**, muon track could be seen, which is undeflected for highly energetic muons. Finally, it is concluded that with ICAL detector we can do analysis for muons in the energy range of 1–400GeV. This corresponds to surface muons in the energy range of 1600–2000 GeV, because muons lose around 1600 GeV energy [3] into the rock overburden to reach at the detector from the top of the INO-ICAL surface. ICAL cannot be used as a magnetic spectrometer for highly energetic cosmic ray muons. For energetic (TeV) muons, pair meter technique [2] can be used for momentum reconstruction as discussed in Section 3 [5]. This technique is tested by a few detectors, since INO-ICAL will be large in dimensions so it will be a perfect machine to test the capability of this technique. We have developed a separate Geant4 code for counting the bursts in the iron plates and also a technique to measure the energy of the bursts with the produced electron pairs into the iron plates. In **Figure 6**, we can see the burst of muons in iron plate. The variation of these burst number is shown in **Figure 4**, which is a function of the muon energy.

### 4.1 Summary and conclusions

- The pair meter technique can competently measure muon energy in the energy range of 1–1000 TeV at INO-ICAL detector operating as pair meter.
- One can probe very high energy muon fluxes and primary cosmic rays in the knee region which will aid in accurate background muon and neutrino flux measurement in the forthcoming detectors designed for ultra-high energy neutrino experiments.
- Our Geant4 analyses for central module of INO-ICAL detector are successfully performed and variation in the cascade number of varying energy is observed in the iron plates.

## Acknowledgements

This work is partially supported by Department of Physics, Lucknow University, Department of Atomic Energy, Harish-Chandra Research Institute, Allahabad and INO collaboration. Financially it is supported by government of India, DST project no-SR/MF/PS02/2013, Department of Physics, Lucknow University. We thank Prof. Raj Gandhi for useful discussion and providing hospitality to work in HRI, Dr. Jyotsna Singh for her support and guidance in completing this work from Lucknow University.

## Author details

Jaydip Singh*, Srishti Nagu and Jyotsna Singh
University of Lucknow, Lucknow, India

*Address all correspondence to: jaydip.singh@gmail.com

## References

[1] Ahamed S, Sajjad Atahar M, et al. (INO Collab). Physics potential of the ICAL detector at the Indian based neutrino observatory. 9 May 2017; arXiv:1505.07380

[2] Kokoulin RP, Petrukhin AA. Theory of the pairmeter for high energy muon measurements. Nuclear Instruments and Methods in Physics Research. 1987;**A263**(1988):468-479

[3] Groom DE, Mokhov NV, Striganov S. Muon stopping power and range tables 10 MeV-100 TeV. Atomic Data and Nuclear Data Tables. 2001;**76**(2)

[4] Chatterjee A et al. (INO Collab). JINST 9(2014) PO 7001; July 2014

[5] Gandhi R, Panda S. Probing very high energy prompt muon and neutrino fluxes and the cosmic ray knee via underground muons. 31 August 2006; arXiv:hep-ph/0512179

[6] Chikkatur AP, Bugel L, et al. Test of a calorimetric technique for measuring the energy of cosmic ray muon in TeV energy range. Zeitschrift für Physik. 1997;**74**:279-289

[7] Agostinelli S et al. GEANT4: A simulation toolkit, GEANT4 collaboration. Nuclear Instruments and Methods in Physics Research Section A. 2003;**506**:250 http://geant4.cern.ch/

[8] Singh J, Singh J, et al. Atmospheric muons charge ratio analysis at the INO-ICAL detector. 29 Jun 2018; arXiv:1709.01064

[9] Ramesh N, Hawron M, Martin C, Bachri A. Flux variation of cosmic muons. Journal of the Arkansas Academy of Science. 2011;**65**:67-72

Chapter 3

# From the Eloisatron to the Pevatron

*Thomas Taylor*

## Abstract

In the late 1970s the experimental physics community was active in promoting the Large Electron Positron (LEP) collider and its associated experiments to study the Z- and W-bosons, and with the expectation that the tunnel could subsequently house a hadron collider (LHC), providing a center-of-mass energy for discoveries at the frontier of knowledge. At this time, Antonino Zichichi, who had chaired a Working Group in charge of promoting LEP among the community of experimental and accelerator physicists, realized that one should envisage building as large a ring as possible, for which LEP/LHC would be but a scale model, and it was thus the idea of the Eloisatron, or ELN, in a ring of about 300 km in circumference, was born. CERN and IHEP, China, are now engaged in studies for future colliders of 100 km in circumference, aiming to extend center-of-mass energy in hadron collisions to 100 TeV by using very high field magnets. The ELN idea lives on, but it is time to envision an update. A ring of diameter 300 km would make possible the installation of a sequence of increasingly complex accelerators culminating in one eventually capable of providing a center-of-mass energy of 1000 TeV, i.e. a peta-electron-volt or PeV.

**Keywords:** particle physics, standard model, CERN, colliders, ISR, LEP, LHC, FCC, Eloisatron, 100 TeV, 1 PeV, Pevatron

## 1. Introduction

Following the success of the first hadron collider, the Intersecting Storage Rings (ISR) [1] at CERN in the early 1970s, colliders have been the experimentalists' main tool for exploring, in laboratory conditions, particle physics at the frontier of knowledge. Enthusiasm for the large collider that was to become the Large Electron-Positron collider (LEP), was amplified in 1976 by the workings of the so-called LEP Working Group [2], which produced several visionary reports regarding the future possibilities of an accelerator of about 30 km in circumference [3]. Thanks to technological advances at the ISR, the Z- and W-bosons foreseen in the Standard Model were first observed (1984) in the proton-antiproton collider in the SPS tunnel at CERN [4], before LEP was completed. The lepton collider LEP, an accelerator of 27 km in circumference targeted detailed study of the intermediate bosons that had been previously discovered, providing unprecedented precision that helped to entrench the Standard Model of fundamental physics between 1989 and 2000 as being the best, albeit incomplete, description of the physical world of elementary particles at the present time [5]. In parallel, the feasibility of performing

comparable experiments with leptons with linear colliders was ably demonstrated at SLAC, and a more powerful proton-antiproton collider was put into service at the Fermilab Tevatron [6]. Experimental particle physics had well and truly embraced the advantage of laboratory-based colliders for probing deeper into the unknown. In the quest for still higher center-of-mass energies, the 80 km Superconducting Super Collider (SSC) [7] in the USA was destined to provide conditions for experiments at center-of-mass energies of 25– 30 TeV, but due to funding problems this was not to be. It was therefore at the Large Hadron Collider [8], installed in the LEP tunnel, that events revealing the elusive Higgs boson were observed in 2012 [9]. Now the community is studying the possibility of providing the discovery potential of still higher center-of-mass energies, as well as precision measurements of the Higgs boson in a lepton collider in much the same way as was done at LEP for the Z- and W-bosons.

The idea of the Eloisatron, or ELN, to be installed in a tunnel of about 300 km of circumference, was born in 1979. Zichichi, an experimental physicist who had played an active role in the first g-2 experiment at CERN, and led experiments at the ISR, clearly understood the value of storage rings and colliders. He had been very active in promoting work on LEP and its associated experiments [2]—fully aware of the fact that the tunnel could be used subsequently to house a hadron collider. He realized the importance of equipping as large a ring as possible to enable to perform experiments at the highest possible center-of-mass energy, and for which LEP/LHC would be but a scale model. It was thus that he came up with the idea of the Eloisatron this being the largest that could be accommodated on the island of Sicily. Zichichi argued that such an instrument could be built for roughly the same cost as a bridge that was envisioned to join the island to the mainland, and this and several other sites in Italy were considered (perhaps the most appropriate being in the geologically stable island of Sardinia) [10]. Kjell Johnsen, who had previously led the highly innovative ISR project, was put in charge of the first studies for such an accelerator. However, this was to be overshadowed by work on the ill-fated 83 km Superconducting Synchrotron Collider (SSC) project in the USA, and on the LHC at CERN, only to be revived later in the ephemeral Very Large Hadron Collider (VLHC) studies for a 233 km long collider at Fermilab [11]—itself largely inspired by the Eloisatron concept. Nevertheless, it should be emphasized that it was due to the recognition of the importance of studies on detectors associated with the potential ELN (and *a fortiori* the LHC) that the LAA project was born. This auxiliary project provided the framework for vital work to be performed on detectors, enabling the adoption of techniques to address problems inherent with equipment required to observe very high energy collisions at the LHC [12].

Today we have the LHC, which will be upgraded to provide increased luminosity from 2026. Studies for a future generation of accelerator/colliders focus on either a linear collider (for leptons) aimed at detailed study of the Higgs (or Higgs-like) events seen at the LHC, or a large (100 km) circular collider. The idea is that this would first provide $e^+e^-$ collisions (as a simpler alternative to the linear collider for a so-called Higgs factory), both in the European Future Circular Collider (FCC) and Chinese Circular Electron-Positron Collider (CEPC) versions, to be followed by installing a hadron collider with discovery potential [13, 14]. To achieve a sought-after 100 TeV center-of-mass energy, the new machine would require a large number of yet-to-be-developed, very high field superconducting magnets (16 T dipoles). The experimental physics community hopes that at least one of the large circular machines will be constructed, even if, as likely, it does not quite reach the presently advertised performance, it will allow groundbreaking studies both in particle and in accelerator physics and technology. However, the philosophy behind the idea of the ELN lives on. Closest to the ELN concept, there is a proposal [15] for

a minimum cost route to a 100 TeV center-of-mass hadron collider: the idea being to finish the SCC tunnel in Texas, in which an injector synchrotron would be installed, and to bore a second tunnel, of length 270 km to house the main collider, using affordable 5 T superconducting dipoles. The SCC tunnel could also house an efficient circular $e^+e^-$ collider to be used as a Higgs factory. The terrain in the vicinity of the SCC is propitious for tunneling, the per meter cost being less than that near CERN, at least in the sections of limestone [16] (but for a global costing this would have to be offset by the value of the existing laboratory infrastructure at CERN). However, unlike for LHC, where there was an identified goal (to reveal Higgs), indicating an appropriate energy, it is now desirable to foresee being able to access far higher collision energies, so the goal should perhaps evolve. It is thus proposed that one should consider a ring of about 300 km *in diameter*, enabling the installation of a sequence of accelerators culminating in one capable of achieving a hadronic center-of-mass energy of 1000 TeV, i.e. a PeV, or peta-electron-volt. In this chapter, a vision is presented of what would probably be the world's Ultimate Circular Collider, based on proven and foreseeable accelerator physics and engineering science: i.e. the UCC, or Pevatron.

## 2. The requirement

It is first assumed that a Higgs Factory, either in the form of a linear collider or phase 1 of an FCC or CEPC (or possibly "LEP3", an ultimate $e^+e^-$ collider in the LEP/LHC tunnel) will have done its work before the first phase of experimentation starts at the UCC. While the tunnel could (and should, initially) undoubtedly be used to house an exciting $e^+e^-$ collider, it is supposed to be principally an instrument for performing frontier physics using hadron collisions. The second assumption is that suitable stable sites can be identified for efficiently boring or excavating an approximately circular tunnel of about 300 km in diameter. For the first phase of operation of the hadron collider, the accelerator should be capable of delivering comfortably a center-of-mass energy of 100 TeV in at least two experiments using the simplest (and cheapest) possible guiding magnet system. This accelerator would serve as the injector for subsequent upgrades of the collision energy, culminating in 1000 TeV and (like the FCC) would depend on the development of affordable high performance superconducting material. The first phase would feature extremely simple magnets based on the use of existing low-cost superconductors. This, together with the fact that synchrotron radiation, and other effects associated with the deflection of stiff beams would not be a problem, could mean that the first phase of the proposed machine may even be cost-competitive with the hadron versions of FCC/CEPC. An added incentive to read on....

## 3. The site

There are undoubted advantages in using present laboratory infrastructure if at all possible, as has been done to render the sequence of accelerators at CERN both performant and affordable. The longstanding international nature of Geneva also facilitates the hosting of such a center. It is thus evident that one candidate should be CERN. However, the terrain is not ideal, as the tunnel would have to pass through many kilometers of mixed rock including limestone, which would complicate the process and have clear implications on the scale, cost and timescale of civil engineering. Other sites must therefore be considered for a larger circular accelerator than the FCC, and the cost analysis should consider what would be required to

develop (or establish) suitable infrastructure for another, possibly entirely new, laboratory. As such an accelerator must be a fully international endeavor, and it will certainly take decades to achieve the ultimate goal, mechanisms will have to be enacted that render it attractive and guarantee its perennity. What springs to mind is a development of the successful CERN model, and CERN should most definitely be central to its establishment. Suitable geologically stable sites with good tunneling attributes certainly exist in China, Europe, Russia and the United States, but socio-political support will be as important as geographical location.

Considering the evident urbanization of the planet, this new collider would provide the incentive for a farseeing nation or region to combine the excitement of creating a laboratory to explore the very forefront of natural science, with that of establishing a cluster of cities, including some that are radically new. These should feature all the latest developments in sustainability and form a living exhibition of what can be done to enhance the quality of life and quest for perfection. Besides accelerator scientists and experimental physicists, architects, engineers, social scientists, artists and philosophers should all share the excitement of working together to create such a holistic ensemble showing the way for a harmonious future of the region of the world that is farsighted enough to seize the opportunity. We consider the establishment of at least four major agglomerations, or sub-cities, each housing at least 5 million inhabitants clustered around a circle defined by the accelerator, inter-linked by rapid train and highway systems. Ideally, to facilitate the setting up of the complex, at least one or two of the cities would be developments of existing conurbations. Each city would feature its own local subway system. The airport should be located approximately at the center of the circle with rapid local trains connecting to each of the mainline stations at the city nodes. Such an arrangement is shown schematically in **Figure 1**, but the actual layout would depend on local geography and a consensus based on overall requirements and planning, and responding to the constraints of sustainability, comfort and efficiency. Some of the glue holding the enterprise together would be the pride of hosting a forefront laboratory probing the mysteries of science using a unique instrument. It is confidently expected that such a complex of cities would be a breeding ground for experimentation in urban living as well as in physics research and associated technological developments and would pioneer advances in social well-being as well

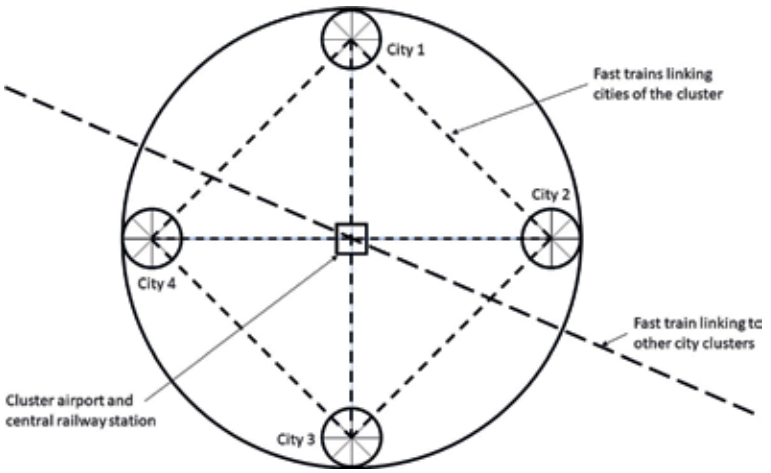


**Figure 1.**
*Schematic layout of a cluster of cities hosting a very large particle accelerator/collider. The large circle represents the main ring. It is supposed that the injector synchrotron would be located at one of the cities, and the two major experiments at two of the other cities.*

as science proper. It has been observed that clustering cities can lead to the creation of hotbeds of efficiency, creativity and innovation, and it is on this premise that China, for example, has already identified 19 regions that it intends to endow with the necessary infrastructure [17]. Other large nations are also considering moving in the same direction. It is opined that the fundamental research orientation of the complex suggested here would be more effective in providing the impetus for getting such a city cluster to work, than either bureaucratic edict or simply hoping that lavish infrastructure would somehow engender efficiency.

## 4. The accelerator/collider complex

It is foreseen that such a collider would be operated in three major phases, each phase taking its performance to new heights.

### 4.1 Phase 1

A large fraction of the experimental particle physics community is presently of the opinion that to provide worthwhile discovery potential the next hadron collider after the LHC should deliver a center-of-mass energy of about 100 TeV. This is the ultimate goal of the FCC as seen today, and it would be the target for the first phase of the UCC. For the 300 km diameter accelerator considered here, this would imply having a main dipole magnet field of 1.7 T. The transmission line magnet (pipetron), first developed for the VLHC study [11] provides such a field very efficiently. As shown in **Figure 2**, this device consists of field-shaping iron poles and yoke excited by a single superconducting cable carrying up to 100 kA and is extremely cost effective. Since the VLHC study, new cables based on magnesium diboride ($MgB_2$) material, which work comfortably at 20 K as opposed to 4.2 K for Nb-Ti, have been developed at CERN for interconnecting equipment required for the luminosity upgrade of the LHC [18]. As the specific heat of metals is proportional to the cube of the absolute temperature, such a cable is very stable, and, compared with the previous study for the VLHC, its use would also lead to a simplification of the associated cryogenic envelope and cooling system. To make best use of this technology the main magnet guiding and focusing system could be of the combined function type featured in the ISR. The estimated cost for such a

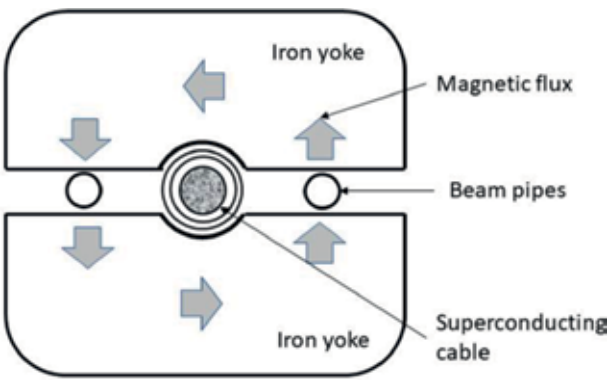


**Figure 2.**
*Schematic cross-section of a transmission line magnet for bending the counter-rotating beams of elementary particles in a collider. The magnet is excited by a large current (about 100 kA) flowing in a superconducting cable. Such a device can deliver a field of up to about 1.7 T—sufficient for delivering a center-of-mass energy of 100 TeV to protons in a collider of 300 km in diameter.*

magnet system for the UCC is of the order of twice the cost of the magnet system for the 8.3 T system for the (very much smaller) LHC, and probably more affordable (and certainly less risky) than that of the presently envisaged high field magnet system for the FCC. The accelerator would require an injector system to supply 4 TeV protons, consisting of a linear accelerator and two pulsed synchrotrons.

### 4.2 Phase 2

By adding a pair of rings, powered by coils wound from classical Nb-Ti conductor cooled to 4.2 T, delivering a dipole field of about 5 T, the second phase of the UCC would provide a center-of-mass energy of up to 330 TeV. By using pre-accelerated beams from the transmission line arrangement, the new magnet system would only be required to increase the momentum of circulating particles by a factor of 3.5 to 4, simplifying the process and enabling the inclusion of beam screen within a relatively small magnet aperture. It is reasonable to assume that, by careful design, the cost per meter of such a magnet system would be less than half that of the LHC system, and as the system is entirely classical, the technological risk would be low. The layout of the transmission line magnet in the tunnel will have to be such that the new magnet system can be installed during shutdowns without disrupting the Phase 1 operation.

### 4.3 Phase 3

It is confidently expected that during the construction and exploitation of phases 1 and 2 of the UCC, a vigorous R&D program on high field superconducting materials, and on their engineering into reliable, cost-effective cables, will have delivered conductors comparable to Nb-Ti today. That being the case, a third set of rings, with dipoles providing fields of up to 18 T, would allow us to envisage a center-of-mass energy of 1000 TeV, or 1 PeV, the ultimate goal of the complex. It is emphasized that such superconductors do not exist at present and that once they have been identified, it will also be necessary to identify a long-term use for the material that generates the need for its engineering development, just as MRI provided the “killer application” for Nb-Ti, and which led to it becoming an affordable commodity. The sole application to particle accelerators, being “one-off” in nature, is not sufficient. The push for increasingly high field magnets for NMR is an immediate application, but essentially small-scale; as seen today, the most likely long-term large-scale application would be for fusion containment—should that develop into a viable energy source. The technological development of such material, identification of applications, and the industrialization of the manufacture are examples of the high-tech activity that one could expect to flourish in the collider city complex.

## 5. The host laboratory

It is generally recognized that CERN provides a good example of how to organize a large international laboratory [19]. This is not an accident. The success of the laboratory is based on a combination of several important principles:

- A simple, well drawn-up convention
- Consistent rules-based funding and purchasing

- Accumulation of skills of the workforce
- Tight technical control of projects
- Skill in the use of infrastructure to build increasingly sophisticated accelerators
- Location in an internationally-oriented city

A new aspiring global laboratory should consider carefully the implication of each of these when planning how to undertake the work.

### 5.1 The convention

The CERN convention is a visionary 32-page document that spells out clearly the purpose of the Organization and the rules for its governance. The governing body is the CERN Council, made up of two delegates from each member state. The Council is assisted by the Finance Committee—which deals with material and personnel budgets, and the Scientific Policy Committee—which advises on the research agenda. The convention is drawn up in such a way as to vest the Council with significant autonomy and authority to negotiate and take decisions in the interest of the Organization, to empower its scientists, and to reduce to a strict minimum the bureaucracy.

### 5.2 Funding

Council allocates the annual budget, with funds provided by the member states in proportion to Net Nation Income. Any activity—in particular research and development—suffers from erratic funding. In the case of CERN this is avoided by a procedure of rolling forecasts: each year the budget for the following year is established, together with firm estimates for the next 2 years and provisional estimates for the following 2 years. This has provided the laboratory with a stable funding profile and enabled planning of both the day-to-day running and that of the medium and long-term scientific program. Purchasing of equipment is subject to strict rules that favor the lowest bid for a supply satisfying carefully drawn-up specifications. While there is not a policy of fair return ("juste retour"), some effort is put into distributing contracts fairly among member states.

### 5.3 Skills

Scientists, engineers and technicians are encouraged to hone their skills through their work on projects. This enables them to write comprehensive specifications for equipment that is available industrially, to follow up constructively the contracts, and to design and prototype special equipment that is not available on the market. The laboratory maintains well-equipped workshops for this purpose and for that of resolving technical problems which may occur due to accidents or malfunction of equipment.

### 5.4 Control

CERN maintains control of projects. The normal way of acquiring equipment is through buying from industry to a tight specification, written by staff competent in the field, and close technical follow-up. Cost is minimized by in-house design and prototyping, and by limiting the risk to manufacturers by confining the

requirement to that of satisfying engineering standards: CERN specifically bears the technical risk for the correct functioning of complex equipment. While the LHC collider was mainly funded via CERN, that of the experiments was mainly financed via the participating institutes and universities, which led to frequent use of "in-kind" supplies. It was found to be necessary to ensure compliance of such equipment by tight control from the host laboratory. For this to work it is essential to have dedicated, competent, experienced and respected staff which is empowered with appropriate authority.

### 5.5 Infrastructure

The maintenance and development of infrastructure is of vital importance for a laboratory. As CERN has evolved, it capitalized on existing accelerators and associated equipment to build successive increasing complex and energetic accelerators and colliders at minimum cost. In parallel, there has been a continuing development in the technology of particle detectors required for the evolving experiments, and of course in that of the supporting informatics hardware and software. The maintenance of efficient and well-equipped workshops has also been of vital importance for the Laboratory. It is an understatement to say that the experience of laboratories established harboring the specific intention of excluding integrated workshops (i.e. relying exclusively on purchasing) has not been good.

### 5.6 Location

Geneva is a city with a long tradition of hosting international organizations. This activity is an important source of income for the city, and it makes a corresponding effort to simplify the bureaucratic problems that can occur with international staffing. Permanent staff is not subject to local income tax, and goods are not subject to value-added tax, which helps to keeps costs under control. The city also has a conveniently located international airport and an efficient public transport system that provides excellent access to the laboratory. The laboratory itself lies astride the frontier between Switzerland and France, so that both countries are in fact host states and provide facilities over and above their reglementary contributions to compensate for the advantages incurred. The country or region wishing to host a laboratory providing facilities for international big science projects is strongly advised to set up a framework of a similar nature.

## 6. City clusters and project funding

One of the reasons for proposing to associate the new collider with a cluster of cities is that it could facilitate the funding. If it is recognized that to host the collider has some value—be it for education, innovation, regional pride or some other factor—then investing in the success of the project could be rendered acceptable, compared with less well-focused requests to central government. Viewed alone, the cost of a very large particle accelerator/collider, just as an array of telescopes for astronomy, or a nuclear fusion device, is perceived to loom large in a national budget, even though much of the cost is simply pumping money around the economy. And to put the figures into perspective, the cost of running CERN, presently the largest collider facility in the world, is equivalent to that of a proverbial annual cup of coffee of the population of the member states—a small price to pay for motivational news generated directly by the laboratory, without considering the economic fall-out, and innovation derived from the activity [20, 21]. The complexity inherent in

the forming of city clusters calls for the injection of capital investment on a huge scale, and the additional percentage cost of hosting a large research facility of the type discussed here would be small, whereas the publicity and enhancement of the attractiveness of the cluster would be considerable. It is anticipated that in the medium term, competition between the clusters will grow, and this will in turn accelerate the performance—and stimulate the desire to host big science projects.

## 7. Conclusion

While the FCC and the CEPC are thought of as being the next, and possibly final step in colliders, these do not reach the size dreamt of already 40 years ago—the Eloisatron, or ELN. The proposal for an accelerator in the USA, using the defunct SSC tunnel to house the injector gets close [15], but in the study presented here the possibility of going still further is addressed. It is suggested that the increasing desire of people to live in cities, and the expected increase in efficiency (and well-being) provided by setting up of clusters of cities, may provide an opportunity to consider associating such a city cluster with a collider that could ultimately deliver interactions at a center-of-mass energy of 1 PeV, the Pevatron.

## Author details

Thomas Taylor[1,2]

1 AT Scientific LLC, Bernex, Switzerland

2 CERN, Geneva, Switzerland

*Address all correspondence to: tom.taylor@cern.ch

## References

[1] Johnsen K. The ISR and accelerator physics. Particle Accelerators. 1986;**18**: 167-182

[2] Zichichi A, editor. ECFA-LEP Working Group 1979 Status Report, ECFA/79/39. 1980

[3] Camilleri L et al. Physics with very high energy $e^+e^-$ colliding beams. CERN 76-18. 1976

[4] Gareyte J. The SPS p-pbar collider. CERN-SPS-84-03-DI-(MST). 1984

[5] Schopper H. LEP—The Lord of the Collider Rings at CERN 1980–2000. Berlin: Springer Verlag; 2009

[6] Wilson RR. The Tevatron. FERMILAB-TM-0753. 1978

[7] Jackson JD, editor. Conceptual design of the superconducting super collider. SSC-SR-2020. 1986

[8] Evans L, editor. The Large Hadron Collider. Lausanne: EPFL Press; 2009

[9] Randall L. Higgs discovery: the power of empty space. London: The Bodley Head; 2012

[10] Barletta WA, Leutz H, editors. Supercolliders and Super-Detectors. Singapore: World Scientific Publishing; 1993

[11] VLHC Design Study Group. Design study for a phased very large hadron collider. Fermilab-TM-2149. 2001

[12] Zichichi A et al. The LAA Project—Report No. 1. CERN/LAA. 1986

[13] Bogomyagkov AV et al. Projects for ultra-high-energy circular colliders at CERN. Physics of Particles and Nuclei Letters. 2016;**13**(7):870-875

[14] CEPC-SppC Preliminary conceptual design report, volume II: accelerator. Beijing: Institute of High Energy Physics, CAS; October 2015

[15] Assadi S, McIntyre P, et al. Higgs factory and 100 TeV hadron collider: Opportunity for a new world laboratory within a decade. 2014. Available from: https://arxiv.org/pdf/1402.5973

[16] Ballantyne B. Future proof. London: World Market Intelligence Ltd., Tunnels and Tunnelling; June 2016

[17] A tale of 19 megacities. London: The Economist magazine; June 23, 2018

[18] Ballarino A. Design of an $MgB_2$ feeder system to connect groups of superconducting magnets to remote power converters. Journal of Physics: Conference Series. 2010;**234**:032003

[19] Fabjan CF et al., editors. Technology Meets Research. Singapore: World Scientific Publishing; 2016

[20] Schmied H. A study of the economic utility resulting from CERN contracts. CERN-1975-005. 1975

[21] Barbalat O. Technology transfer from particle physics: The CERN experience 1974–1997. CERN-BLIT-97-1. 1997

Chapter 4

# Flavor Physics and Charged Particle

*Takaaki Nomura*

## Abstract

We have new charged particles in many scenarios of physics beyond the Standard Model where these particles are sometimes motivated to explain experimental anomalies. Furthermore, such new charged particles are important target at the collider experiments such as the Large Hadron Collider in searching for a signature of new physics. If these new particles interact with known particles in the Standard Model, they would induce interesting phenomenology of flavor physics in both lepton and quark sectors. Then, we review some candidate of new charged particles and its applications to flavor physics. In particular, vector-like lepton and leptoquarks are discussed for lepton flavor physics and $B$-meson physics.

**Keywords:** flavor physics, charged particle from beyond the standard model, $B$-meson decay, vector-like lepton/quark, leptoquarks, charged scalar boson

## 1. Introduction

Charged particles are often considered in the physics beyond the Standard Model (BSM) of particle physics as new heavy particles which are not observed at the experiments. Such charged particles can have rich phenomenology since it would interact with particles in the Standard Model (SM). Furthermore they are motivated to explain some experimental anomalies indicating deviation from predictions in the SM. For example, some charged particle interaction can accommodate with the anomalous magnetic moment of the muon, $(g-2)_\mu$, which shows a long-standing discrepancy between experimental observations [1, 2] and theoretical predictions [3–6],

$$\Delta a_\mu \equiv \Delta a_\mu^{\text{exp}} - \Delta a_\mu^{\text{th}} = (28.8 \pm 8.0) \times 10^{-10}, \tag{1}$$

where $a_\mu = (g-2)_\mu/2$. This difference reaches to $3.6\sigma$ deviation from the prediction. In addition, new charged particles are introduced when we try to explain anomalies in $B$-meson decay like $B \to K^{(*)}\mu^+\mu^-$ and $B \to D^{(*)}\tau\nu$ [7–16].

In this chapter, we review some candidates of new charged particles from BSM physics. After listing some examples of them, the applications to some flavor physics will be discussed focusing on some specific cases. We find it interesting to consider new charged particles which are related to flavor physics in both lepton and quark sectors.

## 2. Some charged particles from beyond the standard model physics

In this section we review some examples of charged particles which are induced from BSM physics.

### 2.1 Charged scalar bosons

Singly charged scalar appears from two-Higgs doublet model (2HDM) [17, 18] in which two $SU(2)_L$ doublet Higgs fields are introduced:

$$H_1 = \begin{pmatrix} H_1^+ \\ (v_1 + \phi_1 + i\eta_1)/\sqrt{2} \end{pmatrix}, \quad H_2 = \begin{pmatrix} H_2^+ \\ (v_2 + \phi_2 + i\eta_2)/\sqrt{2} \end{pmatrix}, \tag{2}$$

where $v_{1,2}$ is the vacuum expectation values (VEVs) of Higgs fields. In general, one can write Yukawa interaction in terms of Higgs doublet fields as

$$\begin{aligned} -\mathcal{L}_Y = &\overline{Q}_L Y_1^d D_R H_1 + \overline{Q}_L Y_2^d D_R H_2 + \overline{Q}_L Y_1^u U_R \tilde{H}_1 + \overline{Q}_L Y_2^u U_R \tilde{H}_2 \\ &+ \overline{L} Y_1^\ell \ell_R H_1 + \overline{L} Y_2^\ell \ell_R H_2 + H.c., \end{aligned} \tag{3}$$

where all flavor indices are hidden, $P_{R(L)} = (1 \pm \gamma_5)/2$; $Q_L^i = \left(u_L^i, d_L^i\right)$ and $L_L = \left(\nu_L^i, e_L^i\right)$ are the $SU(2)_L$ quark and lepton doublets with flavor index $i$, respectively; $f_R$ $(f = U, D, \ell)$ denotes the $SU(2)_L$ singlet fermion; $Y_{1,2}^f$ are the $3 \times 3$ Yukawa matrices; and $\tilde{H}_i = i\tau_2 H_i^*$ with $\tau_2$ being the Pauli matrix. There are two CP-even scalars, one CP-odd pseudoscalar, and two charged Higgs particles in the 2HDM, and the relations between physical and weak eigenstates can be given by

$$\begin{aligned} h &= -s_\alpha \phi_1 + c_\alpha \phi_2, \\ H &= c_\alpha \phi_1 + s_\alpha \phi_2, \\ H^\pm(A) &= -s_\beta \phi_1^\pm(\eta_1) + c_\beta \phi_2^\pm(\eta_2), \end{aligned} \tag{4}$$

where $\phi_i(\eta_i)$ and $\eta_i^\pm$ denote the real (imaginary) parts of the neutral and charged components of $H_i$, respectively; $c_\alpha(s_\alpha) = \cos\alpha(\sin\alpha)$, $c_\beta = \cos\beta = v_1/v$, $s_\beta = \sin\beta = v_2/v$, and $v_i$ are the vacuum expectation values (VEVs) of $H_i$ and $v = \sqrt{v_1^2 + v_2^2} \approx 246$ GeV. In our notation, $h$ is the SM-like Higgs, while $H$, $A$, and $H^\pm$ are new particles which appear in the 2HDM. In particular, Yukawa interactions with charged Higgs are given by

$$\begin{aligned} -\mathcal{L}_Y^{H^\pm} = &\sqrt{2}\,\overline{d}_L V^\dagger \left[-\frac{1}{v t_\beta} \mathrm{m_u} + \frac{\mathbf{X}^u}{s_\beta}\right] u_R H^- \\ &+ \sqrt{2}\overline{u}_L V \left[-\frac{t_\beta}{v} \mathrm{m_d} + \frac{\mathbf{X}^d}{c_\beta}\right] d_R H^+ \\ &+ \sqrt{2}\overline{\nu}_L \left[-\frac{t_\beta}{v} \mathrm{m}_\ell + \frac{\mathbf{X}^\ell}{c_\beta}\right] \ell_R H^+ + H.c., \end{aligned} \tag{5}$$

where $V$ is the CKM matrix and the matrix $\mathbf{X}^f$ is defined by original Yukawa coupling and unitary matrix diagonalizing fermion mass

$$\mathbf{X}^{\mathrm{u}} = V_L^u \frac{Y_1^u}{\sqrt{2}} V_R^{u\dagger}, \;\; \mathbf{X}^{\mathrm{d}} = V_L^d \frac{Y_2^d}{\sqrt{2}} V_R^{d\dagger}, \;\; \mathbf{X}^{\ell} = V_L^{\ell} \frac{Y_2^{\ell}}{\sqrt{2}} V_R^{\ell\dagger}. \tag{6}$$

A doubly charged scalar boson also appears from $SU(2)_L$ triplet scalar field:

$$\Delta = \begin{pmatrix} \delta^+/\sqrt{2} & \delta^{++} \\ (v_\Delta + \delta^0 + i\eta^0)/\sqrt{2} & -\delta^+/\sqrt{2} \end{pmatrix}, \tag{7}$$

where $v_\Delta$ is the VEV of the triplet scalar. Such a triplet scalar is motivated to generate neutrino mass known as Higgs triplet model or type-II seesaw mechanism [19–26]. We can write Yukawa interaction of triplet scalar and lepton doublets by

$$L_Y = h_{ij} L_{L_i}^T C i\sigma_2 \Delta L_{L_j} + h.c. \;, \tag{8}$$

where $L_{L_i} = (\nu_i, \ell_i)_L^T$ with flavor index $i$ and $C = i\gamma^2\gamma^0$ is the Dirac charge conjugation operator. In terms of the components, the Yukawa interaction can be expanded as

$$\begin{aligned} L_Y = h_{ij}\Big( &-\frac{1}{\sqrt{2}} \ell_{iL}^T C\delta^+ \nu_{jL} - \ell_{iL}^T C\delta^{++} \ell_{jL} + \nu_{iL}^T C\delta^0 \nu_{jL} - \frac{1}{\sqrt{2}} \nu_{iL}^T C\delta^+ \ell_{jL} \Big) \\ + h_{ji}^* \Big( &\frac{1}{\sqrt{2}} \nu_{iL}^\dagger C\delta^- \ell_{jL}^* + \ell_{iL}^\dagger C\delta^{--} \ell_{jL}^* - \nu_{iL}^\dagger C\delta^0 \nu_{jL}^* + \frac{1}{\sqrt{2}} \ell_{iL}^\dagger C\delta^- \nu_{jL}^* \Big) \end{aligned} \tag{9}$$

where $C^\dagger = -C$ is used. Another example of model including doubly charged scalar is Zee-Babu type model [27, 28] for neutrino mass generation at two-loop level. In such a type of model, one introduces singly and doubly charged scalars $(h^\pm, k^{\pm\pm})$ which are $SU(2)_L$ singlet. The Yukawa couplings associated with charged scalar fields are given by

$$L_Y = f_{ij} \overline{L}_{L_i}^c (i\sigma_2) L_{L_j} h^+ + g_{ee} \overline{e}_R^c e_R k^{++} + g_{ij} \overline{e}_{R_i}^c e_{R_j} k^{++} + h.c., \tag{10}$$

where $f_{ij}$ is antisymmetric under flavor indices. These Yukawa interactions can be used to generate neutrino mass with the nontrivial interaction in scalar potential:

$$V \supset \mu k^{++} h^- h^- + c.c.. \tag{11}$$

Note that these charged scalars also contribute to lepton flavor violation processes.

### 2.2 Vector-like leptons

The vector-like leptons (VLLs) are discussed in Ref. [29]. They are new charged particles without conflict of gauge anomaly problem and induce rich lepton flavor physics. To obtain mixing with the SM leptons, the representations of VLL under $SU(2)_L \times U(1)_Y$ gauge symmetry can be singlet, doublet, and triplet under $SU(2)_L$. In order to avoid the stringent constraints from rare $Z \to \ell_i^\pm \ell_j^\mp$ decays, we here consider the triplet representations $(1, 3, -1)$ and $(1, 3, 0)$ with hypercharges $Y = -1$ and $Y = 0$, respectively. The new Yukawa couplings thus can be written such that

$$-\mathcal{L}_Y = \overline{L}\mathbf{Y}_1 \Psi_{1R} H + \overline{L}\mathbf{Y}_2 \Psi_{2R} \tilde{H} + m_{\Psi_1} Tr\overline{\Psi}_{1L}\Psi_{1R} + m_{\Psi_2} Tr\overline{\Psi}_{2L}\Psi_{2R} + H.c., \tag{12}$$

where we have suppressed the flavor indices; $H$ is the SM Higgs doublet field, $\tilde{H} = i\tau_2 H^*$ and the neutral component of Higgs field is $H^0 = (v+h)/\sqrt{2}$. The representations of two VLLs are

$$\Psi_1 = \begin{pmatrix} \Psi_1^-/\sqrt{2} & \Psi_1^0 \\ \Psi_1^{--} & -\Psi_1^-/\sqrt{2} \end{pmatrix}, \quad \Psi_2 = \frac{1}{\sqrt{2}} \begin{pmatrix} \Psi_2^0/\sqrt{2} & \Psi_2^+ \\ \Psi_2^- & -\Psi_2^0/\sqrt{2} \end{pmatrix}, \tag{13}$$

with $\Psi_2^+ = C\overline{\Psi}_2^-$ and $\Psi_2^0 = C\overline{\Psi}_2^0$. Since $\Psi_2$ is a real representation of $SU(2)_L$, the factor of $1/\sqrt{2}$ in $\Psi_2$ is required to obtain the correct mass term for Majorana fermion $\Psi_2^0$. Due to the new Yukawa terms of $\mathbf{Y}_{1,2}$, the heavy neutral and charged leptons can mix with the SM leptons, after electroweak symmetry breaking (EWSB). Then the lepton mass matrices become $5 \times 5$ matrices and are expressed by

$$M_\ell = \begin{pmatrix} \mathbf{m}_\ell & \mathbf{Y}^\ell v \\ 0 & \mathbf{m}_\Psi \end{pmatrix}, \quad M_\nu = \begin{pmatrix} \mathbf{m}_\nu & \mathbf{Y}^\nu v \\ 0 & \mathbf{m}_\Psi \end{pmatrix}, \tag{14}$$

where the basis is chosen such that the SM lepton mass matrices are in diagonalized form, $\mathrm{m}_\ell$ is the SM charged lepton mass matrix, $\mathbf{m}_\Psi = \mathrm{diag}(m_{\Psi_1}, m_{\Psi_2})$, and

$$\mathbf{Y}^\ell = \frac{1}{2} \begin{pmatrix} -Y_{11} & Y_{21} \\ -Y_{12} & Y_{22} \\ -Y_{13} & Y_{23} \end{pmatrix}, \quad \mathbf{Y}^\nu = \sqrt{2} \begin{pmatrix} Y_{11} & Y_{21}/2 \\ Y_{12} & Y_{22}/2 \\ Y_{13} & Y_{23}/2 \end{pmatrix}. \tag{15}$$

Note that the elements of $\mathbf{Y}^\chi$ should be read as $Y_{ij} = (\mathbf{Y}_i)_j$, where the index $i = 1, 2$ distinguishes the Yukawa couplings of the different VLLs and the index $j = 1, 2, 3$ stands for the flavors of the SM leptons.

To diagonalize $M_\ell$ and $M_\nu$, the unitary matrices $V_{R,L}^\chi$ with $\chi = \ell, \nu$ so that $M_\chi^{\mathrm{dia}} = V_L^\chi M_\chi V_R^{\chi\dagger}$ are introduced. The information of $V_L^\chi$ and $V_R^\chi$ can be obtained from $M_\chi M_\chi^\dagger$ and $M_\chi^\dagger M_\chi$, respectively. According to Eq. (14), it can be found that the flavor mixings between heavy and light leptons in $V_R^\chi$ are proportional to the lepton masses. Since the neutrino masses are tiny, it is a good approximation to assume $V_R^\nu \approx 1$. If one further sets $m_e = m_\mu = 0$ in our phenomenological analysis, only $\tau$-related processes have significant contributions among them. Unlike $V_R^\chi$, the off-diagonal elements in flavor-mixing matrices $V_L^\chi$ are associated with $\mathbf{Y}_{1,2}v/\mathrm{m}_\Psi$. In principle, the mixing effects can be of the order of 0.1 without conflict. In our example later, we examine these effects on $h \to \tau\mu$. To be more specific, we choose parametrization that the unitary matrices in terms of $\mathbf{Y}_{1,2}$ as

$$V_L^\chi \approx \begin{pmatrix} 1_{3\times3} - \varepsilon_L^\chi \varepsilon_L^{\chi\dagger}/2 & -\varepsilon_L^\chi \\ \varepsilon_L^{\chi\dagger} & 1_{3\times3} - \varepsilon_L^{\chi\dagger}\varepsilon_L^\chi/2 \end{pmatrix}, \quad V_R^\ell \approx \begin{pmatrix} 1_{3\times3} & -\varepsilon_R^\ell \\ \varepsilon_R^{\ell\dagger} & 1_{3\times3} \end{pmatrix}, \tag{16}$$

where $V_R^\nu \approx 1$ is used in our approximation, $\varepsilon_L^\chi \approx v\mathbf{Y}^\chi/\mathbf{m}_\Psi$, and $\varepsilon_R^\ell \approx v\mathbf{m}_\ell^\dagger \mathbf{Y}^\ell/\mathbf{m}_\Psi^2$. Combining the SM Higgs couplings and new Yukawa couplings of Eq. (12), the Higgs couplings to all singly charged leptons are obtained such as

$$-\mathcal{L}_{h\ell'\ell'} = h\overline{\ell}'_L V_L^\ell \begin{pmatrix} \mathbf{m}_\ell/v & \mathbf{Y}^\ell \\ 0 & 0 \end{pmatrix} V_R^{\ell\dagger} \ell'_R + H.c., \tag{17}$$

where $\ell'^T = (e,\mu,\tau,\tau',\tau'')$ is the state of a physical charged lepton in lepton flavor space. We use the notations of $\tau'$ and $\tau''$ to denote the heavy-charged VLLs in mass basis. Using the parametrization of Eq. (16), the Higgs couplings to the SM-charged leptons can be formulated by

$$\begin{aligned} -\mathcal{L}_{h\ell\ell} &= C^h_{ij}\overline{\ell}_{iL}\ell_{jR}h + H.c., \\ C^h_{ij} &= \frac{m_{\ell j}}{v}\left[\delta_{ij} - \frac{3}{8}\left(\frac{v^2 Y_{1i}Y_{1j}}{m^2_{\Psi_1}} + \frac{v^2 Y_{2i}Y_{2j}}{m^2_{\Psi_2}}\right)\right]. \end{aligned} \tag{18}$$

If one sets $m_e = m_\mu = 0$, it is clear that in addition to the coupling $h\tau\tau$ being modified, the tree-level flavor-changing couplings $h$- $\tau$- $\mu$ and $h$- $\tau$- $e$ are also induced, and the couplings are proportional to $m_\tau/v \approx 7.2 \times 10^{-3}$. In order to study the VLL contributions to $h \to \gamma\gamma$, the couplings for $h\tau'\tau'$ and $h\tau''\tau''$ are expressed as

$$-\mathcal{L}_{h\Psi\Psi} = \frac{v\sum_i Y^2_{1i}}{2m_{\Psi_1}}h\tau'\tau' + \frac{v\sum_i Y^2_{2i}}{2m_{\Psi_2}}h\tau''\tau''. \tag{19}$$

### 2.3 Vector-like quarks

Here we consider vector-like triplet quarks (VLTQs) that are discussed in Ref. [30] The gauge invariant Yukawa couplings of VLTQs to the SM quarks, to the SM Higgs doublet and to the new Higgs singlet field are written as

$$\begin{aligned} -\mathcal{L}^Y_{VLTQ} &= \overline{Q}_L\mathbf{Y}_1F_{1R}\tilde{H} + \overline{Q}_L\mathbf{Y}_2F_{2R}H + \tilde{y}_1 Tr(\overline{F}_{1L}F_{1R})S + \tilde{y}_2 Tr(\overline{F}_{2L}F_{2R})S \\ &\quad + M_{F_1}Tr(\overline{F}_{1L}F_{1R}) + M_{F_2}Tr(\overline{F}_{2L}F_{2R}) + h.c., \end{aligned} \tag{20}$$

where $Q_L$ is the left-handed SM quark doublet and it could be regarded as mass eigenstate before VLTQs are introduced; here all flavor indices are hidden, $\tilde{H} = i\tau_2 H^*$, and $F_{1(2)}$ is the $2 \times 2$ VLTQ with hypercharge $2/3(-1/3)$. The representations of $F_{1,2}$ in $SU(2)_L$ are expressed in terms of their components as follows:

$$F_1 = \begin{pmatrix} U_1/\sqrt{2} & X \\ D_1 & -U_1/\sqrt{2} \end{pmatrix}, \quad F_2 = \begin{pmatrix} D_2/\sqrt{2} & U_2 \\ Y & -D_2/\sqrt{2} \end{pmatrix}. \tag{21}$$

The electric charges of $U_{1,2}$, $D_{1,2}$, $X$, and $Y$ are found to be $2/3$, $-1/3$, $5/3$, and $-4/3$, respectively. Therefore, $U_{1,2}(D_{1,2})$ could mix with up (down) type SM quarks. Here $M_{F_{1(2)}}$ is the mass of VLTQ, and due to the gauge symmetry, the VLTQs in the same multiplet state are degenerate. By the Yukawa couplings of Eq. (20), the $5 \times 5$ mass matrices for up and down type quarks are found by

$$\begin{aligned} M_u &= \begin{pmatrix} (\mathbf{m}^{\text{dia}}_u)_{3\times3} & v\mathbf{Y}_1/2 & v\mathbf{Y}_2/\sqrt{2} \\ \hline 0_{2\times3} & & (\mathbf{m}_F)_{2\times2} \end{pmatrix}, \\ M_d &= \begin{pmatrix} (\mathbf{m}^{\text{dia}}_d)_{3\times3} & v\mathbf{Y}_1/\sqrt{2} & -v\mathbf{Y}_2/2 \\ \hline 0_{2\times3} & & (\mathbf{m}_F)_{2\times2} \end{pmatrix}, \end{aligned} \tag{22}$$

where $\left(\mathbf{m}_u^{\rm dia}\right)_{3\times3}$ and $\left(\mathbf{m}_d^{\rm dia}\right)_{3\times3}$ denote the diagonal mass matrices of SM quarks and $\mathrm{dia}(m_F)_{2\times2} = (m_{F_1}, m_{F_2})$. Notice that a non-vanished $v_s$ could shift the masses of VLTQs. Since $v_s \ll v$, we neglect the small effects hereafter. Due to the presence of $\mathbf{Y}_{1,2}$, the SM quarks, $U_{1,2}$, and $D_{1,2}$ are not physical states; thus one has to diagonalize $M_u$ and $M_d$ to get the mass eigenstates in general. If $vY^i_{1,2} \ll m_{F_{1,2}}$, we expect that the off-diagonal elements of unitary matrices for diagonalizing the mass matrices should be of order of $vY^i_{1,2}/m_{F_{1,2}}$. By adjusting $Y^i_{1,2}$, the off-diagonal effects could be enhanced and lead to interesting phenomena in collider physics.

## 2.4 Scalar leptoquarks

In this subsection we consider leptoquarks (LQs) which are discussed for example in Refs. [31, 32]. The three LQs are $\Phi_{7/6} = (2, 7/6)$, $\Delta_{1/3} = (3, 1/3)$, and $S^{1/3} = (1, 1/3)$ under $\left(SU(2)_L, U(1)_Y\right)$ SM gauge symmetry, where the doublet and triplet representations can be taken as

$$\Phi_{7/6} = \begin{pmatrix} \phi^{5/3} \\ \phi^{2/3} \end{pmatrix}, \quad \Delta_{1/3} = \begin{pmatrix} \delta^{1/3}/\sqrt{2} & \delta^{4/3} \\ \delta^{-2/3} & -\delta^{1/3}/\sqrt{2} \end{pmatrix}, \tag{23}$$

where the superscripts are the electric charges of the particles. Accordingly, the LQ Yukawa couplings to the SM fermions are expressed as

$$\begin{aligned} -L_{LQ} = {} & \left[\overline{u}\,\mathbf{V}\mathbf{k}P_R\ell\phi^{5/3} + \overline{d}\,\mathbf{k}P_R\ell\phi^{2/3}\right] + \left[-\overline{\ell}\,\tilde{\mathbf{k}}P_R u\phi^{-5/3} + \overline{\nu}\,\tilde{\mathbf{k}}P_R u\phi^{-2/3}\right] \\ & + \left[\overline{u^c}\,\mathbf{V}^*\mathbf{y}P_L\nu\delta^{-2/3} - \frac{1}{\sqrt{2}}\overline{u^c}\,\mathbf{V}^*\mathbf{y}P_L\ell\delta^{1/3} - \frac{1}{\sqrt{2}}\overline{d^c}\,\mathbf{y}P_L\nu\delta^{1/3} - \overline{d^c}\,\mathbf{y}P_L\ell\delta^{4/3}\right], \\ & + \left(\overline{u^c}\,\mathbf{V}^*\tilde{\mathbf{y}}P_L\ell - \overline{d^c}\,\tilde{\mathbf{y}}P_L\nu + \overline{u^c}\mathbf{w}P_R\ell\right)S^{1/3} + h.c., \end{aligned} \tag{24}$$

where the flavor indices are hidden, $\mathbf{V} \equiv U^u_L U^{d\dagger}_L$ denotes the Cabibbo-Kobayashi-Maskawa (CKM) matrix, $U^{u,d}_L$ are the unitary matrices used to diagonalize the quark mass matrices, and $U^d_L$ and $U^u_R$ have been absorbed into $\mathbf{k}$, $\tilde{\mathbf{k}}$, $\mathbf{y}$, $\tilde{\mathbf{y}}$, and $\mathbf{w}$. In this setup, we treat the neutrinos as massless particles and their flavor mixing effects are rotated away as an approximation. There is no evidence for any new CP violation, so in the following, we treat the Yukawa couplings as real numbers for simplicity.

The scalar LQs can also couple to the SM Higgs field via the scalar potential, and the cross section for the Higgs to diphoton can be modified in principle. However,

| **Particle type** | $(SU(3), SU(2), U(1)_Y)$ | **Examples of application** |
|---|---|---|
| Charged scalar | $(1,3,1)$, $(1,2,1/2)$ | Neutrino mass, lepton flavor violation |
| Vector-like lepton | $(1,3,-1)$, $(1,3,0)$ | Lepton flavor violation |
| Vector-like quark | $(3,3,2/3)$, $(3,3,-1/3)$ | Quark flavor physics |
| Scalar leptoquark | $(3,2,7/6)$, $(3,3,1/3)$, $(3,1,1/3)$ | Meson decay, lepton flavor violation |

**Table 1.**
*List of examples of charged particles from new physics discussed in this review showing $SU(3) \times SU(2) \times U(1)_Y$ representations and applications to phenomenology.*

the couplings of the LQs to the Higgs are independent parameters and irrelevant to the flavors, so by taking proper values for the parameters, the signal strength parameter for the Higgs to diphoton can fit the LHC data. For detailed analysis see **Table 1** in Ref. [31].

## 3. Examples of applying charged particles to flavor physics

In this section, we review applications of charged particles to flavor physics by considering VLLs and LQs as examples.

### 3.1 Flavor physics from vector-like lepton

Introduction of VLLs contributes to lepton flavor physics via Yukawa interactions discussed in previous section. Here we review the leptonic decay of the SM Higgs and LFV decay of charged lepton as an illustration based on Ref. [29].

#### *3.1.1 Modification to $h \to \tau^+\tau^-$ branching ratio*

From Eq. (18), it can be seen that the modified Higgs couplings to the SM leptons are proportional lepton masses. By comparison with other lepton channels, it can be seen that the $\tau\tau$ mode is the most significant one, and thus we estimate the influence on $h \to \tau^+\tau^-$. Using the values that satisfy $BR(h \to \mu\tau) \approx 10^{-4}$, the deviation of $\Gamma(h \to \tau^+\tau^-)$ from the SM prediction can be obtained as

$$\kappa_{\tau\tau} \equiv \frac{\Gamma(h \to \tau^+\tau^-)}{\Gamma^{SM}(h \to \tau^+\tau^-)} = \left|1 - \frac{6v^2 Y_3^2}{8m_\Psi^2}\right|^2 \approx 0.88. \tag{25}$$

If the SM Higgs production cross section is not changed, the signal strength for $pp \to h \to \tau^+\tau^-$ in our estimation is $\mu_{\tau\tau} \approx 0.88$, where the measurements from ATLAS and CMS are $1.44^{+0.42}_{-0.37}$ [33] and $0.91 \pm 0.27$ [34], respectively. Although the current data errors for the $\tau\tau$ channel are still large, the precision measurement of $\mu_{\tau\tau}$ can test the effect or give strict limits on the parameters.

#### *3.1.2 $\tau \to \mu\gamma$ process in vector-like lepton model*

In the following, we investigate the contributions of new couplings in Eq. (18) to the rare tau decays and to the flavor-conserving muon anomalous magnetic moment. We first investigate the muon $g-2$, denoted by $\Delta a_\mu$. The lepton flavor-changing coupling $h\mu\tau$ can provide contribution to $\Delta a_\mu$ through the Higgs-mediated loop diagrams. However, as shown in Eq. (18), the induced couplings are associated with $m_{\ell j}/v\overline{\ell}_{Li}\ell_{Rj}$; only the right-handed tau lepton has a significant contribution. The induced $\Delta a_\mu$ is thus suppressed by the factor of $m_\mu^2 m_\tau/(v m_h^2)$ so that the value of $\Delta a_\mu$ is two orders of magnitude smaller than current data $\Delta a_\mu = a_\mu^{exp} - a_\mu^{SM} = (28.8 \pm 8.0) \times 10^{-10}$ [2]. A similar situation happens in $\tau \to 3\mu$ decay also. Since the couplings are suppressed by $m_\tau/v$ and $m_\mu/v$, the BR for $\tau \to 3\mu$ is of the order of $10^{-14}$. We also estimate the process $\tau \to \mu\gamma$ via the $h$-mediation. The effective interaction for $\tau \to \mu\gamma$ is expressed by

$$\mathcal{L}_{\tau\to\mu\gamma} = \frac{e}{16\pi^2} m_\tau \overline{\mu}\sigma_{\mu\nu}(C_L P_L + C_R P_R)\tau F^{\mu\nu}, \tag{26}$$

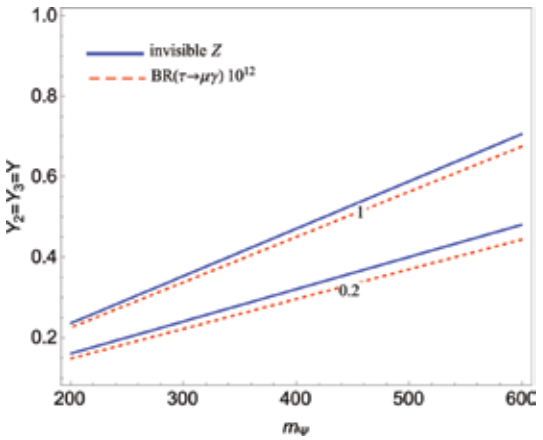


**Figure 1.**
*Contours for $BR(\tau \to \mu\gamma)$ (dashed) as a function of Y and $m_\Psi$, where the constraint from $\Gamma^Z_{inv}$ (solid) is included. (The plot is taken from ref. [29]).*

where $C_L = 0$ and the Wilson coefficient $C_R$ from the one loop is obtained as

$$C_R \approx \frac{C^h_{23} C^h_{33}}{2m_h^2}\left(\ln\frac{m_h^2}{m_\tau^2} - \frac{4}{3}\right). \tag{27}$$

Accordingly, the BR for $\tau \to \mu\gamma$ is expressed as

$$\frac{BR(\tau \to \mu\gamma)}{BR(\tau \to e\bar{\nu}_e\nu_\tau)} = \frac{3\alpha_e}{4\pi G_F^2}|C_R|^2. \tag{28}$$

We present the contours for $BR(\tau \to \mu\gamma)$ as a function of coupling $Y$ and $m_\Psi$ in **Figure 1**, where the numbers on the plots are in units of $10^{-12}$. It can be seen that the resultant $BR(\tau \to \mu\gamma)$ can be only up to $10^{-12}$, where the current experimental upper bound is $BR(\tau \to \mu\gamma) < 4.4 \times 10^{-8}$ [2].

### 3.2 $B$-meson flavor physics with leptoquarks

This section is based on Ref. [32]. Several interesting excesses in semileptonic $B$ decays have been observed in experiments such as (i) the angular observable $P_5'$ of $B \to K^*\mu^+\mu^-$ [7], where a $3\sigma$ deviation due to the integrated luminosity of 3.0 fb $^{-1}$ was found at the LHCb [8, 9], and the same measurement with a $2.6\sigma$ deviation was also confirmed by Belle [10] and (ii) the branching fraction ratios $R_{D,D^*}$, which are defined and measured as follows:

$$\begin{aligned}
R_D &= \frac{\overline{B} \to D\tau\nu}{\overline{B} \to D\ell\nu} = \begin{cases} 0.375 \pm 0.064 \pm 0.026 & \text{Belle [11]}, \\ 0.440 \pm 0.058 \pm 0.042 & \text{BaBar [12, 13]}, \end{cases} \\
R_{D^*} &= \frac{\overline{B} \to D^*\tau\nu}{\overline{B} \to D^*\ell\nu} = \begin{cases} 0.302 \pm 0.030 \pm 0.011 & \text{Belle [14]}, \\ 0.270 \pm 0.035 \pm^{+0.028}_{-0.025} & \text{Belle [15]}, \\ 0.332 \pm 0.024 \pm 0.018 & \text{BaBar [12, 13]}, \\ 0.336 \pm 0.027 \pm 0.030 & \text{LHCb [16]}, \end{cases}
\end{aligned} \tag{29}$$

where $\ell = (e, \mu)$, and these measurements can test the violation of lepton flavor universality. The averaged results from the heavy flavor averaging group are $R_D = 0.403 \pm 0.040 \pm 0.024$ and $R_{D^*} = 0.310 \pm 0.015 \pm 0.008$ [35], and the SM predictions are around $R_D \approx 0.3$ [36, 37] and $R_{D^*} \approx 0.25$, respectively. Further tests of lepton flavor universality can be made using the branching fraction ratios: $R_{K^{(*)}} = BR(B \to K^{(*)}\mu^+\mu^-)/BR(B \to K^{(*)}e^+e^-)$. The current LHCb measurements are $R_K = 0.745^{+0.090}_{-0.074} \pm 0.036$ [38] and $R_{K^*} = 0.69^{+0.11}_{-0.07} \pm 0.05$ [39], which indicate a more than $2.5\sigma$ deviation from the SM prediction. Furthermore, a known anomaly is the muon anomalous magnetic dipole moment (muon $g-2$), where its latest measurement is $\Delta a_\mu = a_\mu^{exp} - a_\mu^{SM} = (28.8 \pm 8.0) \times 10^{-10}$ [2]. These anomalies would be explained by introducing LQs and we review possible scenarios in the following.

### *3.2.1 Effective interactions for semileptonic B-decay*

According to the interactions in Eq. (24), we first formulate the four-Fermi interactions for the $b \to c\ell'\overline{\nu}_{\ell'}$ and $b \to s\ell'^+\ell'^-$ decays. For the $b \to c\ell'\overline{\nu}_{\ell'}$ processes, the induced current-current interactions from $k_{3j}\tilde{k}_{i2}$ and $\tilde{y}_{3i}w_{2j}$ are $(S-P)\times(S-P)$, and those from $y_{3i}y_{2j}$ and $\tilde{y}_{3i}\tilde{y}_{2j}$ are $(S-P)\times(S+P)$, where $S$ and $P$ denote the scalar and pseudoscalar currents, respectively. Taking the Fierz transformations, the Hamiltonian for the $b \to c\ell'\overline{\nu}_{\ell'}$ decays can be expressed as follows:

$$\begin{aligned}\mathcal{H}_{b\to c} =& \left(-\frac{\tilde{y}_{3i}w_{2j}}{2m_S^2} + \frac{k_{3j}\tilde{k}_{i2}}{2m_\Phi^2}\right)\overline{c}P_L b\,\overline{\ell}_j P_L \nu_i + \left(\frac{\tilde{y}_{3i}w_{2j}}{2m_S^2} + \frac{k_{3j}\tilde{k}_{i2}}{2m_\Phi^2}\right)\frac{1}{4}\overline{c}\sigma_{\mu\nu}P_L b\,\overline{\ell}_j\sigma^{\mu\nu}P_L\nu_i \\ &- \sum_a V_{2a}\frac{y_{aj}y_{3i}}{4m_\Delta^2}\overline{c}\gamma_\mu P_L b\,\overline{\ell}_j\gamma^\mu P_L\nu_i + \sum_a V_{2a}\tilde{y}_{aj}\frac{\tilde{y}_{3i}}{2m_S^2}\overline{c}\gamma_\mu P_L b\,\overline{\ell}_j\gamma^\mu P_L\nu_i,\end{aligned} \tag{30}$$

where the indices $i, j$ are the lepton flavors and the LQs in the same representation are taken as degenerate particles in mass. It can be seen that the interaction structure obtained from the triplet LQ is the same as that from the $W$-boson one. The doublet LQ generates an $(S-P)\times(S-P)$ structure as well as a tensor structure. However, the singlet LQ can produce currents of $(V-A)\times(V-A)$, $(S-P)\times(S-P)$, and tensor structures. Nevertheless, we show later that the singlet LQ makes the main contribution to the $R_D$ and $R_{D^*}$ excesses. Note that it is difficult to explain $R_{D,D^*}$ by only using the doublet or/and triplet LQs when the $R_K$ excess and other strict constraints are satisfied at the same time.

With the Yukawa couplings in Eq. (24), the effective Hamiltonian for the $b \to s\ell'^+\ell'^-$ decays mediated by $\phi^{2/3}$ and $\delta^{4/3}$ can be expressed as

$$\begin{aligned}\mathcal{H}_{b\to s} =& \frac{k_{3j}k_{2j}}{2m_\Phi^2}(\bar{s}\gamma^\mu P_L b)(\overline{\ell}_j\gamma_\mu P_R\ell_j), \\ &- \frac{y_{3j}y_{2j}}{2m_\Delta^2}(\bar{s}\gamma^\mu P_L b)(\overline{\ell}_j\gamma_\mu P_L\ell_j),\end{aligned} \tag{31}$$

where the Fierz transformations have been applied. By Eq. (31), it can be clearly seen that the quark currents from both the doublet and triplet LQs are left-handed; however, the lepton current from the doublet (triplet) LQ is right(left)-handed. When one includes Eq. (31) in the SM contributions, the effective Hamiltonian for the $b \to s\ell'^+\ell'^-$ decays is written as

$$\mathcal{H}_{b\to s} = \frac{G_F \alpha_{em} V_{tb} V_{ts}^*}{\sqrt{2}\pi} \left[ H_{1\mu} L^{\mu} + H_{2\mu} L^{5\mu} \right], \tag{32}$$

where the leptonic currents are denoted by $L_{\mu}^{(5)} = \overline{\ell}\gamma_{\mu}(\gamma_5)\ell$, and the related hadronic currents are defined as

$$\begin{aligned} H_{1\mu} &= C_9^{\ell} \bar{s}\gamma_{\mu} P_L b - \frac{2m_b}{q^2} C_7 \bar{s} i\sigma_{\mu\nu} q^{\nu} P_R b, \\ H_{2\mu} &= C_{10}^{\ell} \bar{s}\gamma_{\mu} P_L b. \end{aligned} \tag{33}$$

The effective Wilson coefficients with LQ contributions are expressed as

$$\begin{aligned} C_{9(10)}^{\ell} &= C_{9(10)}^{SM} + C_{9(10)}^{LQ,\ell'}, \\ C_9^{LQ,\ell_j} &= -\frac{1}{4c_{SM}} \left( \frac{k_{3j}k_{2j}}{m_{\Phi}^2} - \frac{y_{3j}y_{2j}}{m_{\Delta}^2} \right), \\ C_{10}^{LQ,\ell_j} &= -\frac{1}{4c_{SM}} \left( \frac{k_{3j}k_{2j}}{m_{\Phi}^2} + \frac{y_{3j}y_{2j}}{m_{\Delta}^2} \right), \end{aligned} \tag{34}$$

where $c_{SM} = V_{tb}V_{ts}^* \alpha_{em} G_F / \left(\sqrt{2}\pi\right)$ and $V_{ij}$ is the CKM matrix element. From Eq. (34), it can be seen that when the magnitude of $C_{10}^{LQ,\ell_j}$ is decreased, $C_9^{LQ,\ell_j}$ can be enhanced. That is, the synchrony of the increasing/decreasing Wilson coefficients of $C_9^{NP}$ and $C_{10}^{NP}$ from new physics is diminished in this model. In addition, the sign of $C_9^{LQ,\ell'}$ can be different from that of $C_{10}^{LQ,\ell'}$. As a result, when the constraint from $B_s \to \mu^+\mu^-$ decay is satisfied, we can have sizable values of $C_9^{LQ,\mu}$ to fit the anomalies of $R_K$ and angular observable in $B \to K^*\mu^+\mu^-$. Although the LQs can contribute to the electromagnetic dipole operators, since the effects are through one-loop diagrams and are also small, the associated Wilson coefficient $C_7$ is mainly from the SM contributions.

### 3.2.2 Constraints from $\Delta F = 2$, radiative lepton flavor violating, $B^+ \to K^+\nu\overline{\nu}$, $B_s \to \mu^+\mu^-$, and $B_c \to \tau\nu$ processes

Before we analyze the muon $g-2$, $R_{D^{(*)}}$, and $R_{K^{(*)}}$ problems, we examine the possible constraints due to rare decay processes. Firstly, we discuss the strict constraints from the $\Delta F = 2$ processes, such as $F - \overline{F}$ oscillation, where $F$ denotes the neutral pseudoscalar meson. Since $K - \overline{K}$, $D - \overline{D}$, and $B_d - \overline{B}_d$ mixings are involved, the first-generation quarks and the anomalies mentioned earlier are associated with the second- and third-generation quarks. Therefore, we can avoid the constraints by assuming that $k_{1\ell'} \approx \tilde{k}_{\ell'1} \approx y_{1\ell'} \approx \tilde{y}_{1\ell'} \approx w_{1i} \approx 0$ without affecting the analyses of $R_{D^{(*)}}$ and $R_{K^{(*)}}$. Thus, the relevant $\Delta F = 2$ process is $B_s - \overline{B}_s$ mixing, where $\Delta m_{B_s} = 2|\langle \overline{B}_s|\mathcal{H}|B_s\rangle|$ is induced from box diagrams, and the LQ contributions can be formulated as

$$\begin{aligned} \Delta m_{B_s} \approx & \frac{C_{box}}{(4\pi)^2} \left[ \frac{5}{4} \left( \frac{\sum_{i=1}^3 y_{3i}y_{2i}}{m_{\Delta}} \right)^2 + \left( \frac{\sum_{i=1}^3 k_{3i}k_{2i}}{m_{\Phi}} \right)^2 \right] \\ & + \frac{C_{box}}{(4\pi)^2} \left[ \left( \frac{\sum_{i=1}^3 \tilde{y}_{3i}\tilde{y}_{2i}}{m_S} \right)^2 + 2\frac{\left(\sum_{i=1}^3 y_{3i}\tilde{y}_{2i}\right)\left(\sum_{i=1}^3 \tilde{y}_{3i}y_{2i}\right)}{m_S^2 - m_{\Delta}^2} \ln\left[\frac{m_S}{m_{\Delta}}\right] \right], \end{aligned} \tag{35}$$

where $C_{box} = m_{B_s} f_{B_s}^2/3, f_{B_s} \approx 0.224$ GeV is the decay constant of $B_s$-meson [40], and the current measurement is $\Delta m_{B_s}^{exp} = 1.17 \times 10^{-11}$ GeV [2]. To satisfy the $R_{K^{(*)}}$ excess, the rough magnitude of LQ couplings is $|y_{3i} y_{2i}| \sim |k_{3i} k_{2i}| \sim 5 \times 10^{-3}$. Using our parameter values, it can be shown that the resulting $\Delta m_{B_s}$ agree with the current experimental data. However, $\Delta m_{B_s}$ can indeed constrain the parameters involved in the $b \to c\ell'\bar{\nu}_{\ell'}$ decays.

In addition to the muon $g-2$, the introduced LQs can also contribute to the lepton flavor violating processes $\ell' \to \ell\gamma$, where the current upper bounds are $BR(\mu \to e\gamma) < 4.2 \times 10^{-13}$ and $BR(\tau \to e(\mu)\gamma) < 3.3(4.4) \times 10^{-8}$ [2], and they can strictly constrain the LQ couplings. To understand the constraints due to the $\ell' \to \ell\gamma$ decays, one expresses their branching ratios (BRs) such as

$$BR(\ell_b \to \ell_a \gamma) = \frac{48\pi^3 \alpha_{em} C_{ba}}{G_F^2 m_{\ell_b}^2} \left( \left|(a_R)_{ab}\right|^2 + \left|(a_L)_{ab}\right|^2 \right) \tag{36}$$

with $C_{\mu e} \approx 1$, $C_{\tau e} \approx 0.1784$, and $C_{\tau\mu} \approx 0.1736$. $(a_R)_{ab}$ is written as

$$(a_R)_{ab} \approx \frac{3}{(4\pi)^2} \int d[X]\, m_t \left(F_{k\tilde{k}} - F_{w\tilde{y}}\right)_{ab}, \tag{37}$$

where $\int [dX] \equiv \int dxdydz(1-x-y-z)$, $(a_L)_{ab}$ can be obtained from $(a_R)_{ab}$ by using $\left(F_{\alpha\beta}^{\dagger}\right)_{ab}$ instead of $\left(F_{\alpha\beta}\right)_{ab}$, and the function $F_{k\tilde{k}}$ is given by

$$\begin{aligned} \left(F_{k\tilde{k}}\right)_{ab} &= (\mathbf{Vk})_{3b} \tilde{k}_{a3} \left( \frac{5}{3} \frac{x}{\Delta(m_t, m_\Phi)_{ab}} + \frac{2}{3} \frac{1-x}{\Delta(m_\Phi, m_t)_{ab}} \right), \\ \left(F_{w\tilde{y}}\right)_{ab} &= w_{3b} \left(\mathbf{V}\tilde{\mathbf{y}}\right)_{3a} \left( \frac{1}{3} \frac{x}{\Delta(m_t, m_S)_{ab}} + \frac{2}{3} \frac{1-x}{\Delta(m_S, m_t)_{ab}} \right), \\ \Delta(m_1, m_2)_{ab} &\approx x m_1^2 + (y+z) m_2^2. \end{aligned} \tag{38}$$

Note that $\mathbf{Vk}_{3b} \approx k_{3b}$ and $\mathbf{V}\tilde{\mathbf{y}}_{3a} \approx \tilde{y}_{3a}$ are due to $V_{ub,cb} \ll V_{tb} \approx 1$. From Eq. (24), we can see that the doublet and singlet LQs can simultaneously couple to both left- and right-handed charged leptons, and the results are enhanced by $m_t$. Other LQ contributions are suppressed by $m_\ell$ due to the chirality flip in the external lepton legs, and thus they are ignored. Based on Eq. (37), the muon $g-2$ can be obtained as

$$\Delta a_\mu \simeq -m_\mu (a_L + a_R)_{a=b=\mu}. \tag{39}$$

As mentioned earlier, the singlet LQ does not contribute to $b \to s\ell'^+\ell^-$ at the tree level, but it can induce the $b \to s\nu\bar{\nu}$ process, where the current upper bound is $B^+ \to K^+\nu\bar{\nu} < 1.6 \times 10^{-5}$, and the SM result is around $4 \times 10^{-6}$. Thus, $B^+ \to K^+\nu\bar{\nu}$ can bound the parameters of $\tilde{y}_{3i}\tilde{y}_{2i}$. The four-Fermi interaction structure, which is induced by the LQ, is the same as that induced by the $W$-boson, so we can formulate the BR for $B^+ \to K^+\nu\bar{\nu}$ as

$$BR(B^+ \to K^+\nu\bar{\nu}) \approx \frac{1}{3} \left( \sum_{\ell'} |1 - r_{\ell'}|^2 \right) BR^{SM}(B^+ \to K^+\nu\bar{\nu}), \tag{40}$$

$$r_{\ell'} = \frac{1}{C_{SM}^{\nu}} \left( \frac{\tilde{y}_{3\ell'}\tilde{y}_{2\ell'}}{2m_S^2} + \frac{y_{3\ell'}y_{2\ell'}}{4m_\Delta^2} \right), \quad C_{SM}^{\nu} = \frac{G_F V_{tb} V_{ts}^*}{\sqrt{2}} \frac{\alpha_{em}}{2\pi \sin^2\theta_W} X(x_t), \tag{41}$$

where $x_t = m_t^2/m_W^2$ and $X(x_t)$ can be parameterized as $X(x_t) \approx 0.65 x_t^{0.575}$ [41]. According to Eq. (31), the LQs also contribute to $B_s \to \mu^+\mu^-$ process, where the BRs measured by LHCb [42] and prediction in the SM [43] are $BR(B_s \to \mu^+\mu^-)^{exp} = \left(3.0 \pm 0.6^{+0.3}_{-0.2}\right) \times 10^{-9}$ and $BR(B_s \to \mu^+\mu^-)^{SM} = (3.65 \pm 0.23) \times 10^{-9}$, respectively. The experimental data are consistent with the SM prediction, and in order to consider the constraint from $B_s \to \mu^+\mu^-$, we use the expression for the BR as [44].

$$\frac{\mathrm{BR}(B_s \to \mu^+\mu^-)}{\mathrm{BR}(B_s \to \mu^+\mu^-)^{SM}} = \left|1 - 0.24 C_{10}^{LQ,\mu}\right|^2. \tag{42}$$

In addition to the $B^- \to D^{(*)}\tau\overline{\nu}$ decay, the induced effective Hamiltonian in Eq. (30) also contributes to the $B_c \to \tau\overline{\nu}$ process, where the allowed upper limit is $BR\left(B_c^- \to \tau\overline{\nu}\right) < 30\%$ [45]. According to previous results given by [45], we express the BR for $B_c \to \tau\overline{\nu}$ as

$$BR(B_c \to \tau\overline{\nu}_\tau) = \tau_{B_c} \frac{m_{Bc} m_\tau^2 f_{B_c}^2 G_F^2 |V_{cb}|^2}{8\pi} \left(1 - \frac{m_\tau^2}{m_{B_c}^2}\right)^2 \left|1 + \varepsilon_L + \frac{m_{B_c}^2}{m_\tau(m_b + m_c)} \varepsilon_P\right|^2, \tag{43}$$

where $f_{B_c}$ is the $B_c$ decay constant, and the $\varepsilon_{L,P}$ in our model is given as

$$\varepsilon_L = \frac{\sqrt{2}}{4G_F V_{cb}} \left[-\sum_a V_{2a} \frac{y_{a3} y_{33}}{4m_\Delta^2} + \sum_a V_{2a} \frac{\tilde{y}_{a3}\tilde{y}_{33}}{2m_S^2}\right],$$
$$\varepsilon_P = \frac{\sqrt{2}}{4G_F V_{cb}} \left[\frac{\tilde{y}_{33} w_{23}}{2m_S^2} - \frac{k_{33}\tilde{k}_{32}}{2m_\Phi^2}\right].$$

Using $\tau_{B_c} \approx 0.507 \times 10^{-12}$ s, $m_{B_c} \approx 6.275$ GeV, $f_{B_c} \approx 0.434$ GeV [46], and $V_{cb} \approx 0.04$, the SM result is $BR^{SM}(B_c \to \tau\overline{\nu}_\tau) \approx 2.1\%$. One can see that the effects of the new physics can enhance the $B_c \to \tau\overline{\nu}_\tau$ decay by a few factors at most in our analysis.

### *3.2.3 Observables: $R_{D^{(*)}}$ and $R_{K^{(*)}}$*

The observables of $R_{D^{(*)}}$ and $R_{K^{(*)}}$ are the branching fraction ratios that are insensitive to the hadronic effects giving clearer test of lepton universality in $B$-meson decay, but the associated BRs still depend on the transition form factors. In order to calculate the BR for each semileptonic decay process, we parameterize the transition form factors for $\overline{B} \to P$ by

$$\langle P(p_2)|q\gamma^\mu b|\overline{B}(p_1)\rangle = F_+(q^2)\left((p_1 + p_2)^\mu - \frac{m_B^2 - m_P^2}{q^2} q^\mu\right) + \frac{m_B^2 - m_P^2}{q^2} q^\mu F_0(q^2),$$
$$\langle P(p_2)|q\sigma_{\mu\nu} b|\overline{B}(p_1)\rangle = -i\left(p_{1\mu} p_{2\nu} - p_{1\nu} p_{2\mu}\right) \frac{2F_T(q^2)}{m_B + m_P}, \tag{44}$$

where $P$ can be the $D(q = c)$ or $K(q = s)$ meson and the momentum transfer is given by $q = p_1 - p_2$. For the $B \to V$ decay where $V$ is a vector meson, the transition form factors associated with the weak currents are parameterized such that

$$\begin{aligned}
\langle V(p_2,\varepsilon)|\overline{q}\gamma_\mu b|\overline{B}(p_1)\rangle &= i\varepsilon_{\mu\nu\rho\sigma}\varepsilon^{\nu*}p_1^\rho p_2^\sigma \frac{2V(q^2)}{m_B+m_V},\\
\langle V(p_2,\varepsilon)|\overline{q}\gamma_\mu\gamma_5 b|\overline{B}(p_1)\rangle &= 2m_V A_0(q^2)\frac{\varepsilon^*\cdot q}{q^2}q_\mu + (m_B+m_V)A_1(q^2)\left(\varepsilon_\mu^* - \frac{\varepsilon^*\cdot q}{q^2}q_\mu\right)\\
&\quad - A_2(q^2)\frac{\varepsilon^*\cdot q}{m_B+m_V}\left((p_1+p_2)_\mu - \frac{m_B^2-m_V^2}{q^2}q_\mu\right),\\
\langle V(p_2,\varepsilon)|\overline{q}\sigma_{\mu\nu} b|\overline{B}(p_1)\rangle &= \varepsilon_{\mu\nu\rho\sigma}\left[\varepsilon^{\rho*}(p_1+p_2)^\sigma T_1(q^2) + \varepsilon^{\rho*}q^\sigma\frac{m_B^2-m_V^2}{q^2}\left(T_2(q^2)-T_1(q^2)\right)\right.\\
&\quad \left. +2\frac{\varepsilon^*\cdot q}{q^2}p_1^\rho p_2^\sigma\left(T_2(q^2)-T_1(q^2)+\frac{q^2}{m_B^2-m_V^2}T_3(q^2)\right)\right],
\end{aligned} \tag{45}$$

where $V = D^*(K^*)$ when $q = c(s)$, $\varepsilon^{0123} = 1$, $\sigma_{\mu\nu}\gamma_5 = (i/2)\varepsilon_{\mu\nu\rho\sigma}\sigma^{\rho\sigma}$, and $\varepsilon^\mu$ is the polarization vector of the vector meson. Here we note that the form factors associated with the weak scalar/pseudoscalar currents can be obtained through the equations of motion, i.e., $i\partial_\mu\overline{q}\gamma^\mu b = (m_b - m_q)\overline{q}b$ and $i\partial_\mu(\overline{q}\gamma^\mu\gamma_5 b) = -(m_b+m_q)\overline{q}\gamma_5 b$. For numerical estimations, the $q^2$-dependent form factors $F_+$, $F_T$, $V$, $A^0$, and $T_1$ are taken as [47]

$$f(q^2) = \frac{f(0)}{(1-q^2/M^2)(1-\sigma_1 q^2/M^2+\sigma_2 q^4/M^4)}, \tag{46}$$

and the other form factors are taken to be

$$f(q^2) = \frac{f(0)}{1-\sigma_1 q^2/M^2+\sigma_2 q^4/M^4}. \tag{47}$$

The values of $f(0)$, $\sigma_1$, and $\sigma_2$ for each form factor are summarized in **Table 2**. A detailed discussion of the form factors can be referred to [47]. The next-to-next-leading (NNL) effects obtained with the LCQCD Some Rule approach for the $B \to D$ form factors were described by [48].

According to the form factors in Eqs. (44) and (45), and the interactions in Eqs. (30) and (32), we briefly summarize the differential decay rates for the semileptonic $B$ decay processes, which we use for estimating $R_{D^{(*)}}$ and $R_K$. For the $\overline{B} \to D\ell'\overline{\nu}_{\ell'}$ decay, the differential decay rate as a function of the invariant mass $q^2$ can be given by

| | $B \to D$ | | | $B \to D^*$ | | | | | | |
|---|---|---|---|---|---|---|---|---|---|---|
| | $F_+$ | $F_0$ | $F_T$ | $V$ | $A_0$ | $A_1$ | $A_2$ | $T_1$ | $T_2$ | $T_3$ |
| f(0) | 0.67 | 0.67 | 0.69 | 0.76 | 0.69 | 0.66 | 0.62 | 0.68 | 0.68 | 0.33 |
| $\sigma_1$ | 0.57 | 0.78 | 0.56 | 0.57 | 0.58 | 0.78 | 1.40 | 0.57 | 0.64 | 1.46 |
| $\sigma_2$ | | | | | | | 0.41 | | | |
| | $B \to K$ | | | $B \to K^*$ | | | | | | |
| f(0) | 0.36 | 0.36 | 0.35 | 0.44 | 0.45 | 0.36 | 0.32 | 0.39 | 0.39 | 0.27 |
| $\sigma_1$ | 0.43 | 0.70 | 0.43 | 0.45 | 0.46 | 0.64 | 1.23 | 0.45 | 0.72 | 1.31 |
| $\sigma_2$ | | 0.27 | | | | 0.36 | 0.38 | | 0.62 | 0.41 |

**Table 2.**
*$B \to P, V$ transition form factors, as parameterized in Eqs. (46) and (47).*

$$\frac{d\Gamma_D^{\ell'}}{dq^2} = \frac{G_F^2|V_{cb}|^2\sqrt{\lambda_D}}{256\pi^3 m_B^3}\left(1-\frac{m_{\ell'}^2}{q^2}\right)^2\left[\frac{2}{3}\left(2+\frac{m_{\ell'}^2}{q^2}\right)\left|X_+^{\ell'}\right|^2+\frac{2m_{\ell'}^2}{q^2}\left|X_0^{\ell'}+\frac{\sqrt{q^2}}{m_{\ell'}}X_S^{\ell'}\right|^2\right.$$
$$\left.+16\left(\frac{2}{3}\left(1+\frac{2m_{\ell'}^2}{q^2}\right)\left|X_T^{\ell'}\right|^2-\frac{m_{\ell'}}{\sqrt{q^2}}X_T^{\ell'}X_0^{\ell'}\right)\right], \tag{48}$$

where the $\left\{X_\alpha^{\ell'}\right\}$ functions and LQ contributions are

$$\begin{aligned}
X_+^{\ell'} &= \sqrt{\lambda_D}\left(1+C_V^{\ell'}\right)F_+(q^2), \quad X_0^{\ell'} = \left(m_B^2-m_D^2\right)\left(1+C_V^{\ell'}\right)F_0(q^2)\\
X_S^{\ell'} &= \frac{m_B^2-m_D^2}{m_b-m_c}C_S^{\ell'}\sqrt{q^2}F_0(q^2), \quad X_T^{\ell'} = -\frac{\sqrt{q^2\lambda_D}}{m_B+m_D}C_T^{\ell'}F_T(q^2)\\
C_V^{\ell'} &= \frac{\sqrt{2}}{8G_FV_{cb}}\sum_a V_{2a}\left(\frac{\tilde{y}_{3\ell'}\tilde{y}_{a\ell'}}{m_S^2}-\frac{y_{3\ell'}y_{a\ell'}}{2m_\Delta^2}\right),\\
C_S^{\ell'} &= -\frac{\sqrt{2}}{4G_FV_{cb}}\left(\frac{\tilde{y}_{3\ell'}w_{2\ell'}}{2m_S^2}-\frac{k_{3\ell'}\tilde{k}_{\ell'2}}{2m_\Phi^2}\right), \quad C_T^{\ell'} = \frac{\sqrt{2}}{16G_FV_{cb}}\left(\frac{\tilde{y}_{3\ell'}w_{2\ell'}}{2m_S^2}+\frac{k_{3\ell'}\tilde{k}_{\ell'2}}{2m_\Phi^2}\right),\\
\lambda_H &= m_B^4+m_H^4+q^4-2\left(m_B^2m_H^2+m_H^2q^2+q^2m_B^2\right).
\end{aligned} \tag{49}$$

We note that the effective couplings $C_S^{\ell'}$ and $C_T^{\ell'}$ at the $m_b$ scale can be obtained from the LQ mass scale via the renormalization group (RG) equation. Our numerical analysis considers the RG running effects with $\left(C_S^{\ell'}/C_T^{\ell'}\right)_{\mu=m_b}/\left(C_S^{\ell'}/C_T^{\ell'}\right)_{\mu=\mathcal{O}(\mathrm{TeV})} \sim 2.0$ at the $m_b$ scale [49]. The $\overline{B}\to D^*\ell'\overline{\nu}_{\ell'}$ decays involve $D^*$ polarizations and more complicated transition form factors, so the differential decay rate determined by summing all of the $D^*$ helicities are

$$\frac{d\Gamma_{D^*}^{\ell'}}{dq^2} = \sum_{h=L,+,-}\frac{d\Gamma_{D^*}^{\ell'h}}{dq^2} = \frac{G_F^2|V_{cb}|^2\sqrt{\lambda_{D^*}}}{256\pi^3 m_B^3}\left(1-\frac{m_{\ell'}^2}{q^2}\right)^2\sum_{h=L,+,-}V_{D^*}^{\ell'h}(q^2), \tag{50}$$

where $\lambda_{D^*}$ is found in Eq. (53) and the detailed $\left\{V_{D^*}^{\ell'h}\right\}$ functions are shown in the appendix. According to Eqs. (48) and (50), $R_M$ $(M = D, D^*)$ can be calculated by

$$R_M = \frac{\int_{m_\tau^2}^{q^2_{\max}} dq^2\left(d\Gamma_M^\tau/dq^2\right)}{\int_{m_\ell^2}^{q^2_{\max}} dq^2\left(d\Gamma_M^\ell/dq^2\right)} \tag{51}$$

where $q^2_{\max} = (m_B - m_M)^2$ and $\Gamma_M^\ell = \left(\Gamma_M^e+\Gamma_M^\mu\right)/2$. For the $B\to K\ell^+\ell^-$ decays, the differential decay rate can be expressed as [50].

$$\begin{aligned}
\frac{d\Gamma_{K\ell\ell}(q^2)}{dq^2} &\approx \frac{|c_{\mathrm{SM}}|^2 m_B^3}{3\cdot 2^8\pi^3}\left(1-\frac{q^2}{m_B^2}\right)^{3/2}\\
&\times\left[\left|C_9^\ell F_+(q^2)+\frac{2m_bC_7}{m_B+m_K}F_T(q^2)\right|^2+\left|C_{10}^\ell F_+(q^2)\right|^2\right].
\end{aligned} \tag{52}$$

From Eq. (52), the measured ratio $R_K$ in the range $q^2 = \left[q^2_{\min}, q^2_{\max}\right] = [1, 6]$ GeV$^2$ can be estimated by

$$R_K = \frac{\int_{q^2_{\min}}^{q^2_{\max}} dq^2 d\Gamma_{K\mu\mu}/dq^2}{\int_{q^2_{\min}}^{q^2_{\max}} dq^2 d\Gamma_{Kee}/dq^2}. \tag{53}$$

$R_{K^*}$ is similar to $R_K$, and thus we only show the result for $R_K$.

### *3.2.4 Numerical analysis*

After discussing the possible constraints and observables of interest, we now present the numerical analysis to determine the common parameter region where the $R_{D^{(*)}}$ and $R_{K^{(*)}}$ anomalies can fit the experimental data. Before presenting the numerical analysis, we summarize the relevant parameters, which are related to the specific measurements as follows:

$$\begin{aligned} &\text{muon } g-2 : k_{32}\tilde{k}_{23}, \tilde{y}_{32}w_{32}; \quad R_K : k_{3\ell}k_{2\ell}, y_{3\ell}y_{2\ell}; \\ &R_{D^{(*)}} : k_{3\ell'}\tilde{k}_{\ell'2}, \sum_a V_{2a}\left(y_{3\ell'}y_{a\ell'}, \tilde{y}_{3\ell'}\tilde{y}_{a\ell'}\right), \tilde{y}_{3\ell'}w_{2\ell'}. \end{aligned} \tag{54}$$

The parameters related to the radiative LFV, $\Delta B = 2$, and $B^+ \to K^+\nu\bar{\nu}$ processes are defined as

$$\begin{aligned} &\mu \to e\gamma : k_{32}\tilde{k}_{13}, \tilde{k}_{23}k_{31}, \tilde{y}_{32}w_{31}, w_{32}\tilde{y}_{31}; \\ &\tau \to \ell_a\gamma : k_{33}\tilde{k}_{a3}, \tilde{k}_{33}k_{3a}, \tilde{y}_{33}w_{3a}, w_{33}\tilde{y}_{3a}; \\ &B^+ \to K^+\nu\bar{\nu} : \tilde{y}_{3i}\tilde{y}_{2i}, y_{3i}y_{2i}; \quad B_s \to \mu^+\mu^- : k_{32}k_{22}, y_{32}y_{22}; \\ &\Delta m_{B_s} : \left(\sum_i z_{3i}z_{2i}\right)^2, \left(\sum_i y_{3i}\tilde{y}_{2i}\right)\left(\sum_i \tilde{y}_{3i}y_{2i}\right), \end{aligned} \tag{55}$$

where $z_{3i}z_{2i} = k_{3i}k_{2i}, y_{3i}y_{2i}, \tilde{y}_{3i}\tilde{y}_{2i}$. From Eqs. (54) and (55), we can see that in order to avoid the $\mu \to e\gamma$ and $\tau \to \ell\gamma$ constraints and obtain a sizable and positive $\Delta a_\mu$, we can set $(\tilde{k}_{13,33}, k_{31,33}, w_{3i})$ as a small value. From the upper limit of $B^+ \to K^+\nu\bar{\nu}$, we obtain $\tilde{y}_{3i}\tilde{y}_{2i} < 0.03$, and thus the resulting $\Delta m_{B_s}$ is smaller than the current data. In order to further suppress the number of free parameters and avoid large fine-tuning of couplings, we employ the scheme with $k_{ij} \approx \tilde{k}_{ji} \approx |y_{ij}|$, where the sign of $y_{ij}$ can be selected to obtain the correct sign for $C_9^{LQ,\ell_j}$ and to decrease the value of $C_{10}^{LQ,\mu}$ so that $B_s \to \mu^+\mu^-$ can fit the experimental data. As mentioned above, to avoid the bounds from the $K$, $B_d$, and $D$ systems, we also adopt $k_{1\ell'} \approx \tilde{k}_{\ell'1} \approx y_{1i} \approx \tilde{y}_{1i} \approx w_{1i} \sim 0$. When we omit these small coupling constants, the correlations of the parameters in Eqs. (54) and (55) can be further simplified as

$$\begin{aligned} &\text{muon } g-2 : k_{32}\tilde{k}_{23}; \quad R_K : k_{32}k_{22}, \quad y_{32}y_{22}; R_{D^{(*)}} : k_{32}k_{22}, y_{32}y_{22}, \tilde{y}_{3\ell'}w_{2\ell'}; \\ &B_s \to \mu^+\mu^- : k_{32}k_{22}, y_{32}y_{22}; \quad \Delta m_{B_s} : (k_{32}k_{22})^2, \left(y_{32}y_{22}\right)^2, \end{aligned} \tag{56}$$

where $\tilde{y}_{3i}\tilde{y}_{2i}$ are ignored due to the constraint from $B^+ \to K^+\nu\bar{\nu}$. The typical values of these parameters for fitting the anomalies in the $b \to s\mu^+\mu^-$ decay are $y_{32}(k_{32}), y_{22}(k_{22}) \sim 0.07$, so the resulting $\Delta m_{B_s}$ is smaller than the current data, but

these parameters are too small to explain $R_{D^{(*)}}$. Thus, we must depend on the singlet LQ to resolve the $R_D$ and $R_{D^*}$ excesses, where the main free parameters are now $\tilde{y}_{3\ell'} w_{2\ell'}$.

After discussing the constraints and the correlations among various processes, we present the numerical analysis. There are several LQs in this scenario, but we use $m_{LQ}$ to denote the mass of all LQs. From Eqs. (37), (39), and (56), we can see that the muon $g-2$ depends only on $k_{32}\tilde{k}_{23}$ and $m_\Phi$. Here we illustrate $\Delta a_\mu$ as a function of $k_{32}\tilde{k}_{23}$ in **Figure 2(a)**, where the solid, dashed, and dotted lines denote the results for $m_\Phi = 1.5$, 5, and 10 TeV, respectively, and the band is the experimental value with $1\sigma$ errors. Due to the $m_t$ enhancement, $k_{32}\tilde{k}_{23} \sim 0.05$ with $m_\Phi \sim 1$ TeV can explain the muon $g-2$ anomaly.

According to the relationships shown in Eq. (56), $R_K$, $B_s \to \mu^+\mu^-$, and $\Delta m_{B_s}$ depend on the same parameters, i.e., $k_{32}k_{22}$ and $y_{32}y_{22}$. We show the contours for these observables as a function of $k_{32}k_{22}$ and $y_{32}y_{22}$ in **Figure 2(b)**, where the data with $1\sigma$ errors and $m_{LQ} = 1.5$ TeV are taken for all LQ masses. Based on these results, we see that $\Delta m_{B_s} < \Delta m_{B_s}^{exp}$ in the range of $|k_{32}k_{22}|$, $|y_{32}y_{22}| < 0.05$, where $R_K$ and $BR(B_s \to \mu^+\mu^-)$ can both fit the experimental data simultaneously. In addition, we show $C_9^{LQ,\mu} = [-1.5, -0.5]$ in the same plot. We can see that $C_9^{LQ,\mu} \sim -1$, which is used to explain the angular observable $P_5'$, can also be achieved in the same common region. According to **Figure 2(b)**, the preferred values of $k_{32}k_{22}$ and $y_{32}y_{22}$ where the observed $R_K$ and $B_s \to \mu^+\mu^-$ and the $C_9^{LQ,\mu} = [-1.5, -0.5]$ overlap are around $(k_{32}k_{22}, y_{32}y_{22}) \sim (-0.001, 0.004)$ and $\sim (0.025, 0.03)$. The latter values are at the percentage level, but they are still not sufficiently large to explain the tree-dominated $R_D$ and $R_{D^*}$ anomalies.

After studying the muon $g-2$ and $R_K$ anomalies, we numerically analyze the ratio of $BR(\overline{B} \to D^{(*)}\tau\overline{\nu}_\tau)$ to $BR(\overline{B} \to D^{(*)}\ell\overline{\nu}_\ell)$, i.e., $R_{D^{(*)}}$. The introduced doublet and triplet LQs cannot efficiently enhance $R_{D^{(*)}}$, so in the following estimations, we only focus on the singlet LQ contributions, where the four-Fermi interactions shown in Eq. (30) come mainly from the scalar- and tensor-type interaction structures. Based

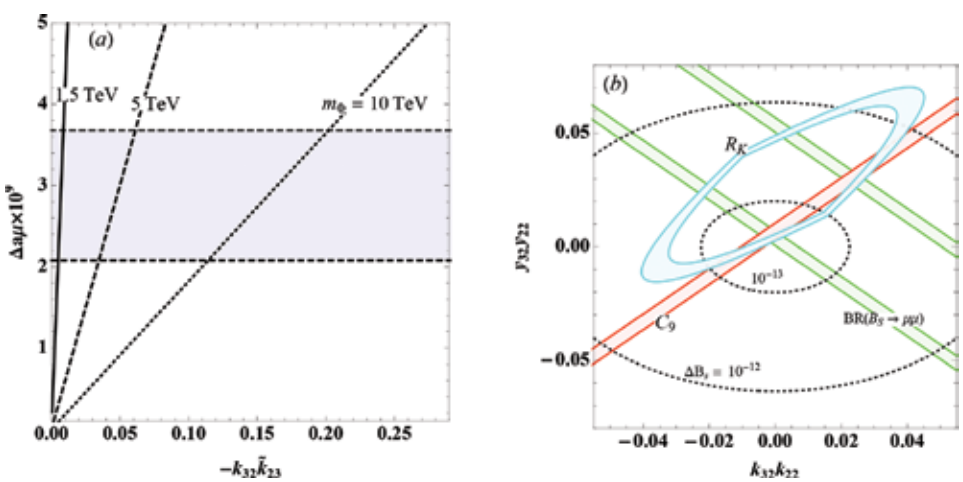


**Figure 2.**
*(a) $\Delta a_\mu$ as a function of $k_{32}\tilde{k}_{23}$ with $m_\Phi = 1.5, 5, 10$ TeV, where the band denotes the experimental data with $1\sigma$ errors. (b) Contours for $R_K$, $B_s \to \mu^+\mu^-$, $\Delta m_{B_s}$, and $C_9^{LQ,\mu}$ as a function of $k_{32}k_{22}$ and $y_{32}y_{22}$, where the ranges of $R_K$ and $B_s \to \mu^+\mu^-$ are the experimental values with $1\sigma$ errors and $m_{LQ} = 1.5$ TeV. For $C_9^{LQ,\mu}$, we show the range for $C^{LQ,\mu} = [-1.5, -0.5]$. (These plots are taken from Ref. [32]).*

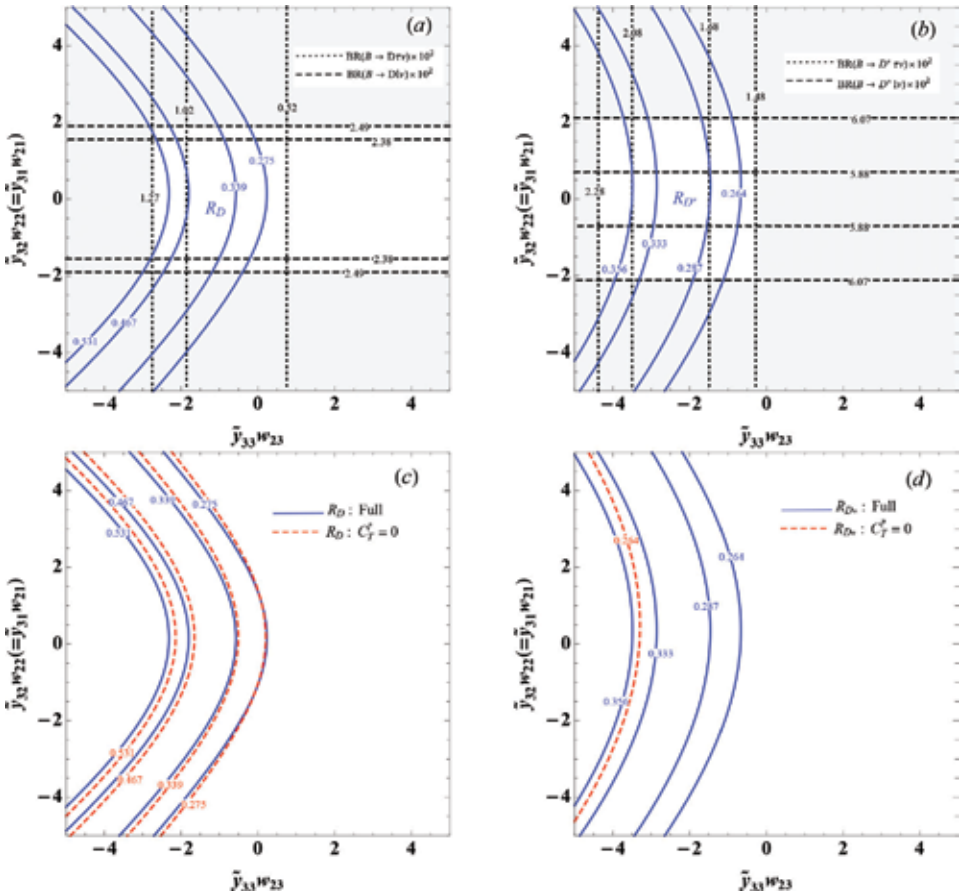


**Figure 3.**
*Contours for (a) $R_D$ and (b) $R_{D^*}$, where the solid lines denote the data with $1\sigma$ and $2\sigma$ errors, respectively. The horizontal dashed lines in both plots denote the $BR^{exp}(B^+ \to D^{(*)}\ell\nu_\ell)$, whereas the vertical dotted lines are the $BR^{exp}(B^+ \to D^{(*)}\tau\nu_\tau)$. Contours for (c) $R_D$ and (d) $R_{D^*}$, where the solid and dashed lines denote the situations with and without tensor operator contributions, respectively. In this case, we take $m_{LQ} = 1.5$ TeV. (These plots are taken from ref. [32]).*

on Eqs. (48), (50), and (51), we show the contours for $R_D$ and $R_{D^*}$ as a function of $\tilde{y}_{33}w_{23}$ and $\tilde{y}_{32}w_{22}(\tilde{y}_{31}w_{21})$ in **Figure 3(a)** and **(b)**, where the horizontal dashed and vertical dotted lines in both plots denote $BR^{exp}(B^- \to D[\ell\overline{\nu}_\ell, \tau\overline{\nu}_\tau]) = [2.27 \pm 0.11, 0.77 \pm 0.25]\%$ and $BR^{exp}(B^- \to D^*[\ell\nu_\ell, \tau\overline{\nu}_\tau]) = [5.69 \pm 0.19, 1.88 \pm 0.20]\%$, respectively, and $m_{LQ} = 1.5$ TeV is used, and the data with $2\sigma$ errors are taken. For simplicity, we take $\tilde{y}_{31}w_{21} \approx \tilde{y}_{32}w_{22}$. When considering the limits from $BR(\overline{B} \to D^{(*)}\ell'\overline{\nu}_{\ell'})$, we obtain the limits $|\tilde{y}_{3\ell}w_{2\ell}| \leq 1.5$ and $\tilde{y}_{33}w_{23} > 0$. In order to clearly demonstrate the influence of tensor-type interactions, we also calculate the situation by setting $C_T^{\ell'} = 0$. The contours obtained for $R_D$ and $R_{D^*}$ are shown in **Figure 3(c)** and **(d)**, where the solid and dashed lines denote the cases with and without $C_T^{\ell'}$, respectively. According to these plots, we can see that $R_D$ and $R_{D^*}$ have different responses to the tensor operators, where the latter is more sensitive to the tensor interactions. $R_D$ and $R_{D^*}$ can be explained simultaneously with the tensor couplings. In order to understand the correlation between $BR(B_c \to \tau\overline{\nu}_\tau)$ and $R_{D^{(*)}}$, we show the contours for $BR(B_c \to \tau\overline{\nu}_\tau)$ and $R_{D^{(*)}}$ as a function of $w_{23}\tilde{y}_{33}$ and $m_S$ in **Figure 4**, where $\tilde{y}_{32}w_{22} \approx \tilde{y}_{31}w_{21} \approx 0$ are used, and the gray area is excluded by

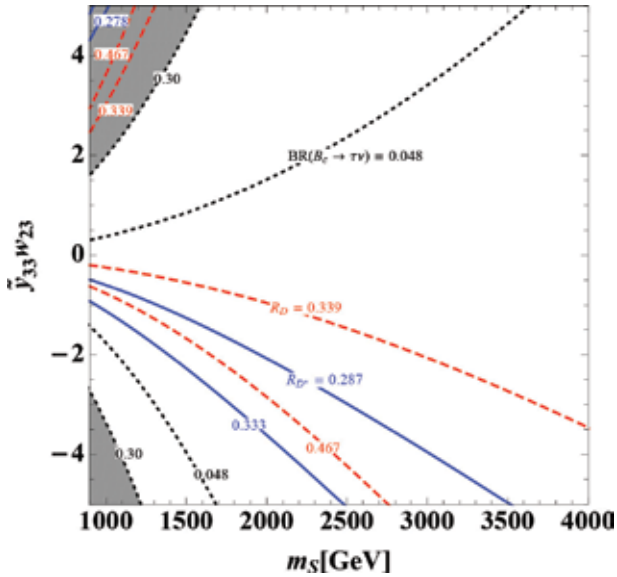


**Figure 4.**
*Contours for $BR(B_c \to \tau\overline{\nu}_\tau)$ and $R_{D^{(*)}}$ as a function of $w_{23}\tilde{y}_{23}$ and $m_S$. (The plot is taken from ref. [32]).*

$BR\left(B_c^- \to \tau\nu\right) < 0.3$. We can see that the predicted $BR(B_c \to \tau\overline{\nu}_\tau)$ is much smaller than the experimental bound.

Finally, we make some remarks regarding the constraint due to the LQ search at the LHC. Due to the flavor physics constraints, only the $S^{1/3}$ Yukawa couplings $\tilde{y}_{t\tau}$, $\tilde{y}_{b\nu_\tau}$, and $w_{c\tau}$ can be of $O(1)$. These couplings affect the $S^{1/3}$ decays but also their production. Therefore, in addition to the $S^{1/3}$-pair production, based on the $O(1)$ Yukawa couplings, the single $S^{1/3}$ production becomes interesting. In the $pp$ collisions, the single $S^{1/3}$ production can be generated via the $gb \to S^{-1/3}\overline{\nu}_\tau$ and $gc \to S^{-1/3}\tau^+$ channels. Using CalcHEP 3.6 [51, 52] with the CTEQ6 parton distribution functions [53], their production cross sections with $|w_{23}| \sim |\tilde{y}_{b\nu_\tau}| \sim \sqrt{2}$ and $m_{LQ} = 1000$ GeV at $\sqrt{s} = 13$ TeV can be obtained as 3.9 fb and 2.9 fb, respectively, whereas the $S^{1/3}$-pair production cross section is $\sigma\left(pp \to S^{-1/3}S^{1/3}\right) \approx 2.4$ fb. If we assume that $S^{-1/3}$ predominantly decays into $t\tau$, $b\nu_\tau$, and $c\tau$ with similar BRs, i.e. $BR\left(S^{-1/3} \to f\right) \sim 1/3$, then the single $S^{1/3}$ production cross section $\sigma\left(S^{-1/3}X\right)$ times $BR\left(S^{-1/3} \to f\right)$ with $X$ and $f$ as the possible final states can be estimated as around 1 fb. The LQ coupling $w_{23}$ involves different generations, so the constraints due to the collider measurements may not be applied directly. However, if we compare this with the CMS experiment [54] based on a single production of the second-generation scalar LQ, we find that the values of $\sigma \times BR$ at $m_{LQ} \sim 1000$ GeV are still lower than the CMS upper limit with few fb. The significance of this discovery depends on the kinematic cuts and event selection conditions, but this discussion is beyond the scope of this study, and we leave the detailed analysis for future research.

## 4. Conclusions

We have reviewed some charged particles which appear from physics beyond the Standard Model of particle physics. Some possible candidates of them are listed

such as charged scalar boson, vector-like leptons, vector-like quarks, and leptoquarks. After showing some properties and interactions of these particles, we reviewed some applications to flavor physics in which lepton flavor physics with vector-like lepton and $B$-meson physics with leptoquarks are focused on as an illumination. We have seen rich phenomenology that would be induced from such new charged particles, and they will be also tested in the future experiments.

## Author details

Takaaki Nomura
School of Physics, Korea Institute for Advanced Study, Seoul, Republic of Korea

*Address all correspondence to: nomura@kias.re.kr

## References


[1] Bennett GW et al. [Muon g-2 Collaboration]. Final report of the muon E821 anomalous magnetic moment measurement at BNL. Physical Review D. 2006;**73**:072003. DOI: 10.1103/PhysRevD.73.072003. [hep-ex/0602035]

[2] Patrignani C et al. [Particle Data Group]. Review of particle physics. Chinese Physics C. 2016;**40**(10): 100001. DOI: 10.1088/1674-1137/40/10/100001

[3] Davier M, Hoecker A, Malaescu B, Zhang Z. Reevaluation of the hadronic contributions to the muon g-2 and to alpha (MZ). European Physical Journal C: Particles and Fields. 2011;**71**:1515. DOI: 10.1140/epjc/s10052-010-1515-z; Erratum: European Physical Journal C: Particles and Fields. 2012;**72**:1874. DOI: 10.1140/epjc/s10052-012-1874-8. [arXiv:1010.4180 [hep-ph]]

[4] Jegerlehner F, Szafron R. $\rho^0 - \gamma$ mixing in the neutral channel pion form factor $F_\pi^e$ and its role in comparing $e^+e^-$ with $\tau$ spectral functions. European Physical Journal C: Particles and Fields. 2011;**71**:1632. DOI: 10.1140/epjc/s10052-011-1632-3. [arXiv:1101.2872 [hep-ph]]

[5] Hagiwara K, Liao R, Martin AD, Nomura D, Teubner T. (g-2)$\mu$ and alpha (M_Z$^2$) re-evaluated using new precise data. Journal of Physics G. 2011;**38**: 085003. DOI: 10.1088/0954-3899/38/8/085003. [arXiv:1105.3149 [hep-ph]]

[6] Aoyama T, Hayakawa M, Kinoshita T, Nio M. Complete tenth-order QED contribution to the muon g-2. Physical Review Letters. 2012;**109**:111808. DOI: 10.1103/PhysRevLett.109.111808. [arXiv:1205.5370 [hep-ph]]

[7] Descotes-Genon S, Matias J, Ramon M, Virto J. Implications from clean observables for the binned analysis of $B - > K*\mu^+\mu^-$ at large recoil. JHEP. 2013;**1301**:048. DOI: 10.1007/JHEP01(2013)048. [arXiv:1207.2753 [hep-ph]]

[8] Aaij R et al. [LHCb Collaboration]. Angular analysis of the $B^0 \to K^{*0}\mu^+\mu^-$ decay using 3 fb$^{-1}$ of integrated luminosity. JHEP. 2016;**1602**:104. DOI: 10.1007/JHEP02(2016)104. [arXiv:1512.04442 [hep-ex]]

[9] Aaij R et al. [LHCb Collaboration]. Measurement of form-factor-independent observables in the decay $B^0 \to K^{*0}\mu^+\mu^-$. Physical Review Letters. 2013;**111**:191801. DOI: 10.1103/PhysRevLett.111.191801. [arXiv:1308.1707 [hep-ex]]

[10] Wehle S et al. [Belle Collaboration]. Lepton-Flavor-Dependent Angular Analysis of $B \to K^*\ell^+\ell^-$. Physical Review Letters. 2017;**118**(11):111801. DOI: 10.1103/PhysRevLett.118.111801 [arXiv:1612.05014 [hep-ex]]

[11] Huschle M et al. [Belle Collaboration]. Measurement of the branching ratio of $\overline{B} \to D^{(*)}\tau^-\overline{\nu}_\tau$ relative to $\overline{B} \to D^{(*)}\ell^-\overline{\nu}_\ell$ decays with hadronic tagging at Belle. Physical Review D. 2015;**92**(7):072014. DOI: 10.1103/PhysRevD.92.072014. [arXiv:1507.03233 [hep-ex]]

[12] Lees JP et al. [BaBar Collaboration]. Evidence for an excess of $\overline{B} \to D^{(*)}\tau^-\overline{\nu}_\tau$ decays. Physical Review Letters. 2012; **109**:101802. DOI: 10.1103/PhysRevLett.109.101802. [arXiv:1205.5442 [hep-ex]]

[13] Lees JP et al. [BaBar Collaboration]. Measurement of an excess of $\overline{B} \to D^{(*)}\tau^-\overline{\nu}_\tau$ decays and implications for charged Higgs bosons. Physical Review D. 2013;**88**(7):072012. DOI: 10.1103/PhysRevD.88.072012. [arXiv:1303.0571 [hep-ex]]

[14] Abdesselam A et al. [Belle Collaboration]. Measurement of the branching ratio of $\overline{B}^0 \to D^{*+}\tau^-\overline{\nu}_\tau$ relative to $\overline{B}^0 \to D^{*+}\ell^-\overline{\nu}_\ell$ decays with a semileptonic tagging method. arXiv: 1603.06711 [hep-ex]

[15] Hirose S et al. [Belle Collaboration]. Measurement of the $\tau$ lepton polarization and $R(D^*)$ in the decay $\overline{B} \to D^*\tau^-\overline{\nu}_\tau$. Physical Review Letters. 2017;**118**(21):211801. DOI: 10.1103/PhysRevLett.118.211801. [arXiv: 1612.00529 [hep-ex]]

[16] Aaij R et al. [LHCb Collaboration]. Measurement of the ratio of branching fractions $\mathcal{B}\left(\overline{B}^0 \to D^{*+}\tau^-\overline{\nu}_\tau\right)/\mathcal{B}\left(\overline{B}^0 \to D^{*+}\mu^-\overline{\nu}_\mu\right)$. Physical Review Letters. 2015;**115**(11):111803. DOI: 10.1103/PhysRevLett.115.111803; Addendum: Physical Review Letters. 2015;**115**(15):159901. DOI: 10.1103/PhysRevLett.115.159901. [arXiv: 1506.08614 [hep-ex]]

[17] Gunion JF, Haber HE, Kane GL, Dawson S. The Higgs hunter's guide front. Physiologie. 2000;**80**:1

[18] Branco GC, Ferreira PM, Lavoura L, Rebelo MN, Sher M, Silva JP. Theory and phenomenology of two-Higgs-doublet models. Physics Reports. 2012; **516**:1. DOI: 10.1016/j.physrep.2012.02.002. [arXiv:1106.0034 [hep-ph]]

[19] Magg M, Wetterich C. Neutrino mass problem and gauge hierarchy. Physics Letters B. 1980;**94**:61

[20] Lazarides G, Shafi Q, Wetterich C. Proton lifetime and fermion masses in an SO(10) model. Nuclear Physics B. 1981;**181**:287

[21] Mohapatra RN, Senjanovic G. Neutrino masses and mixings in gauge models with spontaneous parity violation. Physical Review D. 1981;**23**:165

[22] Ma E, Sarkar U. Neutrino masses and leptogenesis with heavy Higgs triplets. Physical Review Letters. 1998; **80**:5716. [hep-ph/9802445]

[23] Konetschny W, Kummer W. Nonconservation of total lepton number with scalar bosons. Physics Letters B. 1977;**70**:433

[24] Schechter J, Valle JWF. Neutrino masses in SU(2) $\times$ U(1) theories. Physical Review D. 1980;**22**:2227

[25] Cheng TP, Li L-F. Neutrino masses, mixings and oscillations in SU(2) $\times$ U(1) models of electroweak interactions. Physical Review D. 1980; **22**:2860

[26] Bilenky SM, Hosek J, Petcov ST. On oscillations of neutrinos with dirac and majorana masses. Physics Letters B. 1980;**94**:495

[27] Zee A. Quantum numbers of majorana neutrino masses. Nuclear Physics B. 1986;**264**:99

[28] Babu KS. Model of 'Calculable' majorana neutrino masses. Physics Letters B. 1988;**203**:132

[29] Chen CH, Nomura T. Bounds on LFV Higgs decays in a vector-like lepton model and searching for doubly charged leptons at the LHC. European Physical Journal C: Particles and Fields. 2016;**76** (6):353. DOI: 10.1140/epjc/s10052-016-4197-3. [arXiv:1602.07519 [hep-ph]]

[30] Chen CH, Nomura T. Single production of $X_{\pm 5/3}$ and $Y_{\mp 4/3}$ vector like quarks at the LHC. Physical Review D. 2016;**94**(3):035001. DOI: 10.1103/PhysRevD.94.035001. [arXiv: 1603.05837 [hep-ph]]

[31] Chen CH, Nomura T, Okada H. Explanation of $B \to K^{(*)}\ell^+\ell^-$ and muon $g-2$, and implications at the LHC. Physical Review D. 2016;**94**(11):115005.

DOI: 10.1103/PhysRevD.94.115005. [arXiv:1607.04857 [hep-ph]]

[32] Chen CH, Nomura T, Okada H. Excesses of muon $g-2$, $R_{D^{(*)}}$, and $R_K$ in a leptoquark model. Physics Letters B. 2017;**774**:456. DOI: 10.1016/j.physletb.2017.10.005. [arXiv:1703.03251 [hep-ph]]

[33] Aad G et al. [ATLAS Collaboration]. Measurements of the Higgs boson production and decay rates and coupling strengths using pp collision data at $\sqrt{s}=7$ and 8 TeV in the ATLAS experiment. European Physical Journal C: Particles and Fields. 2016;**76**(1):6. DOI: 10.1140/epjc/s10052-015-3769-y. [arXiv:1507.04548 [hep-ex]]

[34] CMS Collaboration [CMS Collaboration]. Precise determination of the mass of the Higgs boson and studies of the compatibility of its couplings with the standard model. CMS-PAS-HIG-14-009

[35] Amhis Y et al. [HFLAV Collaboration]. Averages of $b$-hadron, $c$-hadron, and $\tau$-lepton properties as of summer 2016. European Physical Journal C. 2017;**77**(12):895. DOI: 10.1140/epjc/s10052-017-5058-4 [arXiv: 1612.07233 [hep-ex]]

[36] Bailey JA et al. [MILC Collaboration]. '$B \to D\tau\nu$ form factors at nonzero recoil and $|V_{cb}|$ from 2+1-flavor lattice QCD. Physical Review D. 2015;**92**(3):034506. DOI: 10.1103/PhysRevD.92.034506. [arXiv: 1503.07237 [hep-lat]]

[37] Na H et al. [HPQCD Collaboration]. $B \to Dl\nu$ form factors at nonzero recoil and extraction of $|V_{cb}|$. Physical Review D. 2015;**92**(5):054510. DOI: 10.1103/PhysRevD.93.119906; Erratum: Physical Review D. 2016;**93**(11):119906. DOI: 10.1103/PhysRevD.92.054510 [arXiv: 1505.03925 [hep-lat]]

[38] Aaij R et al. [LHCb Collaboration]. Test of lepton universality using $B^+ \to K^+\ell^+\ell^-$ decays. Physical Review Letters. 113, 151601 (2014) DOI: 10.1103/PhysRevLett.113.151601. [arXiv:1406.6482 [hep-ex]]

[39] Aaij R et al. [LHCb Collaboration]. Test of lepton universality with $B^0 \to K^{*0}\ell^+\ell^-$ decays. JHEP. 2017; **1708**:055. DOI: 10.1007/JHEP08(2017) 055 [arXiv:1705.05802 [hep-ex]]

[40] Dowdall RJ et al. [HPQCD Collaboration]. B-Meson decay constants from improved lattice nonrelativistic QCD with physical u, d, s, and c quarks. Physical Review Letters. 2013;**110**(22):222003. DOI: 10.1103/PhysRevLett.110.222003. [arXiv: 1302.2644 [hep-lat]]

[41] Buchalla G, Buras AJ, Lautenbacher ME. Weak decays beyond leading logarithms. Reviews of Modern Physics. 1996;**68**:1125. DOI: 10.1103/RevModPhys.68.1125. [hep-ph/9512380]

[42] Aaij R et al. [LHCb Collaboration]. Measurement of the $B_s^0 \to \mu^+\mu^-$ branching fraction and effective lifetime and search for $B^0 \to \mu^+\mu^-$ decays. Physical Review Letters. 2017;**118**(19): 191801. DOI: 10.1103/PhysRevLett.118.191801. [arXiv: 1703.05747 [hep-ex]]

[43] Bobeth C, Gorbahn M, Hermann T, Misiak M, Stamou E, Steinhauser M. $B_{s,d} \to l^+l^-$ in the standard model with reduced theoretical uncertainty. Physical Review Letters. 2014;**112**: 101801. DOI:10.1103/PhysRevLett.112.101801 [arXiv: 1311.0903 [hep-ph]]

[44] Hiller G, Schmaltz M. $R_K$ and future $b \to s\ell\ell$ physics beyond the standard model opportunities. Physical Review D. 2014;**90**:054014. DOI: 10.1103/

PhysRevD.90.054014. [arXiv:1408.1627 [hep-ph]]

[45] Alonso R, Grinstein B, Martin Camalich J. Lifetime of $B_c^-$ Constrains explanations for anomalies in $B \to D^{(*)}\tau\nu$. Physical Review Letters. 2017;**118**(8):081802. DOI: 10.1103/PhysRevLett.118.081802. [arXiv:1611.06676 [hep-ph]]

[46] Colquhoun B et al. [HPQCD Collaboration]. B-meson decay constants: A more complete picture from full lattice QCD. Physical Review D. 2015;**91**(11):114509. DOI: 10.1103/PhysRevD.91.114509. [arXiv:1503.05762 [hep-lat]]

[47] Melikhov D, Stech B. Weak form-factors for heavy meson decays: An Update. Physical Review D. 2000;**62**: 014006. DOI: 10.1103/PhysRevD.62.014006. [hep-ph/0001113]

[48] Wang YM, Wei YB, Shen YL, Lü CD. Perturbative corrections to B → D form factors in QCD. JHEP. 2017;**1706**: 062. DOI: 10.1007/JHEP06(2017)062. [arXiv:1701.06810 [hep-ph]]

[49] Sakaki Y, Tanaka M, Tayduganov A, Watanabe R. Testing leptoquark models in $\overline{B} \to D^{(*)}\tau\overline{\nu}$. Physical Review D. 2013; **88**(9):094012. DOI: 10.1103/PhysRevD.88.094012. [arXiv:1309.0301 [hep-ph]]

[50] Chen CH, Geng CQ. Probing new physics in B —> K(*) l+ l− decays. Physical Review D. 2002;**66**:094018. DOI: 10.1103/PhysRevD.66.094018. [hep-ph/0209352]

[51] Belyaev A, Christensen ND, Pukhov A. CalcHEP 3.4 for collider physics within and beyond the Standard Model. Computer Physics Communications. 2013;**184**:1729. [arXiv:1207.6082 [hep-ph]]

[52] Belyaev A, Leroy C, Mehdiyev R, Pukhov A. Leptoquark single and pair production at LHC with CalcHEP/CompHEP in the complete model. JHEP. 2005;**0509**:005. DOI: 10.1088/1126-6708/2005/09/005. [hep-ph/0502067]

[53] Nadolsky PM, Lai HL, Cao QH, Huston J, Pumplin J, Stump D, et al. Implications of CTEQ global analysis for collider observables. Physical Review D. 2008;**78**:013004. [arXiv:0802.0007 [hep-ph]]

[54] Khachatryan V et al. [CMS Collaboration]. Search for single production of scalar leptoquarks in proton-proton collisions at $\sqrt{s} = 8\ TeV$. Physical Review D. 2016;**93**(3):032005. DOI: 10.1103/PhysRevD.93.032005; Erratum: Physical Review D. 2017;**95** (3):039906. DOI: 10.1103/PhysRevD.95.039906. [arXiv:1509.03750 [hep-ex]]

Section 3

# Electron Positron Plasma

Chapter 5

# Electrostatic Waves in Magnetized Electron-Positron Plasmas

*Ian Joseph Lazarus*

## Abstract

The behavior of arbitrary amplitude linear and nonlinear electrostatic waves that propagate in a magnetized four component, two-temperature, electron-positron plasma is presented. The characteristics of the dispersive properties of the associated linear modes using both fluid and kinetic theory are examined. The fluid theory analysis of the electrostatic linear waves shows the existence of electron acoustic, upper hybrid, electron plasma and electron cyclotron branches. A kinetic theory analysis is then used to study the acoustic mode, in particular the effect of Landau damping, which for the parameter regime considered is due to the cooler species. Consequently, it is found that a large enough drift velocity is required to produce wave growth. Nonlinear electrostatic solitary waves (ESWs), similar to those found in the broadband electrostatic noise observed in various regions of the earth's magnetosphere is further investigated. A set of nonlinear differential equations for the ESWs, which propagate obliquely to an external magnetic field is derived and numerically solved. The effect of various plasma parameters on the waves is explored and shows that as the electric driving force is increased, the electric field structure evolves from a sinusoidal wave to a spiky bipolar form. The results are relevant to both astrophysical environments and related laser-induced laboratory experiments.

**Keywords:** electrons, positrons, electrostatic waves, nonlinear waves

## 1. Introduction

Electron-positron plasmas play a significant role in the understanding of the early universe [1, 2], active galactic nuclei [3], gamma ray bursts (GRBs) [4], pulsar magnetospheres [5, 6] and the solar atmosphere [7]. These plasmas are also important in understanding extremely dense stars such as white dwarfs and pulsars, which are thought to be rotating neutron stars. The existence of these plasmas in neutron stars and in the pulsar magnetosphere is well documented [8]. The possibility for the co-existence of two types of cold and hot electron-positron populations in the pulsar magnetosphere has been suggested by [9] which was inspired by the pulsar model [10]. In their model, accelerated primary electrons moving on curved magnetic field lines emit curvature photons which produce electron-positron pairs. The secondary particles then produce curvature radiation, hence producing new electron-positron pairs, and so on. Therefore, both the electron and positron populations can be subdivided in two groups of distinct temperatures, one modeling the original plasma, and the second the higher-energy cascade-bred pairs. It is also

known that in astrophysical and cosmic plasmas, a minority of cold electrons and heavy ions exist along with hot electron-positron pairs [11]. Hence, the formation of two temperature multispecies plasmas is possible due to the outflow of the electron-positron plasma from pulsars entering into an interstellar cold, low-density electron-ion plasma [12].

Investigations into electron-positron plasma behavior have focused primarily on the relativistic regime. It is however plausible that nonrelativistic astrophysical electron-positron plasmas may exist, given the effect of cooling by cyclotron emission [13]. The study of nonrelativistic astrophysical electron-positron plasmas therefore plays an important role in understanding wave fluctuations. Due to the equal charge to mass ratio for these oppositely charged species, only one frequency scale exists and due to this symmetry, there exists different physical phenomena to the conventional electron-ion plasmas. Further, the frequent instabilities that arise in space plasma and astrophysical environments (e.g., solar flames and auroras), involve the growth of electrostatic and electromagnetic waves which gives rise to a growing wave mode. In particular, the linear behavior of the electrostatic modes using fluid and kinetic theory approaches allows one to understand the effect of plasma parameters such as the propagation angle, cool to hot temperature ratios, density ratios and the magnetic field strength on the waves.

Investigations conducted have focused on modulational instabilities and wave localization [14], envelope solitons [15], multidimensional effects [16]. Large amplitude solitons and electrostatic nonlinear potential structures in electron-positron plasmas having equal hot and cold components of both species have been studied by a number of authors [17–19]. In one such study [20], using the two-fluid model with a single temperature they investigated linear and nonlinear longitudinal and transverse electrostatic and electromagnetic waves in a nonrelativistic electron-positron plasma in the absence and presence of an external magnetic field. They found that several of the modes present in electron-ion plasmas also existed in electron-positron plasmas, but in a modified form. Collective modes in nonrelativistic electron-positron plasmas using the kinetic approach was studied by [21]. The author found that the dispersion relations for the longitudinal modes in the electron-positron plasma for both unmagnetized and magnetized electron-positron plasmas were similar to the modes in one-component electron or electron-ion plasmas. Moreover, the hybrid resonances present in the former are not found in an electron-positron plasma.

The understanding of nonlinear wave structures which gives rise to electrostatic solitary wave (ESWs) in space is important since it is known that satellite measurements using high-time resolution equipment aboard spacecraft S3-3 [22], Viking [23], Geotail [24], Polar [25], and Fast [26] have indicated the presence of Broadband Electrostatic Noise (BEN) in the auroral magnetosphere at altitudes between 3000 km to 8000 km and beyond. These observations have shown the presence of electrostatic solitary waves (ESWs), which are characterized by their spiky bipolar pulses. Hence, the study of nonlinear wave behavior in electron-positron plasmas propagating at oblique angles to an ambient magnetic field is explored to understand electrostatic solitary waves in space. Specifically, the spiky nature of the electrostatic potential structures and the effects of the propagation angle, cold and hot drift velocities, cool to hot density and temperature ratios and Mach number on the ESWs are examined.

In this chapter a two-temperature magnetized four component electron-positron plasma model is used to study linear wave modes using both the fluid and kinetic approaches as well as the behavior of the nonlinear structures of these electrostatic solitary waves (ESWs) which plays an important role in space and astrophysical environments.

## 2. Linear waves in electron-positron plasmas: fluid theory approach

Let us consider a homogeneous magnetized, four component electron-positron plasma, consisting of cool electrons and cool positrons with equal temperatures and equilibrium densities denoted by $T_c$ and $n_{0c}$, respectively, and hot electrons and hot positrons with equal temperatures and equilibrium densities denoted by $T_h$ and $n_{0h}$, respectively. The temperatures are expressed in energy units and wave propagation is taken in the $x$-direction at an angle $\theta$ to the ambient magnetic field $\mathbf{B_0}$, which is assumed to be in the $x$–$z$ plane.

Assuming that the hot isothermal species are described by the Boltzmann distribution, their densities are, respectively

$$n_{eh} = n_{0h} \exp\left(\frac{e\phi}{T_h}\right) \tag{1}$$

and

$$n_{ph} = n_{0h} \exp\left(\frac{-e\phi}{T_h}\right), \tag{2}$$

where $n_{eh}$ ($n_{ph}$) is the density of the hot electrons (positrons) and $\phi$ is the electrostatic potential.

Using Boltzmann distribution of hot electrons and positrons is justified provided they have sufficiently high temperatures, much greater than that of cooler species such that their thermal velocities parallel to the magnetic field exceed the phase velocity of the modes so that they are able to establish the Boltzmann distribution. The magnetic field effects on hot species are not felt since the perturbation wavelengths are shorter than their gyroradii such that both hot electrons and positrons follow essentially straight line orbits across the magnetic field direction.

The dynamics of cooler isothermal species are governed by fluid equations, namely the continuity equations,

$$\frac{\partial n_{jc}}{\partial t} + \nabla.\left(n_{jc}\mathbf{v}_{jc}\right) = 0, \tag{3}$$

the equations of motion,

$$\frac{\partial \mathbf{v}_{jc}}{\partial t} + \mathbf{v}_{jc}.\nabla\mathbf{v}_{jc} = -\varepsilon_j \frac{e}{m}\nabla\phi + \varepsilon_j \frac{e}{m}\left(\mathbf{v}_{jc} \times B_0\right) - \frac{\gamma T_c}{n_{jc}m}\nabla n_{jc}, \tag{4}$$

where $\varepsilon_j = +1(-1)$ for positrons (electrons), $j = e(p)$ for the electrons (positrons). The system is closed by the Poisson equation

$$\varepsilon_0 \frac{\partial^2 \phi}{\partial x^2} = -e\left(n_{pc} - n_{ec} + n_{ph} - n_{eh}\right). \tag{5}$$

In the above equations, $n_j$ and $v_j$ are the number densities and fluid velocities respectively of the *jth* species. In order to derive the linear dispersion relation, equations (3)–(5) are linearized. For perturbations varying as $\exp\left(i(kx - \omega t)\right)$, $\partial/\partial t$ is replaced with $-i\omega$ and $\partial/\partial x$ with $ik$. Hence the perturbed densities for the electrons and positrons become

$$n_{ec} = -\left(\frac{n_{0c}ek^2\phi}{m}\right)\left(\frac{\omega^2 - \Omega^2\cos^2\theta}{\omega^4 - \omega^2\left(3k^2v_{tc}^2 + \Omega^2\right) + 3k^2v_{tc}^2\Omega^2\cos^2\theta}\right). \tag{6}$$

and

$$n_{pc} = \left(\frac{n_{0c}ek^2\phi}{m}\right)\left(\frac{\omega^2 - \Omega^2\cos^2\theta}{\omega^4 - \omega^2\left(3k^2v_{tc}^2 + \Omega^2\right) + 3k^2v_{tc}^2\Omega^2\cos^2\theta}\right). \tag{7}$$

From equations (1) and (2), the perturbed densities for the hot species are given by,

$$n_{eh} = n_{oh}\frac{e\phi}{T_h} \tag{8}$$

and

$$n_{ph} = -n_{oh}\frac{e\phi}{T_h}. \tag{9}$$

Substituting equations (6)–(9), into Poisson's equation (5), the general dispersion relation for the two temperature electron-positron plasma is found to be

$$\omega^2\left(\omega^2 - \Omega^2\right) - 3k^2v_{tc}^2\left(\omega^2 - \Omega^2\cos^2\theta\right) - \frac{k^2\,v_{ea}^2}{1 + \frac{1}{2}k^2\lambda_{Dh}^2}\left(\omega^2 - \Omega^2\cos^2\theta\right) = 0 \tag{10}$$

where $v_{ea} = (n_{0c}/n_{0h})^{1/2}v_{th}$ is the acoustic speed of the electron-positron plasma, analogous in form to the electron acoustic speed in an electron-ion plasma [27]. The thermal velocity of the cool species is $v_{tc} = (T_c/m)^{1/2}$, $\Omega_j = \Omega = q_jB_o/m$ is the gyrofrequency of the electrons and positrons and $\lambda_{dh} = (\varepsilon_0T_h/n_{0h}e^2)^{1/2}$ is the Debye length of the hot species.

It is noted that the study of linear electrostatic waves using a simple fluid model cannot handle the possible Landau damping of the modes. Hence, Landau damping is not significant since phase velocities are far away from the thermal velocities of either the hot or cooler species, i.e., $v_{th} \gg v_\phi \gg v_{tc}$ with $T_h \gg T_c$. The effects of the temperature variation on the acoustic mode in terms of Landau damping using kinetic theory are discussed in the next section.

For a single species electron-positron plasma, with temperature $T_c$, equation (10) reduces to,

$$\omega^4 - \omega^2\left(\Omega^2 + 3k^2v_{tc}^2\right) + 3k^2v_{tc}^2\Omega^2\cos^2\theta = 0. \tag{11}$$

This is identical to the dispersion relation of [20] for their single temperature electron-positron model.

For wave frequencies much lower than the gyrofrequency and satisfying $\omega \ll \Omega\cos\theta$, the associated electron-acoustic (or positron-acoustic) mode is found to be,

$$\omega^2 = \frac{k^2v_{ea}^2\cos^2\theta}{1 + \frac{1}{2}k^2\lambda_{Dh}^2} + 3k^2v_{tc}^2\cos^2\theta. \tag{12}$$

Taking short wavelength limit ($k^2\lambda_{Dh}^2 \gg 1$), the dispersion relation equation (10) reduces to,

$$\omega^4 - \omega^2\left(3k^2v_{tc}^2 + \omega_{UH}^2\right) + \left(3k^2v_{tc}^2 + 2\omega_{pc}^2\right)\Omega^2\cos^2\theta = 0, \tag{13}$$

where

$$\omega_{UH}^2 = \Omega^2 + 2\omega_{pc}^2 \tag{14}$$

is the upper hybrid frequency associated with the cooler species [20], with $\omega_{pc} = \left(n_{oc}e^2/\varepsilon_0 m\right)^{1/2}$ as the plasma frequency of the cooler species. If one solves equation (13) in the limit $\left(3k^2v_{tc}^2 + \omega_{UH}^2\right)^2 \gg 4\left(3k^2v_{tc}^2\Omega^2\cos^2\theta + 2\omega_{pc}^2\Omega^2\cos^2\theta\right)$, one obtains for the upper hybrid mode,

$$\omega_+^2 = \left(3k^2v_{tc}^2 + \omega_{UH}^2\right) - \frac{\left(3k^2v_{tc}^2 + 2\omega_{pc}^2\right)\Omega^2\cos^2\theta}{3k^2v_{tc}^2 + \omega_{UH}^2}, \tag{15}$$

Taking the negative square root of equation (13) yields

$$\omega_-^2 = \frac{\left(3k^2v_{tc}^2 + 2\omega_{pc}^2\right)\Omega^2\cos^2\theta}{3k^2v_{tc}^2 + \omega_{UH}^2}, \tag{16}$$

In order to gain physical insight into the solution space of the dispersion relation, the two extreme limits of equation (10) will now be considered, viz. pure perpendicular and pure parallel propagations.

### 2.1 Case I: pure perpendicular propagation

Considering the pure perpendicular ($\theta = 90^o$) limit, the general dispersion relation (10), reduces to:

$$\omega^4 - \omega^2\left(\Omega^2 + 3k^2v_{tc}^2 + \frac{k^2v_{ea}^2}{1 + \frac{1}{2}k^2\lambda_{dh}^2}\right) = 0. \tag{17}$$

Hence the normal mode frequencies are, $\omega = 0$, which is a nonpropagating mode, and

$$\omega^2 = \Omega^2 + 3k^2v_{tc}^2 + \frac{k^2v_{ea}^2}{1 + \frac{1}{2}k^2\lambda_{dh}^2}. \tag{18}$$

Taking the short wavelength limit ($k^2\lambda_{dh}^2 \gg 1$) of the above relationship, one obtains,

$$\omega^2 = \omega_{UH}^2 + 3k^2v_{tc}^2. \tag{19}$$

showing that the behavior of the upper hybrid mode for the two temperature model is due to the cooler species, where $\omega_{UH}^2 = \Omega_p^2 + 2\omega_{pc}^2$.

Now taking the long wavelength limit ($k^2\lambda_{dh}^2 \ll 1$) of the dispersion relation for perpendicular propagation, equation (18) reduces to

$$\omega^2 = \Omega^2 + k^2\left(3v_{tc}^2 + v_{ea}^2\right). \tag{20}$$

This is the cyclotron mode for the electron-positron plasma with contributions from both the thermal motion of the adiabatic cooler species and the acoustic motion due to the two species of different temperatures. To try and understand the physical implications, the above expression for the dispersion relation can be written as,

$$\omega^2 = \Omega^2 + k^2 v_{ea}^2\left(1 + 3\frac{T_c}{T_h}\frac{n_{0h}}{n_{0c}}\right). \tag{21}$$

For $T_c/T_h \ll 1$, one requires $n_{0h} \gg n_{0c}$, i.e., a plasma dominated by the hot species, in order for the second term in brackets to affect the dispersive properties of the wave.

### 2.2 Case II: pure parallel propagation

Considering the limit of parallel propagation ($\theta = 0^o$), the general dispersion relation (10) reduces to,

$$\omega^4 - \omega^2\left(\Omega^2 + 3k^2v_{tc}^2 + \frac{k^2v_{ea}^2}{1+\frac{1}{2}k^2\lambda_{dh}^2}\right) + \Omega^2\left(3k^2v_{tc}^2 + \frac{k^2v_{ea}^2}{1+\frac{1}{2}k^2\lambda_{dh}^2}\right) = 0, \tag{22}$$

from which it can be shown

$$\omega^2 = \frac{1}{2}\left[\Omega^2 + 3k^2v_{tc}^2 + \frac{k^2v_{ea}^2}{1+\frac{1}{2}k^2\lambda_{dh}^2} \pm \left(\Omega^2 - 3k^2v_{tc}^2 - \frac{k^2v_{ea}^2}{1+\frac{1}{2}k^2\lambda_{dh}^2}\right)\right]. \tag{23}$$

There exist two possible solutions. Taking the positive sign of the relevant term in equation (23) as the first option yields,

$$\omega_+^2 = \Omega^2, \tag{24}$$

which is a constant frequency, nonpropagating cyclotron mode.

Now taking the negative sign of the term in equation (23) yields the normal mode frequency

$$\omega_-^2 = 3k^2v_{tc}^2 + \frac{k^2v_{ea}^2}{1+\frac{1}{2}k^2\lambda_{dh}^2}, \tag{25}$$

which may be written for $k^2\lambda_{dh}^2 \ll 1$ as

$$\omega_-^2 = k^2v_{ea}^2\left(1 + 3\frac{T_c}{T_h}\frac{n_{0h}}{n_{0c}}\right), \tag{26}$$

which is identified fundamentally, as the electron-acoustic mode, with a correction term to its phase velocity due to the thermal motion of the cooler species.

In the limit $k^2\lambda_{dh}^2 \gg 1$, one obtains

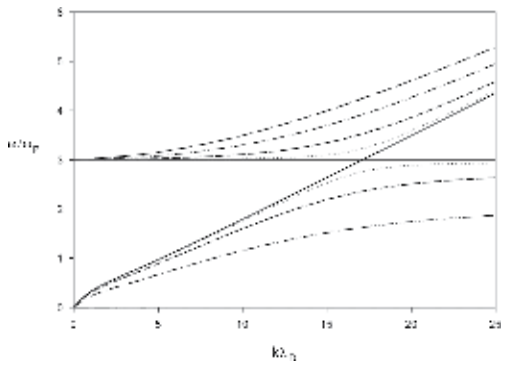

**Figure 1.**
*Normalized real frequency as a function of the normalized wavenumber showing the acoustic and cyclotron branches for various angles of propagation $\theta$ = 0° (solid), 9° (dotted), 22.5° (broken), 45° (dashddot) and 90° (longbroken). The fixed plasma parameters are $R = 0.333$, $T_c/T_h = 0.01$ and $n_{0c}/n_{0h} = 0.11$.*

$$\omega_-^2 = 3k^2 v_{tc}^2 + 2\omega_{pc}^2 \tag{27}$$

Equating equations (24) and (27) in the limit $k^2\lambda_{dh}^2 \gg 1$, the critical $k$ value for which the two modes may couple is determined to be,

$$(k\lambda_d)_{crit} = \left(\frac{T_h}{3T_c}\frac{n_{0c}}{n_0}\right)^{1/2}\left(\frac{n_0}{n_{0c}R^2} - 2\right)^{1/2}. \tag{28}$$

A numerical analysis of the general dispersion relation can be performed focusing on the effects of the density and temperature ratios of the hot and cool electrons and positrons. If one normalizes the fluid speeds by the thermal velocity $v_{th} = (T_h/m)^{1/2}$, the particle density by the total equilibrium plasma density $n_0 = n_{0c} + n_{0h}$, the temperatures by $T_h$, the spatial length by $\lambda_D = (\varepsilon_0 T_h/n_0 e^2)^{1/2}$, and the time by $\omega_p^{-1} = (n_0 e^2/\varepsilon_0 m)^{-1/2}$ in equation (10), you get the normalized general dispersion relation,

$$\omega'^4 - \omega'^2\left(\frac{1}{R^2} + 3k'^2\frac{T_c}{T_h} + \frac{k'^2 n'_{0c}}{n'_{0h} + \frac{1}{2}k'^2}\right) + \frac{\cos^2\theta}{R^2}\left(3k'^2\frac{T_c}{T_h} + \frac{k'^2 n'_{0c}}{n'_{0h} + \frac{1}{2}k'^2}\right) = 0, \tag{29}$$

where $\omega' = \omega/\omega_p$, $k' = k\lambda_D$, $n'_{0h} = n_{0h}/n_0$, $n'_{0c} = n_{0c}/n_0$ and $R = \omega_p/\Omega$ is a measure of the plasma densities and the strength of the magnetic field. A typical result can be seen in **Figure 1** [28] for the normalized real frequency as a function of the normalized wavenumber showing the acoustic and cyclotron branches for a range of propagation angles.

## 3. Linear waves in electron-positron plasmas: kinetic theory approach

In this section the kinetic theory approach is used to study the acoustic mode that was investigated in the previous section using fluid theory. The focus is on this mode since it is a micro-instability arising from resonances in velocity space. This instability is kinetic in nature and the growth rate of the wave is a function of the slope of the velocity distribution function. When the wave phase velocity along $\mathbf{B_0}$ sees a negative slope of the velocity distribution $(\partial f_0/\partial V_\parallel < 0)$, the particles on

average will gain energy from the wave, consequently the wave losses energy and becomes damped, an effect known as Landau damping. The wave mode is hence subjected to Landau damping and wave enhancement. Therefore the focus in this section is primarily on the effect of the temperatures of the plasma species.

The same plasma model as in the previous section is considered, i.e., a four component magnetized electron-positron plasma, consisting of cool electrons and cool positrons with equal temperatures and equilibrium densities denoted by $T_c$ and $n_{0c}$ respectively, and hot electrons and hot positrons with equal temperatures and equilibrium densities denoted by $T_h$ and $n_{0h}$, respectively.

We begin by deriving the general dispersion relation where each species $j$ has an isotropic, drifting Maxwellian velocity distribution with temperatures $T_j$ drifting parallel to the magnetic field $\mathbf{B_0} = B_0\hat{z}$, with drift velocities $V_{oj}$.

Hence, the equilibrium velocity distribution for the electron and positron species is chosen to be,

$$f_{\alpha 0} = \frac{n_{\alpha 0}}{\left(2\pi v_{tj}^2\right)^{\frac{3}{2}}} \exp\left\{\frac{-\left[V_x^2 + V_y^2 + \left(V_z - V_{oj}\right)^2\right]}{2v_{tj}^2}\right\}, \tag{30}$$

The Vlasov equations are,

$$\frac{\partial f_\alpha}{\partial t} + \mathbf{V}.\nabla f_\alpha + \frac{q_\alpha}{m}(\mathbf{E} + \mathbf{V} \times \mathbf{B}).\frac{\partial f_\alpha}{\partial \mathbf{V}} = 0, \tag{31}$$

and the equations of motion for the electrons and positrons is given by,

$$m\frac{d\mathbf{V}}{dt} = q_\alpha\{\mathbf{E} + \mathbf{V} \times \mathbf{B}\}, \tag{32}$$

where $j = c(h)$ for the cool (hot) species and $\alpha = ec, pc, eh$ and $ph$ for the cool electrons, cool positrons, hot electrons and hot positrons respectively, and $v_{tj} = \left(T_j/m\right)^{1/2}$ is the thermal velocity of the $j^{th}$ species.

Following standard techniques for electron-ion plasmas [29], the general kinetic dispersion relation for the four component, two temperature electron-positron plasma is given by

$$\begin{aligned} k^2 &+ \frac{2}{\lambda_{Dc}^2}\left[1 + \frac{\omega - \mathbf{k}.\mathbf{V_{oc}}}{\sqrt{2}k_\parallel v_{tc}} \sum_{p=-\infty}^{\infty} Z(z_{pc})\Gamma_{pc}\right] \\ &+ \frac{2}{\lambda_{Dh}^2}\left[1 + \frac{\omega - \mathbf{k}.\mathbf{V_{oh}}}{\sqrt{2}k_\parallel v_{th}} \sum_{p=-\infty}^{\infty} Z(z_{ph})\Gamma_{ph}\right] = 0, \end{aligned} \tag{33}$$

where $\lambda_{Dc,h} = \left(\varepsilon_0 T_h/n_{0c,h}e^2\right)^{1/2}$ is the Debye length for the cool (hot) species and $z_{pj}$ is the argument of the plasma dispersion function or Z-function [30] and is given by,

$$z_{pj} = \frac{\omega - \mathbf{k}.\mathbf{V_{oj}} - p\Omega_j}{\sqrt{2}k_\parallel v_{tj}}, \tag{34}$$

where,

$$\Gamma_{pj} = e^{-\alpha_j} I_p(\alpha_j), \tag{35}$$

and

$$\alpha_j = \frac{k_\perp^2 v_{tj}^2}{\Omega_j^2}, \tag{36}$$

where $I_p$ is the modified Bessel function of order $p$. The components of $\mathbf{k}$ parallel (perpendicular) to $\mathbf{B_0}$ are given by $k_\parallel$ ($k_\perp$) respectively, while $\mathbf{V_{oc}}$ and $\mathbf{V_{oh}}$ are the drift velocities of the cool (hot) species, respectively.

### 3.1 Approximate solutions of the kinetic dispersion relation

The general dispersion relation (33) can be numerically solved without any approximations. However, to get some insight into the solutions, here, approximate expansions of the plasma dispersion function are used to obtain analytical expressions for the frequency and growth rate of the acoustic mode.

In proceeding, for the temperatures it is assumed that $T_h \gg T_c (\sim 0)$. In addition low frequency modes satisfying $|\omega| \ll \Omega$ are considered. The series expansion of the Z-function [30] is given by

$$Z(z) = i\sqrt{\pi} e^{-z^2} - 2z\left[1 - \frac{2z^2}{3} + \frac{4z^4}{15} - \ldots\right] \text{ for } |z| \ll 1 \text{ and} \tag{37}$$

$$Z(z) = i\sqrt{\pi}\delta e^{-z^2} - \frac{1}{z}\left[1 + \frac{1}{2z^2} + \frac{3}{4z^4} + \ldots\right] \text{ for } |z| \gg 1. \tag{38}$$

where for $|z| \gg 1$, $\delta = \begin{cases} 0, & \mathrm{Im}(z) > 0 \\ 1, & \mathrm{Im}(z) = 0 \\ 2, & \mathrm{Im}(z) < 0 \end{cases}$

Assuming the drift of the electrons and positrons to be weak (i.e., small $V_{oc}$ and $V_{oh}$) [31] and $|\omega| \ll \Omega$,

$$z_{pc} = \frac{\omega - \mathbf{k}.\mathbf{V_{oc}} - p\Omega}{\sqrt{2}k_\parallel v_{tc}} \approx \frac{-p\Omega}{\sqrt{2}k_\parallel v_{tc}} \quad \text{for } p \neq 0 \tag{39}$$

and

$$z_{ph} = \frac{\omega - \mathbf{k}.\mathbf{V_{oh}} - p\Omega}{\sqrt{2}k_\parallel v_{th}} \approx \frac{-p\Omega}{\sqrt{2}k_\parallel v_{th}} \quad \text{for } p \neq 0. \tag{40}$$

Then for the cool species,

$$\sum_{p=-\infty}^{\infty} Z(z_{pc})\Gamma_{pc} \approx Z\left(\frac{\omega - \mathbf{k}.\mathbf{V_{oc}}}{\sqrt{2}k_\parallel v_{tc}}\right)\Gamma_{oc} + \sum_{p=1}^{\infty}\left\{Z\left(\frac{p\Omega}{\sqrt{2}k_\parallel v_{tc}}\right) + Z\left(\frac{-p\Omega}{\sqrt{2}k_\parallel v_{tc}}\right)\right\}\Gamma_{pc}. \tag{41}$$

From the definition of the Z-function, $Z(\xi) + Z(-\xi) = 0$, hence

$$\sum_{p=-\infty}^{\infty} Z(z_{pc})\Gamma_{pc} \approx Z(z_{oc})\Gamma_{oc}. \tag{42}$$

Taking the cooler species to be stationary, $V_{oc}$ is therefore set to zero, allowing only the hot species to drift. Then,

$$z_{oc} = \frac{\omega}{\sqrt{2}k_{\parallel}v_{tc}}. \tag{43}$$

For modes satisfying $\omega/k_{\parallel} \gg v_{tc}$, one may assume $|z_{oc}| \gg 1$, i.e., the wave phase speed along $\mathbf{B_o}$ is much larger than the cool electron thermal speed. For instability (i.e., a growing wave with $\mathrm{Im}(z)>0$), $\delta$ is set equal to zero in equation (38). Hence using the series expansion equation (38), equation (41) becomes

$$\sum_{p=-\infty}^{\infty} Z(z_{pc})\Gamma_{pc} \approx \left[-\frac{1}{z_{oc}} - \frac{1}{2z_{oc}^3} - \frac{3}{4z_{oc}^5}\right]\Gamma_{oc}. \tag{44}$$

Similarly, using the series expansion equation (37) (where $e^{-z_{oh}^2} \approx 1$ for $|z_{oh}| \ll 1$), we have for the hot species,

$$\sum_{p=-\infty}^{\infty} Z(z_{ph})\Gamma_{ph} \approx \left(i\sqrt{\pi} - 2z_{oh} + \frac{4z_{oh}^3}{3}\right)\Gamma_{oh}. \tag{45}$$

It is noted that for relatively high temperature $T_h$, the thermal velocity of the hot species is much larger than the wave phase velocity. Hence, for large $T_h$, we have assumed that $|z_{oh}| \ll 1$.

Substituting (44) and (45), $\lambda_D$, $\lambda_{Dc}$ and $\lambda_{Dh}$, into the dispersion relation (33), whereas before $\lambda_D = (\varepsilon_0 T_h/n_0 e^2)^{1/2}$, gives

$$k^2\lambda_D^2 + 2\frac{\frac{n_{0c}}{n_0}}{\frac{T_c}{T_h}}\left[i\sqrt{\pi}z_{oc}e^{-z_{oc}^2} - \frac{1}{2z_{oc}^2} - \frac{3}{4z_{oc}^4}\right] + 2\frac{n_{0h}}{n_0}\left[1 + i\sqrt{\pi}z_{oh}\Gamma_{oh}\right] = 0. \tag{46}$$

For the cool species we have assumed $|\alpha_c| = |k_{\perp}^2 v_{tc}^2/\Omega^2| = k^2\rho_c^2 \ll 1$ (where $\rho_c$ is the gyroradius of the cool species), i.e., long wavelength fluctuations in comparison to $\rho_c$. Since in general for $|x| \ll 1$ we can write $\Gamma_p(x) = e^{-x}I_p(x) \approx (x/2)^p(1/p!)$ $(1-x)$, hence we have $\Gamma_{oc} \approx 1$.

Second and higher order terms in $z_{oh}$ are also neglected since we have assumed $|z_{oh}| \ll 1$. Setting $\omega = \omega_r + i\gamma$ and assuming $\gamma/\omega_r \ll 1$ one may write

$$\frac{1}{\omega^2} \approx \frac{1}{\omega_r^2}\left(1 - \frac{2i\gamma}{\omega_r}\right). \tag{47}$$

Using the above manipulation the dispersion relation equation (46) becomes

$$\begin{aligned} k^2\lambda_D^2 &+ 2\frac{\frac{n_{0c}}{n_0}}{\frac{T_c}{T_h}}\left[i\sqrt{\pi}\left(\frac{\omega_r + i\gamma}{\sqrt{2}k_{\parallel}v_{tc}}\right)e^{-z_{oc}^2} - \frac{k_{\parallel}^2 v_{tc}^2}{\omega_r^2}\left(1 - \frac{2i\gamma}{\omega_r}\right) - \frac{3k_{\parallel}^4 v_{tc}^4}{\omega_r^4}\left(1 - \frac{2i\gamma}{\omega_r}\right)^2\right] \\ &+ 2\frac{n_{0h}}{n_0}\left[1 + i\sqrt{\pi}\left(\frac{\omega_r + i\gamma - \mathbf{k}.\mathbf{V_{oh}}}{\sqrt{2}k_{\parallel}v_{th}}\right)\Gamma_{oh}\right] = 0. \end{aligned} \tag{48}$$

Taking the real part of equation (48) with the charge neutrality condition $n_{oc} + n_{oh} = 1$, gives

$$\omega_r^2 = \frac{k^2 v_{ea}^2 \cos^2\theta}{1 + \frac{1}{2}k^2\lambda_{Dh}^2} + 3k^2 v_{tc}^2 \cos^2\theta, \tag{49}$$

where $\cos\theta = k_{\parallel}/k$ and $v_{ea} = (n_{0c}/n_{0h})^{1/2} v_{th}$ is the acoustic speed of the electron-positron plasma. It is noted that equation (49) is consistent with the expression (12) obtained from fluid theory.

The approximate solution of the growth rate is determined by taking the imaginary part of equation (48), and hence solving for $\gamma$, one finds

$$\gamma = \frac{\frac{\omega_r^4}{k_{\parallel}^3}\left(\frac{\pi}{8}\right)^{1/2}\left(\frac{m}{T_h}\right)^{3/2}\left[-\left(\frac{T_h}{T_c}\right)^{3/2} e^{-z_{oc}^2} + \left(\frac{n_{0h}}{n_{0c}}\right)\left(\frac{\mathbf{k}.\mathbf{V_{oh}}}{\omega_r} - 1\right)\Gamma_{oh}\right]}{\left[1 + \frac{6k_{\parallel}^2 \frac{T_c}{m}}{\omega_r^2}\right]}. \tag{50}$$

We note that in equation (50), it is the cooler species that provides the Landau damping, i.e., the velocity distribution function sees a negative slope $\left(\partial f_0/\partial V_{\parallel} < 0\right)$. It is also seen from equation (50) that for an unstable mode ($\gamma$>0), it is necessary that $V_{0h} > \omega_r/k_{\parallel}$, i.e., the drift velocity parallel to $\mathbf{B_0}$ of the hot species has to be larger than the phase velocity to overcome the damping terms.

Normalizing the fluid speeds by the thermal velocity $v_{th} = (T_h/m)^{1/2}$, the particle density by the total equilibrium plasma density $n_0 = n_{0c} + n_{0h}$, the temperatures by $T_h$, the spatial length by $\lambda_{dj} = \left(\frac{\varepsilon_0 T_j}{n_{0j} e^2}\right)^{1/2}$, and the time by $\omega_p^{-1} = \left(\frac{n_0 e^2}{\varepsilon_0 m}\right)^{-1/2}$, one may write the normalized real frequency as,

$$\omega_r^2 = \frac{2n_{0c}k_{\parallel}^2\lambda_d^2}{2(1-n_{0c}) + k^2\lambda_d^2} + 3k_{\parallel}^2\lambda_d^2\frac{T_c}{T_h}, \tag{51}$$

and the approximate normalized growth rate as,

$$\gamma_r = \frac{\frac{\omega_r^4}{k_{\parallel}^3\lambda_d^3}\left(\frac{\pi}{8}\right)^{1/2}\left[\left(\frac{1-n_{0c}}{n_{0c}}\right)\left(\vec{k}\,.\frac{\vec{V_{oh}}}{\omega_r} - 1\right)\Gamma_{oh}\right]}{\left[1 + \frac{6k_{\parallel}^2 \frac{T_c}{T_h}}{\omega_r^2}\right]}, \tag{52}$$

For a fixed value of $k\lambda_d$, the real frequency increases with an increase in the cool to hot temperature ratio. This can be seen from the approximate analytical expression (51). **Figure 2** displays the normalized growth rate as a function of the normalized wavenumber for varying cool to hot species temperature ratios $T_c/T_h$. It is noted that as the $T_c/T_h$ decreases, the growth rate increases, implying that the

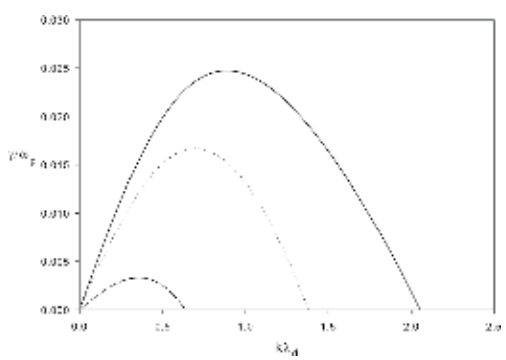


**Figure 2.**
*Normalized growth rate as a function of the normalized wavenumber. The fixed parameters are $R = 0.333$, $V_{oh} = 0.5$, $n_{0c} = 0.1$ and $\theta = 45^o$. The parameter labeling the curve is the cool to hot temperature ratio $T_c/T_h = 0.005$ (solid), 0.01 (dotted), and 0.02 (broken).*

instability is more easily excited with lower temperature ratios. This may be explained as follows. As the temperature of the cooler species is increased, the associated Landau damping increases, resulting in a reduction of the overall growth rate. It is noted that a cutoff $k\lambda_d$ value is reached beyond which the mode is damped.

## 4. Nonlinear electrostatic solitary waves in electron-positron plasmas

The study of nonlinear effects in electron-positron plasmas is important since these plasmas exhibit different wave phenomena as compared to electron-ion plasmas. It is therefore important to understand the nonlinear structures, especially the solitary waves that exist in electron-positron plasmas. Satellite observations in the Earth's magnetosphere have shown the existence of electrostatic solitary waves which forms part of broadband electrostatic noise (BEN) and electrostatic solitary waves (ESWs) in various regions of the Earth's magnetosphere. The characteristic features of these ESWs are solitary bipolar pulses and consist of small scale, large amplitude parallel electric fields. These large amplitude spiky structures have been interpreted in terms of either solitons [32] or isolated electron holes in the phase space corresponding to positive electrostatic potential [33]. Given that electron-positron plasmas are increasingly observed in astrophysical environments, as well as in laboratory experiments [34], the above mentioned satellite observations also lead one to explore if such nonlinear structures are also possible in electron-positron plasmas. There is a distinct possibility that a pulsar magnetosphere can support coexistence of two types of cold and hot electron-positron populations [10, 35, 28]. In this section we investigate nonlinear electrostatic spiky structures in a magnetized four component two-temperature electron-positron plasma.

### 4.1 Basic equations

The model considered, as in the previous section is a homogeneous magnetized, four component, collisionless, electron-positron plasma, consisting of cool electrons ($ec$) and cool positrons ($pc$) with equal temperatures $T_c$ and initial densities ($n_{ec0} = n_{pc0}$), and hot electrons ($eh$) and hot positrons ($ph$) with equal temperatures $T_h$ and densities ($n_{eh0} = n_{ph0}$). Wave propagation is taken in the $x$-direction at an angle $\theta$ to the magnetic field $\mathbf{B_0}$, which is assumed to be in the $x$-$z$ plane.

The continuity and momentum equations for the four species are given by

$$\frac{\partial n_j}{\partial t} + \frac{\partial (n_j v_{jx})}{\partial x} = 0 \tag{53}$$

$$\frac{\partial v_{jx}}{\partial t} + v_{jx}\frac{\partial v_{jx}}{\partial x} + \frac{1}{n_j m}\frac{\partial p_j}{\partial x} = -\frac{\varepsilon_j e}{m}\frac{\partial \phi}{\partial x} + \varepsilon_j \Omega v_{jy}\sin\theta \tag{54}$$

$$\frac{\partial v_{jy}}{\partial t} + v_{jx}\frac{\partial v_{jy}}{\partial x} = \varepsilon_j \Omega v_{jz}\cos\theta - \varepsilon_j \Omega v_{jx}\sin\theta \tag{55}$$

$$\frac{\partial v_{jz}}{\partial t} + v_{jx}\frac{\partial v_{jz}}{\partial x} = -\varepsilon_j \Omega v_{jy}\cos\theta, \tag{56}$$

where $\varepsilon_j = +1(-1)$ for positrons (electrons) and $j = ec, pc, eh, ph$ for the cool electrons, cool positrons, hot electrons, and the hot positrons, respectively.

The density of the cool electrons (positrons) is $n_{ec}$ ($n_{pc}$), and that of the hot electrons (positrons) is $n_{eh}$ ($n_{ph}$).

The general equation of state for the four species is given by

$$\frac{\partial p_j}{\partial t} + v_{jx}\frac{\partial p_j}{\partial x} + 3p_j\frac{\partial v_{jx}}{\partial x} = 0, \tag{57}$$

The system is closed by the Poisson equation

$$\varepsilon_0\frac{\partial^2\phi}{\partial x^2} = -e\left(n_{pc} - n_{ec} + n_{ph} - n_{eh}\right). \tag{58}$$

In the above equations, $n_j$, $\mathbf{v}_j$ and $p_j$ are the densities, fluid velocities and pressures, respectively, of the $j^{th}$ species. $\Omega = \Omega_e = \Omega_p = eB_0/m$ is the cyclotron frequency. Here $m = m_e = m_p$ is the common mass of the electrons and the positrons. Adiabatic compression, $\gamma = (2+N)/N$ =3, is assumed, where $N$ =1 implies one degree of freedom.

Upon linearizing and combining equations (53)–(58) and taking the limit $v_{tc} \ll \omega/k \ll v_{th}$, where $v_{th} = (T_h/m)^{1/2}$ and $v_{tc} = (T_c/m)^{1/2}$ are the thermal velocities of the hot (cool) species, the dispersion relation equation for a magnetized two-temperature four component electron-positron plasma, where all species are governed by the fluid equations is,

$$\omega^4 - \omega^2\left(\Omega^2 + 2\omega_s^2 + 3k^2v_{tc}^2\right) + 2\omega_s^2\Omega^2\cos^2\theta = 0. \tag{59}$$

where $\omega_{pc,ph} = \left(n_{0c,h}e^2/\varepsilon_0 m\right)^{1/2}$ are the plasma frequencies of the cool and hot species respectively and $\omega_s = \omega_{pc}/\left(1 + 2/3k^2\lambda_{Dh}^2\right)^{1/2}$ and $\lambda_{Dh} = \left(\varepsilon_0 T_h/n_{oh}e^2\right)^{1/2}$.

Solving the above dispersion relation gives the cyclotron mode,

$$\omega_+^2 = \left(\Omega^2 + 2\omega_s^2 + 3k^2v_{tc}^2\right) - \frac{2\omega_s^2\Omega^2\cos^2\theta}{\Omega^2 + 2\omega_s^2 + 3k^2v_{tc}^2} \tag{60}$$

and the acoustic mode,

$$\omega_-^2 = \frac{2\omega_s^2\Omega^2\cos^2\theta}{\Omega^2 + 2\omega_s^2 + 3k^2v_{tc}^2}, \tag{61}$$

### 4.2 Nonlinear analysis

In the nonlinear regime, a transformation to a stationary frame $s = (x - Vt)(\Omega/V)$ is performed, and $v, t, x$ and $\phi$ are normalized with respect to $v_{th}$, $\Omega^{-1}$, $\rho = v_{th}/\Omega$, and $T_h/e$, respectively. $V$ is the phase velocity of the wave. In equations (53)–(57), $\partial/\partial t$ is replaced by $-\Omega(\partial/\partial s)$ and $\partial/\partial x$ by $(\Omega/V)(\partial/\partial s)$, and the diving electric field amplitude is defined as $E = -(\partial\psi/\partial s)$, where $\psi = e\phi/T_h$.

Integrating equation (53) and using the initial conditions $n_{ec0} = n_0$ and $v_{ecx} = v_0$ at $s = 0$, yields the normalized velocity for the cool electrons in the x-direction.

$$v_{ecx} = -\left(\frac{n_{eco}}{n_{ec}}\right)(V - v_0) + V \tag{62}$$

Similarly the cool positrons, hot electrons and hot positrons velocities are determined. Substituting these into the normalized form of equations (53)–(57), gives

the following set of nonlinear first-order differential equations for the cool electron species in the stationary frame.

$$\frac{\partial \psi}{\partial s} = -E \tag{63}$$

$$\frac{\partial E}{\partial s} = R^2 M^2 \left(n_{pcn} - n_{ecn} + n_{phn} - n_{ehn}\right) \tag{64}$$

$$\frac{\partial n_{ecn}}{\partial s} = \frac{n_{ecn}^3 \left[E + M \sin\theta v_{ecyn}\right]}{\left(\frac{n_{ec0}}{n_0}\right)^2 (M - \delta_c)^2 - 3\frac{T_c}{T_h} p_{ecn} n_{ecn}} \tag{65}$$

$$\frac{\partial v_{ecyn}}{\partial s} = \frac{M n_{ecn}}{(M - \delta_c)} \left(\frac{n_0}{n_{ec0}}\right) \left[-\left(M - \frac{(M - \delta_c)}{n_{ecn}} \left(\frac{n_{ec0}}{n_0}\right)\right) \sin\theta + v_{eczn} \cos\theta\right] \tag{66}$$

$$\frac{\partial v_{eczn}}{\partial s} = -\left(\frac{n_0}{n_{ec0}}\right) \frac{n_{ecn} v_{ecyn} M \cos\theta}{(M - \delta_c)} \tag{67}$$

$$\frac{\partial p_{ecn}}{\partial s} = \frac{3 p_{ecn} n_{ecn}^2 \left[E + M \sin\theta v_{ecyn}\right]}{\left(\frac{n_{ec0}}{n_0}\right)^2 (M - \delta_c)^2 - 3\frac{T_c}{T_h} p_{ecn} n_{ecn}} \tag{68}$$

The set of differential equations for the cool positrons are given by,

$$\frac{\partial n_{pcn}}{\partial s} = \frac{n_{pcn}^3}{(M - \delta_c)^2} \left(\frac{n_0}{n_{pc0}}\right)^2 \left[-E - M \sin\theta v_{pcyn}\right] \tag{69}$$

$$\frac{\partial v_{pcyn}}{\partial s} = \frac{M n_{pcn}}{(M - \delta_c)} \left(\frac{n_0}{n_{pc0}}\right) \left[\left(M - \frac{(M - \delta_c)}{n_{pcn}} \left(\frac{n_{pc0}}{n_0}\right)\right) \sin\theta - v_{pczn} \cos\theta\right] \tag{70}$$

$$\frac{\partial v_{pczn}}{\partial s} = \left(\frac{n_0}{n_{pc0}}\right) \frac{n_{pcn} v_{pcyn} M \cos\theta}{(M - \delta_c)} \tag{71}$$

$$\frac{\partial p_{pcn}}{\partial s} = \frac{3 p_{pcn} n_{pcn}^2 \left[-E - M \sin\theta v_{pcyn}\right]}{\left(\frac{n_{pc0}}{n_0}\right)^2 (M - \delta_c)^2 - 3\frac{T_c}{T_h} p_{pcn} n_{pcn}} \tag{72}$$

Similar sets of differential equations can be derived for the hot electrons and hot positron species. The velocities are normalized with respect to the thermal velocity of the hot species $v_{th} = (T_h/m)^{1/2}$ and the densities with respect to the total density $n_0$. The equilibrium density of the cool (hot) electrons is $n_{ec0}$ $(n_{eh0})$, and that of the cool (hot) positrons $n_{pc0}$ $(n_{ph0})$, with $n_{ec0} + n_{eh0} = n_{pc0} + n_{ph0} = n_0$. $R = \omega_p/\Omega$, where $\omega_p = (n_0 e^2/\varepsilon_0 m)^{1/2}$ is the total plasma frequency, $M = V/v_{th}$ is the Mach number and $\delta_{c,h} = v_{0c,0h}/v_{th}$ is the normalized drift velocity of cool (hot) species at $s$ =0. The system of nonlinear first-order differential equations can now be solved numerically using the Runge-Kutta (RK4) technique [36]. The initial values can be determined self consistently where the actual normalized electric fields are given by $E_{norm} = -(1/M)(\partial\psi/\partial s)$ and wave propagation is taken almost parallel to the ambient magnetic field $\mathbf{B_0}$.

Numerical results to investigate the effect of parameters such as the electric driving force $E_0$, densities $n_{ec0}$ and $n_{ph0}$, temperature ratio $T_c/T_h$, Mach number $M$, drift velocities $\delta_{c,h}$ and propagation angle $\theta$ on the wave can be explored. A typical numerical result is seen in **Figure 3a–d** [37] showing the evolution of the system for various driving electric field amplitudes $E_0$. It is seen that as $E_0$ increases, the electric field structure evolves from a sinusoidal wave to a sawtooth structure. For a

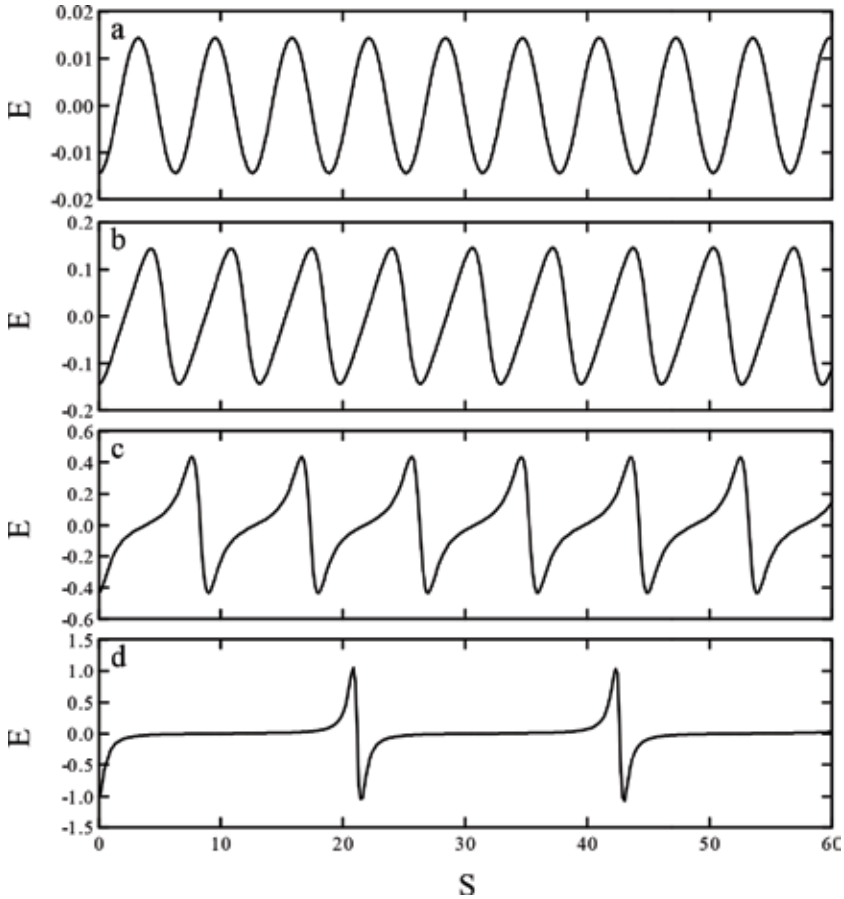


**Figure 3.**
*Numerical solution of the normalized electric field for the parameters $M = 3.5$, $\theta = 2^o$, $R = 10.0$, $\delta_c = \delta_h = 0.0$, $n_{ec0}/n_0 = n_{pc0}/n_0 = 0.5$, $T_c/T_h = 0.0$, and $E_0$ = (a) 0.05 [linear waveform], (b) 0.5 [sinusoidal waveform], (c) 1.5 [sawtooth waveform] and (d) 3.5 [bipolar waveform].*

higher $E_0$ value of 3.5, the potential structure has a spiky bipolar form showing that as the period of the wave increases and the frequency of the wave decreases.

## 5. Conclusion

Linear and nonlinear electrostatic waves in a magnetized four component two-temperature electron-positron plasma have been investigated. In the linear analysis fluid and kinetic theory approaches are employed to describe the wave motion. The fluid theory approach focused on the wave dynamics of both the acoustic and cyclotron branches. Solutions of the dispersion relation from fluid theory yielded electron-acoustic, upper hybrid, electron plasma and electron cyclotron branches. Perpendicular and parallel wave propagation was examined showing its influence on the dispersive properties of the wave. The kinetic theory approach further examined Landau damping effects on the acoustic mode, analyzing the frequency and growth rate of the wave. The analysis shows that a large enough drift velocity ($V_{oh}$) is required to produce wave growth. Both fluid and kinetic theory show excellent agreement for the real frequencies of the acoustic mode and solutions of the corresponding dispersion relation can be explored as a function of several

plasma parameters. In the nonlinear analysis, the two-fluid model is used to derive a set of differential equations for the electrostatic solitary waves in a magnetized two-temperature electron-positron plasma. In particular, electrostatic solitary waves and their electric fields, similar to those found in the Broadband Electrostatic Noise are explored. For the onset of spiky ESWs, it is noted that as the wave speed increases, a larger driving electric field is required.

## Acknowledgements

Thank you to Prof. Ramesh Bharuthram (University of the Western Cape, South Africa), Prof. Gurbax Lakhina and Prof. Satyavir Singh (Indian Institute of Geomagnetism, Navi Mumbai, India and Dr. Suleman Moolla (University of KwaZulu-Natal, Durban, South Africa) for your valuable contributions.

## Author details

Ian Joseph Lazarus
Department of Physics, Durban University of Technology, Durban, South Africa

*Address all correspondence to: lazarusi@dut.ac.za

## References

[1] Weinberg S. Gravitation and Cosmology. New York: Wiley; 1972

[2] Rees MJ. In: Gibbons GW, Hawking SW, Siklas S, editors. The Very Early Universe. Cambridge: Cambridge University Press; 1983

[3] Miller HR, Witta PJ. Active Galactic Nuclei. Berlin: Springer-Verlag; 1987. p. 202

[4] Piran T. The physics of gamma-ray bursts. Reviews of Modern Physics. 2005;**76**:1143

[5] Goldreich P, Julian WH. Pulsar Electrodynamics. The Astrophysical Journal. 1969;**157**:869

[6] Michel FC. Theory of pulsar magnetospheres. Reviews of Modern Physics. 1982;**54**:1

[7] Tandberg EH, Emslie AG. The Physics of Solar Flares. Cambridge: Cambridge University Press; 1988. p. 124

[8] Beskin VS, Gurevich AV, Istomin YN. Electrodynamics of pulsar magnetospheres. Soviet Physics—JETP. 1983;**58**:235

[9] Bharuthram R. Arbitrary Amplitude Double Layers in a Multi-Species Electron-Positron Plasma. Astrophysics and Space Science. 1992;**189**:213

[10] Sturrock PA. A Model of Pulsars. The Astrophysical Journal. 1971;**164**:529

[11] Berezhiani VI, Mahajan SM. Large relativistic density pulses in electron-positron-ion plasmas. Physical Review E. 1995;**bf52**:1968

[12] Shatashvili NL, Javakhishvili JI, Kaya H. Nonlinear Wave Dynamics in Two Temperature Electron-Positron-Ion Plasma. Astrophysics and Space Science. 1997;**250**:109

[13] Bhattacharyya R, Janaki MS, Dasgupta B. Relaxation in electron-positron plasma: a possibility. Physics Letters A. 2003;**315**:120

[14] Stenflo L, Shukla PK, Yu MY. Nonlinear Propagation of Electromagnetic Waves in Magnetized Electron-Positron Plasmas. Astrophysics and Space Science. 1985;**117**:303

[15] Mofiz UA, de Angelis U, Forlani A. Solitons in weakly nonlinear electron-positron plasmas and pulsar microstructure. Physical Review A. 1985;**31**:951

[16] Yu MY, Shukla PK, Stenflo L. Alfven Vortices in a Strongly Magnetized Electron-Positron Plasma. The Astrophysical Journal. 1986;**309**: L63

[17] Pillay R, Bharuthram R. Large Amplitude Solitons in a Multi-Species Electron-Positron Plasma. Astrophysics and Space Science. 1992;**198**:85-93

[18] Verheest F, Lakhina GS. Oblique Solitary Alfv $e^{'}$ n Modes in Relativistic Electron-Positron Plasmas. Astrophysics and Space Science. 1996;**240**:215

[19] Lazarus IJ, Bharuthram R, Hellberg MA. Modified Korteweg-de Vries-Zakharov-Kuznetsov solitons in symmetric two-temperature electron-positron plasmas. Journal of Plasma Physics. 2008;**74**:519

[20] Zank GP, Greaves RG. Linear and nonlinear modes in nonrelativistic electron-positron plasmas. Physics Review. 1995;**51**:6079

[21] Iwamoto N. Collective modes in nonrelativistic electron-positron

plasmas. Physical Review E. 1993;**47**: 604

[22] Mozer FS, Ergun R, Temerin M, Cattell CA, Dombeck J, Wygant JR. New Features of Time Domain Electric-Field Structures in the Auroral Acceleration Region. Physical Review Letters. 1997; **79**:1281

[23] Andre M, Koskinen H, Gustafsson G, Lundin R. Ion waves and upgoing ion beams observed by the Viking satellite. Geophysical Research Letters. 1987;**14**: 463

[24] Matsumoto H, Kojima H, Miyatake T, Omura Y, Okada M, Nagano I, et al. Electrostatic Solitary Waves (ESW) in the magnetotail: BEN wave forms observed by GEOTAIL. Geophysical Research Letters. 1994;**21**:2915

[25] Franz JR, Kintner PM, Pichett JS. POLAR Observations of Coherent Electric Field Structures. Geophysical Research Letters. 1998;**25**:1277

[26] Ergun RE, Carlson CW, McFadden JP, Mozer FS, Delroy GT, Peria W, et al. FAST satellite observations of large-amplitude solitary wave structures. Geophysical Research Letters. 1998;**25**: 2041

[27] Gary SP, Tokar RL. The electron acoustic Mode. Physics of Fluids. 1985; **28**:2439

[28] Lazarus IJ, Bharuthram R, Singh SV, Pillay SR, Lakhina GS. Linear electrostatic waves in two-temperature electron-positron plasmas. Journal of Plasma Physics. 2012;**78**:621

[29] Bharuthram R, Pather T. The kinetic dust-acoustic instability in a magnetized dusty plasma. Planetary and Space Science. 1996;**44**:137

[30] Fried BD, Conte SD. The Plasma Dispersion Function. New York: Academic Press; 1961

[31] Rosenberg M. Ion- and dust-acoustic instabilities in dusty plasmas. Planetary and Space Science. 1993;**41**: 229

[32] Temerin MA, Cerny K, Lotko W, Mozer FS. Observations of double layers and solitary waves in the auroral plasma. Physical Review Letters. 1982;**48**:1175

[33] Omura Y, Kojima H, Matsumoto H. Computer simulation of Electrostatic Solitary Waves: A nonlinear model of broadband electrostatic noise. Geophysical Research Letters. 1994;**21**: 2923

[34] Greaves RG, Surko CM. An Electron-Positron Beam-Plasma Experiment. Physical Review Letters. 1995;**75**:3846

[35] Bharuthram R. Arbitrary Amplitude Double Layers in a Multi-Species Electron-Positron Plasma. Astrophysics and Space Science. 1992;**189**:213

[36] Press WH, Teukolsky SA, Vetterling WT, Flannery BP. Numerical Receipes in Fortran 90-The Art of Parallel Scientific Computing. 1996;**2**:702, 731, 1297-704, 740, 1308

[37] Lazarus IJ, Bharuthram R, Moolla S, Singh SV, Lakhina GS. Nonlinear electrostatic solitary waves in electron-positron plasmas. Journal of Plasma Physics. 2016;**82**:1

Section 4

# Application of Charge Particles

Chapter 6

# Biological Effects of Negatively Charged Particle-Dominant Indoor Air Conditions

*Suni Lee, Yasumitsu Nishimura, Naoko Kumagai-Takei, Hidenori Matsuzaki, Megumi Maeda, Nagisa Sada, Kei Yoshitome and Takemi Otsuki*

## Abstract

To identify health-promoting indoor air conditions, we developed negatively charged particle-dominant indoor air conditions (NCPDIAC). Experiments assessing the biological effects of NCPDIAC comprised (1) 2.5-h stays in NCPDIAC or control rooms, (2) 2-week nightly stays in control followed by NCPDIAC rooms, (3) 3-month OFF to ON and ON to OFF trials in individual living homes equipped with NPCDIAC in their sleeping or living rooms, and (4) in vitro assays comparing the immune effects between negatively charged particle-dominant and control cell culture incubators. The most significant difference examined between NCPDIAC and control rooms in the 2.5-h stays was an increase in interleukin (IL)-2 with occupancy of the NCPDIAC room. For the 2-week nightly stay experiments, natural killer (NK) cell activity increased with occupancy of the NCPDIAC room. The 3-month OFF to ON trial showed an increase in NK cell activity, while the ON to OFF trial yielded a decrease in NK cell activity. Additionally, the in vitro assays also showed an increase in NK cell activity. The use of NCPDIAC resulted in increased NK cell activity, which has the effect of enhancing immune surveillance for the occurrence of cancer and improving symptoms associated with viral infections.

**Keywords:** indoor air, negatively charged particle, natural killer cell activity

## 1. Introduction

Indoor air conditions can sometimes affect human health. For example, sick building syndrome (SBS) is one of the most well-known health impairments caused by indoor air conditions [1–3]. Volatile organic compounds (VOCs) are considered to be the cause of SBS [1–3]. SBS can induce a variety of signs or symptoms such as headache; eye, nose, and throat irritation; fatigue; dizziness; and nausea. The condition of patients with SBS may worsen following exposure to certain VOCs, with individual patients revealing specific hypersensitivity to particular chemicals. It is considered that some pathophysiological alterations in the psycho-neuro-immune-endocrine network at the level of genes, molecules, proteins, cells, and

organs may occur in SBS patients, which then defines or determines their sensitivity to such low concentrations of VOCs [1–3]. However, the precise nature of these alterations is yet to be delineated. Consequently, the only advice presently available to SBS patients is to avoid exposure to VOCs for which the patient shows particular sensitivity [1–3].

Furthermore, most homes in Japan possess air-conditioning units in each room. During the winter season, the room adjacent to the bathroom which is utilized for changing clothes is narrow and particularly cold. Moreover, the lavatory is also cold. Consequently, there is a risk of changes in blood pressure and the onset of cardiovascular events caused by drastic changes in room temperature in these areas [4, 5].

Thus, decreasing the amount and use of chemicals and maintaining appropriate room temperatures at home are things that can be considered with respect to the task of establishing health-promoting indoor conditions. Additionally, although there are few reports detailing the use of indoor air under negatively charged conditions, a consideration of air electrical charges may assist with this task [6–9].

## 2. Development of NCPDIAC

The development of NCPDIAC has previously been reported [10].

As shown in **Figure 1**, NCPDIAC was established using extraporous charcoal paint and loading an electric voltage (approximately 72–100 V) behind the room walls [10]. The charcoal paints were mainly used for deodorization and dehumidification. As a result, the surface of the walls acquired a slightly negative charge, and small positively charged particles 20–30 nm in diameter collected on the surface of walls [10]. Thus, although negatively charged particles were not introduced into the

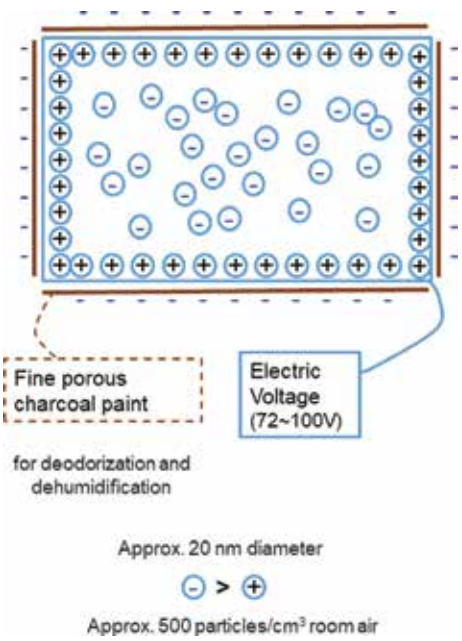


**Figure 1.**
*NCPDIAC was established using extraporous charcoal paint and loading an electric voltage behind the walls.*

indoor conditions, the balance between positively and negatively charged particles was such that negatively charged particles were predominant [10].

## 3. 2.5H stay experiments

Results of the 2.5H (2.5-h) stay experiments have previously been reported [10].

Three control rooms and three NCPDIAC rooms were built in the wide subunderground laboratory. Both types of rooms were built in a large subunderground laboratory in the Comprehensive Housing R&D Institute, SEKISUI HOUSE, Ltd., at Kizu-town, Kyoto prefecture, Japan. The area and volume of the laboratory were approximately 539 $m^2$ and 1564 $m^3$, respectively, and those of the experimental rooms were 9.1 $m^2$ and 22.8 $m^3$, respectively. The appearance of the control and NCPDIAC rooms is shown in **Figure 2A**. All of the healthy volunteers (HV) referred to in **Figure 2B** were unaware of the room type (control or NCPDIAC) they were to occupy during the experimental period. The following items were measured immediately prior to (prestay) and following (poststay) entry into the rooms as previously reported [10].

1. General conditions: blood chemistry including liver [alanine aminotransferase (ALT), aspartate aminotransferase (AST), and gamma-glutamyl transferase (γGT)] and kidney functions [creatinine, blood urea nitrogen (BUN) and uric acid], blood sugar and lactic acid levels, and peripheral blood counts (white blood cell, red blood cell, hemoglobin, hematocrit and platelet) were measured using peripheral venous blood. Blood pressure and pulse rate were also measured.

2. Stress markers: Levels of blood cortisol and salivary cortisol, chromogranin A, amylase, and secretory immunoglobulin A were measured as stress markers.

3. Parameters related to the autonomic nervous system: The autonomic nervous system was examined using the Flicker test, a stabilometer, and heart rate monitor for 3 min. The Flicker test and flicking frequencies of red, green, and yellow colors were monitored. A Gravicoder GS-7TM instrument (Anima Inc., Tokyo, Japan) was used as a stabilometer and the Romberg ratio was used as the parameter for body sway. The ratio was calculated from the whole trajectory of the body sway during a 30-s standing period with eyes closed divided by that with eyes open. The heart rate was monitored using a Heart Rate Monitor S810iTM instrument (Polar Electro, Kempele, Finland) for 3 min. During monitoring, HV sat on chairs and were kept at rest. The R wave intervals in the electrocardiogram were estimated and the standard deviation (SD) or R wave interval was considered as an index of heart rate fluctuation.

4. Immunological parameters: Serum levels of immunoglobulin (Ig) E and Ig A, and cytokines related to the Th1/Th2 balance [Interferon (IFN)-γ, tumor necrosis factor (TNF)-α, Interleukin (IL)-2, IL-4, IL-6 and IL-10] were evaluated. Individual samples for cytokine measurement were applied to the Cytometric Bead Array of Human Th1/Th2 cytokine kit II (CBA, BD Bioscience, San Jose, CA, USA) and measurements were made using FACSCalibur flow cytometry (BD Bioscience) according to the manufacturer's instructions. For samples that revealed less than the lower limit of the values from analytical methods for cytokines and immunoglobulins, the 1/10 value of the minimum values among the entire measurable samples was substituted instead of 0 or left as "unmeasurable," as previously reported [10].

5. Blood viscosity: Blood viscosity was measured using a Micro-Channel Flow Analyzer MC-FAN (MC Laboratory Inc., Tokyo, Japan) according to the manufacturer's instructions. Briefly, peripheral heparinized blood sample (100 µl) was placed into the instrument and allowed to flow through the microchannel chips, which are a model for capillary vessels, and the flowing time was recorded. The flowing blood sample was visualized using a CCD camera equipped to the microscope.

These experiments were approved by the institutional ethical committee (#114). Samples were only taken from HV who provided written informed consent.

The electrical charge in these rooms was measured using an Ion Counter EB-1000TM instrument made by Eco Holistic Inc., Suita, Japan.

Differences in the positively and negatively charged particles in control and NCPDIAC rooms are shown in **Figure 2C**. The number of positively charged particles in the rooms with NCPDIAC was reduced. However, the number of negatively charged particles in control and NCPDIAC rooms did not differ. Negatively charged air conditions were therefore formed by reducing the number of positively charged particles in NCPDIAC rooms.

Differences between control and NCPDIAC room values for all items measured were determined by calculating [poststay]-[prestay]. As shown in **Figure 2D**, differences were found in IL-2 [10]. The increase in IL-2 levels (by approximately 1 pg/ml)

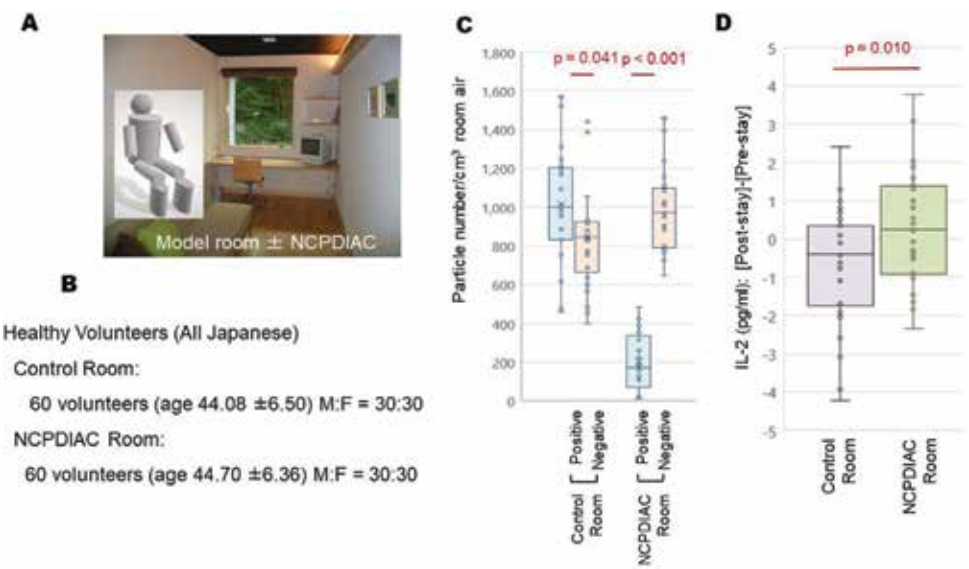


**Figure 2.**
*(A) Control and NCPDIAC rooms were constructed as shown. Healthy volunteers occupied rooms for 2.5 h, being unaware of the room type (control or NCPDIAC). Volunteers remained within the rooms in a stable state, without sleeping or excitement. (B) A total of 60 Japanese volunteers participated in experiments for each room type. The gender ratio and average age of the volunteers were almost identical in both groups (occupants of control and NCPDIAC rooms). (C) The box-and-whisker plots show the number of positively and negatively charged particles per 1 cm³ air in control and NCPDIAC rooms. Although there was no difference in the level of positively and negatively charged particles in control rooms, NCPDIAC rooms possessed significantly lower levels of positively charged particles compared with control rooms. Furthermore, there was no difference in the level of negatively charged particles between control and NCPDIAC rooms. Statistical differences were assayed using the student T test. (D) The box-and-whisker plots show a comparison of IL-2 levels ([Post-Stay]-[Pre-Stay], pg/ml) in volunteers who occupied the control and NCPDIAC rooms during the 2.5-h stay experiments. The most significant difference found in the examined values using [poststay]-[prestay] related to IL-2 levels, which increased significantly following NCPDIAC room stays compared with control room stays. This difference was analyzed using the Mann-Whitney U test.*

was considered not to be caused by any pathophysiological conditions. Additionally, it was considered that levels could return to base values in individual HV. As a result, it appears that NCPDIAC affected the immune system without any adverse effects with respect to the signs, symptoms, or measured items in the present experiments [10].

## 4. 2W nightly stay experiments

In the next step, 2W (2-week) nightly stay experiments were performed as previously reported [11].

Approximately 1 year after obtaining the results of the 2.5H experiments and with subsequent discussions, new participants were recruited for our 2W nightly stay experiments. This study was approved by the institutional ethical committee (#176) and samples were only taken from HV who provided written informed consent.

The dormitory belonging to SEKISUI HOUSE, Ltd., Kizugawa-City, Kyoto Prefecture, Japan, and ordinarily used for the training of employees was utilized for our 2W nightly stay experiments. These employees usually receive training for 3 months as shown in **Figure 3A**. Then, in the case of volunteers for our experiments, employees were moved at the second month from their original room into a control

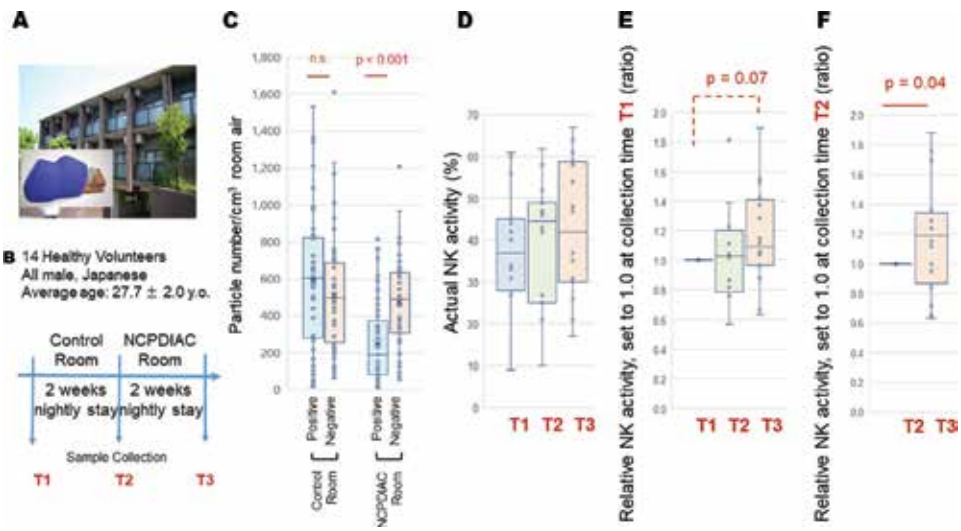


**Figure 3.**
*(A) For the 2W (2-week) nightly stay experiments the dormitory for training employees was used. (B) All volunteers initially occupied the control room every night for 2 weeks. Thereafter, volunteers occupied NCPDIAC rooms without being aware of which room type (control or NCPDIAC) they had initially occupied. Sample collections were performed at T1, T2, and T3 time points. T1 represented the time point prior to volunteers occupying the control room. T2 represented the time point immediately following the 2W nightly stay in control rooms, and just prior to occupancy of the NCPDIAC room, while T3 represented the time point following the 2W nightly stay in the NCPDIAC room. Although HV agreed to be recruited in this study, they were unaware of the room type (control or NCPDIAC) they had initially entered. (C) The box-and-whisker plots show the number of positively and negatively charged particles per 1 cm³ air in control and NCPDIAC rooms. Although there was no difference between the number of positively and negatively charged particles in control rooms, NCPDIAC rooms possessed significantly lower levels of positively charged particles compared with control rooms. Furthermore, there was no difference in the level of negatively charged particles between control and NCPDIAC rooms. Statistical analyses were performed using the student T test. (D) The box-and-whisker plots show the actual NK cell activity (%) at T1, T2, and T3 time points. There were no differences among the three time points. Statistical analyses were performed using the ANOVA test. (E) The box-and-whisker plots show the relative NK activity after setting T1 of individual volunteers to 1.0. Statistical analyses comparing T1 and T2 or T3 were performed using the student T test. (F) Relative NK activity after setting T2 of individual volunteers to 1.0. There was a significant increase in relative NK activity after the 2W nightly stay in the NCPDIAC rooms. Statistical analyses were performed using the student T test.*

(both were the same in terms of NCPDIAC). After occupying the control room every night for 2 weeks, they were then moved into NCPDIAC rooms, without being aware of the room type (control or NCPDIAC) they had initially occupied. As shown in **Figure 3B**, sample collections were performed prior to volunteers occupying the control room (T1), after their 2W nightly stay in the control room (T2), and finally after occupying the NCPDIAC room (T3). The measured items remained unchanged during the 2.5H stay experiments. Additionally, several parameters that had not changed during the hour-based time period but were altered during the week-based time period when environmental factors or physiological conditions had changed were included as biological parameters. Those parameters comprised NK cell activity, along with urine 17 hydroxycorticosteroid (OHCS) and 8-oxo-2′-deoxyguanosine (OHdG) levels.

All volunteers initially occupied the control room every night for 2 weeks. Thereafter, volunteers occupied NCPDIAC rooms without being aware of which room type (control or NCPDIAC) they had initially occupied. Sample collection was performed at T1, T2, and T3 time points. T1 represented the time point prior to volunteers occupying the control room. T2 represented the time point immediately following the 2W nightly stay in control rooms, and just prior to occupancy of the NCPDIAC room, while T3 represented the time point following the 2W nightly stay in the NCPDIAC room.

Among all the items measured, significant change was only found in the NK activity. The NK cell activity was determined using a $^{51}$Cr-release assay according to a method outlined in previous reports [12, 13]. The effector cell (mononuclear cell)-to-target cell (K562 cell) ratio was 10:1. However, there was a wide range of individual actual NK cell activity in the vicinity of approximately 10% to greater than 50%. In the 2W nightly stay experiments, the NK cell activity among HV ranged from less than 30% to near 60% at T1 (**Figure 3B**). Although actual NK activity measurements did not reveal any statistical significance (**Figure 3D**) due to the wide variation in individual volunteers, when the relative NK activity was set to 1.0 at T1, there was a tendency toward increased NK cell activity at T3 (**Figure 3E**) [11]. Since the room conditions prior to T1 and T2 collections were basically the same, the relative NK cell activity between T2 and T3 was compared, with T2 being set to 1.0 in individual HV [11]. As shown in **Figure 3F**, there was a significant increase in relative NK activity at T3, after the 2W nightly stay with NCPDIAC [11].

## 5. In vitro experiments

The in vitro experiments were performed to examine cellular alterations under negative particle dominant conditions. Results have previously been reported [14].

Freshly isolated peripheral blood mononuclear cells derived from seven healthy volunteers were cultured in a standard $CO_2$ incubator at 37°C with 5% $CO_2$ under humidified conditions (standard cell culture conditions comprised a humidity of 95%). For these experiments, it was impossible to use charcoal paint or to load an electric voltage. Thus, negatively charged particles were forced in and circulated. The difference between positively and negatively charged particles in 1 $cm^3$ of incubator air was approximately 3000 (**Figure 4A**) [14].

This study was approved by the institutional ethical committee (#883) and samples were only taken from the HV who provided written informed consent. Peripheral blood mononuclear cells were derived from samples obtained from HV.

For the NK cell activity, K562 cells, a human immortalized myelogenous leukemia cell line, were stained with Vybrant™ Dio Cell-Labeling Solution by incubation for 20 min at room temperature [14]. Dio-stained cells were then washed with phosphate buffered slain (PBS), and peripheral blood mononuclear cells (PBMC)

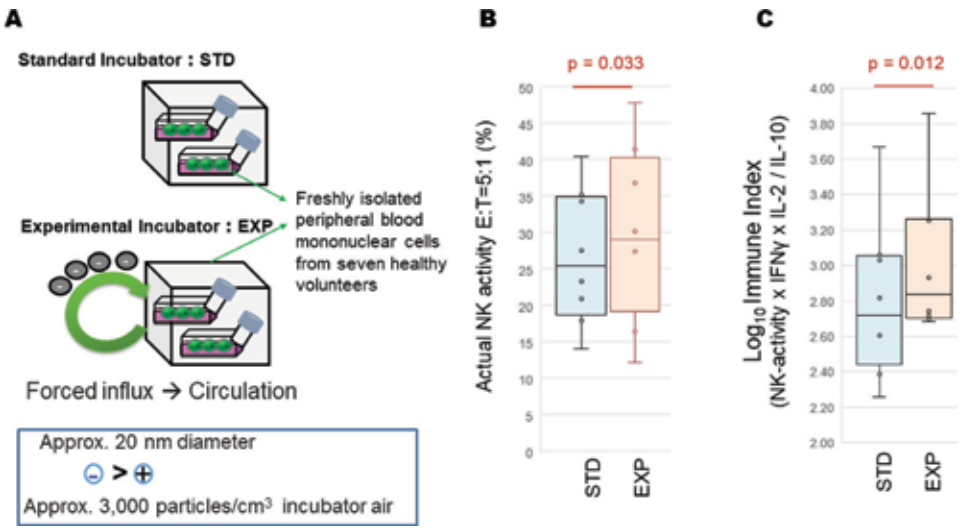


**Figure 4.**
*(A) Peripheral blood mononuclear cells from HV were incubated in standard (STD) or experimental (EXP) incubators. Negatively charged particles (20–30 nm in diameter) were forced into incubators and then circulated. The experimental incubator was set to generate negatively charged particles using a neutralizing instrument that created negatively charged particles (SJ-M200, Keyence Co. Ltd., Osaka, Japan). This instrument yielded negatively charged particles that were set to directly enter the inside of the incubator (by making a hole). Since the interior volume of the incubator was 49 l, the negatively charged particles entered and passed out at a rate of approximately 3000 particles/cm$^3$. (B) The box-and-whisker plots show the increase in actual NK cell activity, represented by the E/T (effector vs. target cells) ratio, which, being 5:1, showed greater increase with experimental incubators and negatively charged particle-dominant culture conditions compared with standard incubators. (C) The LOG$_{10}$ value of the "immune index" as [NC-activisty X IFN-γ concentration X IL-2 concentration]/[IL-10 concentration] was compared between standard and experimental incubator conditions. Experimental incubator conditions showed a significant increase in this index.*

were incubated with 5000 Dio-labeled K562 cells in 96-well round bottom plates at an effector cell-to-target cell (E/T) ratio of 2.5:1, 5:1, or 10:1 for 5 h in experimental or standard incubators. Following incubation, cells were collected and stained with propidium iodide (PI) at 5 μg/ml and the percentage of PI+ Dio-labeled cells among the total Dio-labeled cells, representing the percentage of lysed cells, was examined using FACSCalibur flow cytometry. The percentage of specific lysis induced by effector cells was calculated after analyzing the substrate and spontaneous dead cell numbers expressed in wells without effector [14].

Additionally, peripheral blood mononuclear cells were cultured in RPMI1640 culture medium with antibiotics just as for standard cell cultures for 1 or 2 weeks without any stimulants such as cytokines. The concentrations of IFN-γ, IL-2, and IL-10 (as well as IL-6, TNF-α, and IL-4) in supernatants were measured. Additionally, other items such as surface CD25, CD69, programmed death-1 (PD1), and CD44 expression in CD4+ T helper cells, CD8+ T cells, and NK cells were measured [14].

It is noteworthy that NK cell activity was significantly higher when incubations were performed in the experimental incubator compared with those performed in the standard incubator (**Figure 4B**). Additionally, if we calculate the "immune index" as [NC-activity X IFN-γ concentration X IL-2 concentration]/[IL-10 concentration] and compare this index from standard and experimental incubators using $\log_{10}$ titer (**Figure 4C**), there is a significantly greater increase in this "$\text{Log}_{10}$ Immune Index" associated with the use of experimental incubators compared with the use of standard incubators. The higher value of this item was assumed to reflect stimulation of immune status [14].

These results indicated that a predominance of negatively charged particles induces immune stimulation at non-pathophysiological levels [14].

## 6. 3M ON and OFF trials

Finally, long-term (3-month, or 3M) stay experiments were performed and the results have previously been reported [15].

Following the aforementioned experiments (2.5H and 2W nightly stay experiments and evaluations), it seemed that NCPDIAC stimulated NK activity with no adverse effects on HV [15]. The increase in NK activity could be accounted for by the short-term, albeit slight, increase in IL-2, which may activate NK cells during the 2W period. The following experiments were then applied in living homes. The homes of seven volunteers were modified for NCPDIAC, targeting mainly sleeping rooms and living rooms. A switch panel approximately 4 × 22 × 29 cm in size had been fitted. Volunteers would then switch this panel ON and OFF every 3 months. Then, prior to and following every 3-month ON or OFF living period, clinical measurements including NK cell activity and others (as measured in the 2W nightly stay experiments) were performed. A total of 16 OFF to ON (3M ON) and 13 ON to OFF (3M OFF) trials were performed as shown in **Figure 5A** [15].

Blood samples were taken just before switching ON or OFF. Thus, during the OFF to ON (3M ON) period, HV stayed at home with NCPDIAC (sleeping room and living room). During the ON to OFF (3M OFF) period, HV occupied rooms in their homes without NCPDIAC [15].

All seven HV comprised Japanese living in Japan and were asked to join this project by first-class registered architects who are colleagues of the authors. The average age of the volunteers was 54.86 ± 9.15 years and included five males and two females.

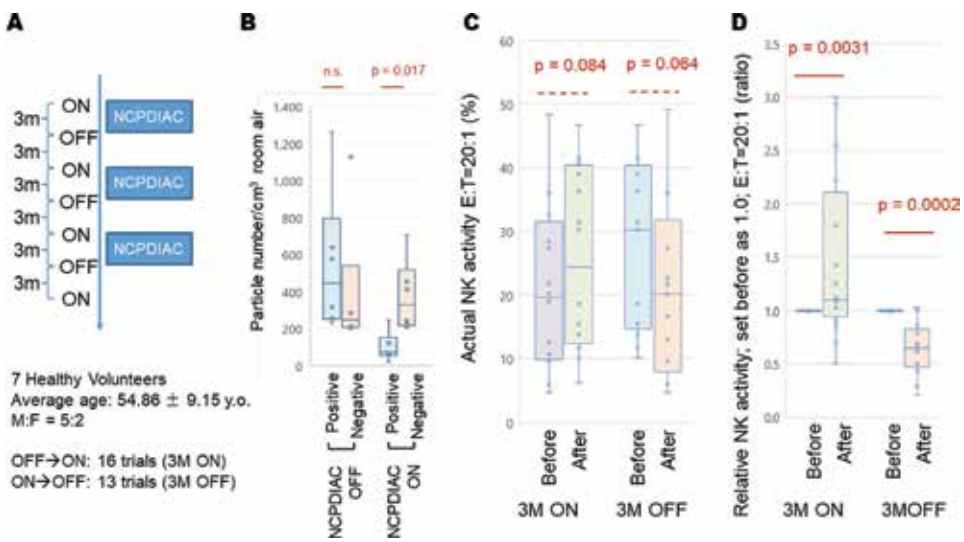


**Figure 5.**
*(A) Seven healthy volunteers utilized sleeping and living rooms with NCPDIAC in their homes. During this period, the occupants themselves would switch NCPDIAC ON and OFF. Sixteen trials of OFF to ON (3M ON) and thirteen trials of ON to OFF (3M OFF) were executed. (B) The levels of positively and negatively charged particles in the representative six rooms including the homes of HV where the NCPDIAC apparatus was set were measured using as ion counter (EM-1000, Eco Holistic Inc., Suita, Japan) during the OFF and ON periods. During the OFF period, there was no difference between positively and negatively charged particles; however, during the ON period, the level of positively charged particles was significantly reduced, thereby establishing a difference between the number of positively and negatively charged particles. Statistical analyses were performed using the student T test. (C) Changes in actual NK cell activity prior to and following the 3M ON and 3M OFF periods. Values tended to increase during the 3M ON and decrease during the 3M OFF periods. (D) Relative NK cell activities with NK cell activity previously set to 1.0. There was a significant increase in relative NK cell activity during the 3M ON period and a significant decrease during the 3M OFF period. Statistical analyses were performed using the student T test.*

All volunteers had built or renovated their residential homes prior to being recruited to this project and agreed to set up an NCPDIAC device for the experiments [15].

This study was approved by the institutional ethical committee (#854) and samples were only taken from HV who provided written informed consent.

The clinical parameters measured were similar to those determined for the 2W nightly stay experiments with additional cytokines being measured. Twenty-nine cytokines were measured using the Luminex 26 Cytokine Plex Kit Human Cytokine/Chemokine Panel (MPXHCYTO60KPMX26, Merck Millipore, Billerica, MA) [15]. Additionally, adipokines and cytokines related to oxidative stress in serum from 16 ON and 13 OFF trials were measured using the Human Adipokine Magnetic 14-Plex Panel with Luminex instruments (Bio-rad, Hercules, CA, USA). Fourteen of the cytokines examined comprised IL-1β, IL-10, IL-6, monocyte chemotactic protein (MCP)-1, leptin, SAA (serum amyloid A), hepatocyte growth factor (HGF), insulin, lipocalin-2, TNF-α, B cell activating factor (BAFF: belonging to the tumor necrosis factor family), resistin, plasminogen activator inhibitor (PAI)-1, and IL-8 [16].

After analyzing all of the results, it was determined that all items measured except for NK activity revealed no significant difference between 3M ON and 3M OFF conditions. NK activity was measured as the E/T ratio and was calculated to be 10:1 and 20:1. With an actual NK activity of 20:1, there was a tendency of NK activity to increase in the 3M ON period and decrease in the 3M OFF period [15]. Additionally, the relative changes in NK activity set before as 1.0 for individual values of 3M ON and 3M OFF periods revealed a significant increase during the 3M ON periods and a decrease during the 3M OFF periods in the 20:1 E/T ratio as shown in **Figure 5C** [with an E/T ratio of 10:1, similar significant results were obtained in the 3M ON ($p = 0.017$) and 3M OFF ($p = 0.012$) periods] [15].

Taken together, it was shown that NCPDIAC cause enhancement of NK cell activity even in living homes. The apparatus utilized for establishing NCPDIAC may possess advantages in reducing the occurrence of cancers, as well as reducing signs or symptoms associated with virus-infected diseases such as influenza [15].

For adipokines and cytokines related to oxidative stress, there were no significant changes observed [16]. However, with the exception of one case, serum amyloid A (SAA) levels decreased significantly during the ON trials (data not shown) [16]. Considering that SAA is an acute phase-reactive protein like C-reactive protein (CRP), this observed decrease may indicate a prevention of cardiovascular and atherosclerotic changes, since an increase in high-sensitive CRP is associated with subsequent detection of these events [16].

## 7. Discussion

Initial assessment of the biological effects of NCPDIAC began with evaluations of 2.5H stay experiments since similar experiments had yet to be reported and investigations should involve collaboration with HV. Thus, our initial 2.5H stay experiments demonstrated a small but significant increase in IL-2. Additionally, it was assumed that there were no adverse effects during the 2.5H period. These experiments were then followed with 2W nightly stay experiments. However, to set up NCPDIAC in the homes of HV was very difficult since sleeping and/or living rooms required alterations. Thus, we used a dormitory that belonged to the collaborating house company where many trainees (company employees) would be staying during the 3M period. With these experiments, we found an enhancement of NK cell activity during the 2W nightly stay. Additionally, there were no adverse effects as determined by the various parameters examined.

During these studies employing HV, in vitro assays were performed. From the in vitro experiments, we confirmed the increased NK cell activity and slight immune-stimulatory effects of negatively charged particles. Again, there were no adverse effects to the human body as determined by the various parameters examined.

These results encouraged us to apply NCPDIAC in the actual homes (sleeping and living rooms) of volunteers. Following approval by the institutional ethical committee and obtaining written informed consent, the homes of 7 HV were set up with NCPDIAC. Results showed that the 3M ON period enhanced and the 3M OFF period reduced NK cell activity.

It was important to proceed with these experiments in a methodical, step-by-step fashion as careful consideration and confirmation of the results were required to preserve the health and well-being of the volunteers.

## 8. Conclusions

In this chapter, the establishment of NCPDIAC and results of the experiments for short-term (2.5H, 2.5-h), mid-term (2W, 2-week), and relatively long-term (3M, 3-month in actual living homes) stays were shown.

Long-term monitoring in actual living homes comprising 6-month, 12-month, and 3-year duration periods has commenced, and the results will be reported in due course.

It is extremely important that appropriate living environments are investigated and created that mitigate or prevent the onset of many diseases such as cancers and virus-infected diseases. In addition to NCPDIAC, other devices that maintain stable temperature as well as increase air tightness may prevent acute accidents related to cardiovascular events. Our recent long-term trial monitoring experiments have included these devices. We hope that these health-promoting indoor environments enable people to live healthier and happier lives.

## Notes and Acknowledgements

All experiments described in this chapter were approved by the Ethics Committee of the Kawasaki Medical School, Kurashiki, Japan.

All authors thank Ms. Shoko Yamamoto and Tamayo Hatayama for their skillful technical assistance.

## Conflicts of interest

For the short-term (2.5H) and mid-term (2W) stay experiments and the in vitro experiments, the Department of Hygiene, Kawasaki Medical School, obtained research funding from SEKISUI HOUSE Ltd., Osaka, Japan. For the long-term (3M) stay experiments, the Department of Hygiene obtained research funding from Yamada SXL Hone Co. Ltd., Takasaki, Japan. Additionally, the extraporous charcoal paints were provided by Artech Kohboh, Co. Ltd., Omura, Nagasaki, Japan.

## Author details

Suni Lee[1], Yasumitsu Nishimura[1], Naoko Kumagai-Takei[1], Hidenori Matsuzaki[2], Megumi Maeda[3], Nagisa Sada[1,4], Kei Yoshitome[1] and Takemi Otsuki[1*]

1 Department of Hygiene, Kawasaki Medical School, Kurashiki, Japan

2 Department of Life Science, Faculty of Life and Environmental Science, Prefectural University of Hiroshima, Shobara, Japan

3 Department of Biofunctional Chemistry, Graduate School of Environmental and Life Science, Okayama University, Okayama, Japan

4 Department of Biophysical Chemistry, Graduate School of Medicine, Dentistry and Pharmaceutical Sciences, Okayama University, Okayama, Japan

*Address all correspondence to: takemi@med.kawasaki-m.ac.jp

## References

[1] Hodgson MJ. Clinical diagnosis and management of building-related illness and the sick-building syndrome. Occupational Medicine. 1989;**4**:93-606

[2] Redlich CA, Sparer J, Cullen MR. Sick-building syndrome. Lancet. 1997;**349**:1013-1016

[3] Menzies D, Bourbeau J. Building-related illnesses. The New England Journal of Medicine. 1997;**337**:1524-1531

[4] Saeki K, Obayashi K, Tone N, Kurumatani N. A warmer indoor environment in the evening and shorter sleep onset latency in winter: The HEIJO-KYO study. Physiology & Behavior. 2015;**149**:29-34. DOI: 10.1016/j.physbeh.2015.05.022

[5] Saeki K, Obayashi K, Tone N, Kurumatani N. Daytime cold exposure and salt intake based on nocturnal urinary sodium excretion: A cross-sectional analysis of the HEIJO-KYO study. Physiology & Behavior. 2015;**152**:300-306. DOI: 10.1016/j.physbeh.2015.10.015

[6] Krueger AP, Reed EJ. Biological impact of small air ions. Science. 1976;**193**:1209-1213

[7] Misiaszek J, Gray F, Yates A. The calming effects of negative air ions on manic patients: A pilot study. Biological Psychiatry. 1987;**22**:107-110

[8] Weber C, Henne B, Loth F, Schoenhofen M, Falkenhagen D. Development of cationically modified cellulose adsorbents for the removal of endotoxins. ASAIO Journal. 1995;**41**:M430-M434

[9] Yamada R, Yanoma S, Akaike M, Tsuburaya A, Sugimasa Y, Takemiya S, Motohashi H, Rino Y, Takanashi Y, Imada T. Water-generated negative air ions activate NK cell and inhibit carcinogenesis in mice. Cancer Letters. 2006;**239**:190-197

[10] Takahashi K, Otsuki T, Mase A, Kawado T, Kotani M, Ami K, et al. Negatively-charged air conditions and responses of the human psycho-neuro-endocrino-immune network. Environment International. 2008; **34**:765-772. DOI: 10.1016/j.envint.2008.01.003

[11] Takahashi K, Otsuki T, Mase A, Kawado T, Kotani M, Nishimura Y, et al. Two weeks of permanence in negatively-charged air conditions causes alteration of natural killer cell function. International Journal of Immunopathology and Pharmacology. 2009;**22**:333-342

[12] Domzig W, Stadler BM, Herberman RB. Interleukin 2 dependence of human natural killer (NK) cell activity. Journal of Immunology. 1983;**130**:1970-1973

[13] Ishikawa H, Saeki T, Otani T, Suzuki T, Shimozuma K, Nishino H, Fukuda S, Morimoto K. Aged garlic extract prevents a decline of NK cell number and activity in patients with advanced cancer. The Journal of Nutrition. 2006;**136**:816S-820S

[14] Nishimura Y, Takahashi K, Mase A, Kotani M, Ami K, Maeda M, Shirahama T, Lee S, Matsuzaki H, Kumagai-Takei N, Yoshitome K, Otsuki T. Exposure to negatively charged-particle dominant air-conditions on human lymphocytes in vitro activates immunological responses. Immunobiology. 2015;**220**:1359-1368. DOI: 10.1016/j.imbio.2015.07.006

[15] Nishimura Y, Takahashi K, Mase A, Kotani M, Ami K, Maeda M, Shirahama T, Lee S, Matsuzaki H, Kumagai-Takei N, Yoshitome K, Otsuki T. Enhancement of NK cell

cytotoxicity induced by long-term living in negatively charged-particle dominant indoor air-conditions. PLoS One. 2015;**10**:e0132373. DOI: 10.1371/journal.pone.0132373

[16] Lee S, Yamamoto S, Nishimura Y, Matsuzaki H, Yoshitome K, Hatayama T, Ikeda M, Yu M, Sada N, Kumagai-Takei N, Otsuki T. Decrease in serum amyloid A (SAA) protein following three-month stays under negatively charged particle-dominant indoor air conditions. Biomedical and Environmental Sciences. 2018;**31**:335-342. DOI: 10.3967/bes2018.044

*Edited by Malek Maaza and Mahmoud Izerrouken*

A charged particle is a particle that carries an electric charge and can be discussed in many aspects. This book focuses on cutting-edge and important research topics such as flavor physics to search for new physics via charged particles that appear in different extensions of the standard model, as well as the analysis of ultra-high energy muons using the pair-meter technique. Also included in this book are the idea of the Eloisatron to PeVatron, the important research field of electrostatic waves in magnetized electron/positron plasmas, and the application of charge bodies.

Published in London, UK


IntechOpen

ISBN 978-1-83962-035-5
9 781839 620355